MEASUREMENT OF $t\bar{t}$ PRODUCTION CROSS SECTION AND SEARCH FOR NEW PHYSICS BEYOND THE STANDARD MODEL

by

Sailesh Chopra

A dissertation submitted in partial fulfillment
of the requirements for the degree of
Doctor of Philosophy
(Physics)
in The University of Michigan
1998

Doctoral Committee:

Assistant Professor J. Qian, Chair
Professor R. Akhoury
Associate Professor M. Aronson
Professor P. Federbush
Professor H.A. Neal

ABSTRACT

MEASUREMENT OF $t\bar{t}$ PRODUCTION CROSS SECTION AND SEARCH FOR NEW PHYSICS BEYOND THE STANDARD MODEL

by

Sailesh Chopra

Chairman: Jianming Qian

We present a measurement of the $t\bar{t}$ production cross section in $p\bar{p}$ collisions at $\sqrt{s} = 1.8$ TeV by the DØ experiment at the Fermilab Tevatron. We observe 40 $t\bar{t}$ candidate events in single and dilepton decay channels with an expected background of 13.3 ± 2.2 events. For a top quark mass of 172 GeV/c^2, we measure the ttbar production cross section to be 5.9 ± 1.8 pb.

We have also performed a search for inclusive energetic diphoton events with large missing transverse energy at DØ. Such events are expected from pair production of charginos and neutralinos within the framework of the minimal supersymmetric standard model with a light gravitino. No excess of events is observed. A 95% CL exclusion region in the supersymmetry parameter space is presented. Lower mass bounds of 150 GeV/c^2 for the lightest chargino and 77 GeV/c^2 for the lightest neutralino are derived.

Both the measurements are based on data from an integrated luminosity of approximately 106 pb^{-1} accumulated during the 1992-1996 collider run.

I deny nothing, but doubt every thing.

Lord Byron, 1788-1824

Be very, very careful what you put into that head, because you will never, ever get it out.

Cardinal Wolsey, 1475?-1530

Dedicated to my parents

ACKNOWLEDGEMENTS

I would first like to express my sincere thanks to the experimental high energy physics group at Panjab University, especially J.M. Kohli and J. B. Singh for introducing me to high energy physics and the DØ experiment. I thank Rajendran Raja at Fermilab for helping me during my initial stay at Fermilab and getting me started on the top quark analysis. I thank the entitr top group at DØ specially Serban Protopopescu, Boaz Klima, Rich Partridge, John Hobbs and Meenakshi Narain. It was only because of Meenakshi's support and encouragement that I could finish the analysis in a timely fashion and contribute to the top quark discovery.

My special thanks to my advisors at Michigan, Homer Neal and Jianming Qian, for helping me join the University of Michigan and supporting me during difficult times. I thank Homer for listening to my various problems and always coming up with a solution. I thank Jianming for trusting me and getting me into the SUSY analysis. He carefully and effectively advised me to make a transition from one physics analysis to the other and helped me finish the SUSY analysis and the thesis in a timely manner.

My stay at Fermilab has been made enjoyable by many friends, without whom the work would have been very hard. At Fermilab, I developed a special friendship with Prem and Prajakta. I could always count on their help and advice in the hours of need. I would like to thank Mrinmoy and Bornali, Bala, Vipin, Brajesh, Shankar, Ashutosh, Satyadev and Dhiman for all the fun I have had with them. I thank my friends Ajay, Amitabh, Anil,

Meenakshi and Anita – who have nothing to do with physics and who simply made my life more interesting and diverse. I want to thank Don Lincoln and Ken Del Signore for reading and rereading the drafts of this thesis and improving it in many aspects with their comments.

Finally, my thanks to my parents and my brother and sisters. Without their support and encouragement my research work would have been much harder.

TABLE OF CONTENTS

LIST OF FIGURES

LIST OF TABLES

CHAPTER 1

INTRODUCTION

People have long asked, "Of what is the world made" and "what holds it together". In ancient times, the Hindu scholars postulated the universe to be made of five elements: earth, water, fire, air and sky (space). Similar views were prevelant in other advanced civilizations of that time. The Greeks were the first to postulate the existence of the *atom*, the building block of all matter. Democritus postulated in 400 BC that:

- by convention there is color,
- by convention there is sweetness,
- by convention there is bitterness,

but in reality there are only atoms and space.

People were not able to test the hypothesis of the atomic nature of matter because of technical difficulties until about the late eighteenth century. The discovery of the fact that equal volume of all the gases at the same temperature and pressure bear ratios of small integers to their weights indicated that there may be some lowest common denominator after all. The ensuing deductions from experiments on the chemical analysis and synthesis of compounds established the hypothesis of atomic nature of matter on firm ground. Soon thereafter, it was found that the atoms could be categorized in terms of their chemical properties (as in the periodic table) which suggested that the atom after all might not be the fundamental particle. Subsequently, a series of experiments in the late eighteenth century (1897, by Thomson, establishing the existence of electrons) and in the early twentieth century (1911, by Rutherford, discovering the positively charged massive "nucleus") established that the atom in fact has structure. The nucleus of a hydrogen atom, the lightest element, was

called a "proton". The 1932 experiment of Chadwick proved the existence of the "neutron", a neutral particle with almost the same mass as a proton, inside the nucleus. Thus the neutron along with electron and proton, were thought to be the basic building blocks of matter. But there were still many unanswered questions: What holds the protons and neutrons inside the nucleus; and why does the nuclear β decay have a continuous energy spectrum?

In an attempt to explain the continuous β spectrum, Pauli postulated the existence of a "neutrino", the massless non-interacting particle in 1930. Four years later, Enrico Fermi came up with the theory of "weak interactions" to explain the anamolously long lifetime of the free neutron. This theory also solved the puzzle of β decay. A year later, Yukawa postulated the existence of a new kind of interaction called the "strong interaction" between protons and neutrons inside the nucleus. This force is mediated by massive particles which he called "π mesons". This particle was discovered in 1947, with a mass very close to what Yukawa had predicted.

Soon after the discovery of Yukawa force carriers, many new particles were observed in various scattering and cosmic ray experiments. Very quickly a need was felt for a new theory to explain the existence of these particles and interactions. Many theories and models were proposed. Some of these were verified experimentally and by 1973 the efforts culminated in a model called the "Standard Model"[1], which could describe all phenomena that are known in particle physics.

1.1 The Standard Model

The Standard Model (SM) describes the universe as being made of two broad categories of particles: the matter particles and the force carriers. Matter particles interact with each other by exchanging the force carrier particles. The matter particles can be divided into two types of fermions (particles with intrinsic spin of 1/2): quarks and leptons. Table 1.1 lists all the "fundamental" matter particles in the Standard Model and Table 1.2 lists all the force carrier particles. Since the gravitional interaction is very small compared to the other interactions in the SM, it is not considered in this discussion.

The six quarks and six leptons are arranged into three generations, each consisting of a doublet: (u, d), (c, s), (t, b) for quarks and (e, ν_e), (μ, ν_μ), (τ, ν_τ) for leptons. The SM doesn't make any predictions about the number of generations of fermions, but it does require that both leptons and quarks appear in doublets.

Particle type	Particle name	Spin	Charge	Mass (MeV/c^2)
Leptons	$e-$neutrino	$\frac{1}{2}$	0	$< 7.3 \times 10^{-3}$
	electron (e)	$\frac{1}{2}$	-1	0.511
	$\mu-$neutrino	$\frac{1}{2}$	0	< 0.27
	muon (μ)	$\frac{1}{2}$	-1	105.7
	$\tau-$neutrino	$\frac{1}{2}$	0	< 35
	tauon (τ)	$\frac{1}{2}$	-1	1784
Quarks	up (u)	$\frac{1}{2}$	$\frac{2}{3}$	≈ 350
	down (d)	$\frac{1}{2}$	$-\frac{1}{3}$	≈ 350
	charm (c)	$\frac{1}{2}$	$\frac{2}{3}$	≈ 1600
	strange (s)	$\frac{1}{2}$	$-\frac{1}{3}$	≈ 550
	top (t)	$\frac{1}{2}$	$\frac{2}{3}$	≈ 175000
	bottom (b)	$\frac{1}{2}$	$-\frac{1}{3}$	≈ 4500

Table 1.1: The "fundamental" matter particles in the Standard Model.

Interaction type	Carrier particle	Spin	Charge	Mass(GeV/c^2)
Strong	gluons ($g_i (i = 1 \ldots 8)$)	1	0	0
Electromagnetic	photon (γ)	1	0	0
Weak	$W^{\pm}$	1	± 1	80.2
	Z	1	0	91.19

Table 1.2: The force carriers in the Standard Model.

Electromagnetic interactions, mediated by photons, can occur only between electrically charged particles. All particles except gluons take part in weak interactions, and the strong interactions are limited to particles with "color" charge which is unique to quarks and gluons. The electromagnetic interactions, described by quantum electrodynamics (QED), and the weak interactions have been unified into the electroweak (EW) theory. Strong interactions are described by Quantum Chromodynamics (QCD). Both EW and QCD are gauge theories which involve fields (mathematical constructs that represent the particles and interactions) that are invariant under the gauge or phase transformation.

The manner in which the gauge enters the theory determines the nature of the

interaction. For example, QED involves the phase factor of $e^{i\phi(x)}$, which represents members of the symmetry group $U(1)$. But for weak interactions, it is convenient to use a two-component field for each doublet: (u, d), (e, ν_e) etc. The gauge transformations in this case involve matrices and can transform a particle into its partner. These transformations belong to the symmetry group $SU(2)$ (sometimes it is written as $SU(2)_L$, since weak interactions only affect particles in left-handed chiral state). The associated gauge bosons necessary to maintain the invariance of the theory are called W_i. There is one boson for each of the three generators of $SU(2)$ transformations. Thus for a theory to be gauge invariant, we require three massless gauge bosons (these are not the same as the massive W and Z bosons):

$$W^+ = (-W_1 + iW_2)/\sqrt{2}$$

$$W^- = (-W_1 - iW_2)/\sqrt{2}$$

$$W^\circ = W_3$$

The electromagnetic force (with its neutral massless gauge boson B°) can be combined with the weak force to give the $SU(2) \times U(1)$ symmetry group for the electroweak theory. There are four gauge bosons in this theory. Two (γ, Z) are electrically neutral and two are charged (W^+, W^-). The photon is massless, whereas the Z ($\sim 91\text{GeV/c}^2$) and the W's ($\sim 80\text{GeV/c}^2$) are massive. This is the case of broken $SU(2) \times U(1)$ symmetry, since originally the gauge bosons of $U(1)$ and $SU(2)$ were massless.

The Higgs mechanism provides a method for spontaneously breaking the electroweak symmetry. Here the assumption is made that the universe is filled with a spin-zero field, called the Higgs field, which is a doublet in the $SU(2)$ space and carries non-zero $U(1)$ hypercharge, but is a singlet in the $SU(3)$ color space. This is analogous to the fact that the vacuum is filled with an electromagnetic field whose sources are electrically charged particles. The gauge bosons and fermions can interact with this field and, in its presence, they no longer appear to have zero mass. A crucial ingredient is that the states with one or more Higgs fields are not orthogonal to the ground state (*i.e* the vacuum) even though these states carry non-zero $SU(2)$ and $U(1)$ quantum numbers. That means the $SU(2)$ and $U(1)$ quantum numbers of the vacuum are non-zero, so the $SU(2)$ and $U(1)$ symmetries are effectively broken. When a symmetry is broken in this way, *i.e.* the symmetry is valid for the interaction but not for the ground state of the system, it is said to be a spontaneously broken symmetry.

A result of the spontaneous breaking of the symmetry for the EW theory is that the W^+, W^- and Z (a mixture of B° and W°) acquire mass and the photon (a different mixture of B° and W°) remains massless. The price one pays is the introduction of a new field representing the spin-zero Higgs boson and a new parameter in the model, θ_W, the mixing angle for relating the Z and γ to the B° and W°.

The Higgs mechanism is the simplest known scheme that generates masses for the W and Z bosons as well as for the quarks and leptons. The triumph of the Higgs mechanism is the prediction of the masses of W and Z bosons. These particles were discovered at CERN in the late 1980's, and their masses were measured to be consistent with the SM predictions.

1.2 The Top Quark

Since the SM requires leptons and quarks to come in pairs, with the discovery of the b quark in 1977 [2], the search for its weak isospin partner quark (the top quark) began. This quark weak isospin doublet was supposed to parallel the third generation of the lepton doublet associated with the τ lepton discovered in 1975 at SLAC [3].

A strong indication that the top quark must exist is based on fact that the b quark behaves like a member of a weak isospin doublet with the $SU(2)_L$ EW interaction. One way of proving this is to measure the forward-backward charge asymmetry in the reaction $e^+ + e^- \to (\gamma, Z) \to b\bar{b}$. This asymmetry is defined as

$$A_{FB} = \frac{\sigma_F - \sigma_B}{\sigma_F + \sigma_B}$$

where σ_F and σ_B are the cross section of b jets in the forward and backward directions respectively. The contribution to the cross section from γ decay is symmetric about the plane perpendicular to the beamline in the Center-of-Mass (CM) frame, but that from the Z is not if the b quark is a member of the weak isospin doublet. A_{FB} is proportional to $t_{3L} - t_{3R}$, where t_{3L} and t_{3R} are the third isospin components of the left-handed and right-handed b quark respectively. To determine these components precisely, one combines the A_{FB} with the measurement of the partial width of $Z \to b\bar{b}$ decays, which is proportional to $(t_{3L} + \frac{1}{3}\sin^2\theta_W)^2 + (t_{3R} + \frac{1}{3}\sin^2\theta_W)^2$. The result shows [4]

$$t_{3L} = -0.504^{+0.018}_{-0.011}$$

$$t_{3R} = -0.008^{+0.056}_{-0.056}$$

Which strongly suggests that the b quark is indeed a $SU(2)_L$ doublet. Therefore its isospin partner, the top quark, should exist.

1.2.1 The Discovery of the Top Quark

Searches for the top quark began in late 1970's. In 1993, the DØ collaboration set a lower limit on the mass of the top quark at 131 GeV [5]. In 1994, the CDF collaboration reported evidence for the existence of the top quark, with a cross section of $13.9^{+6.1}_{-4.8}$ pb, a mass of $174 \pm 10 \pm 13$ GeV, and a significance of 2.8 standard deviations [6].

In 1995, on the basis of more data, both DØ and CDF claimed the discovery of the top quark. DØ reported a cross section of 6.4 ± 2.2 pb and a mass of $199^{+19}_{-21} \pm 22$ GeV on the basis of 50 pb^{-1} of data [7]. CDF measured cross section of $6.8^{+3.6}_{-2.4}$ pb and a mass of $176 \pm 8 \pm 10$ GeV on the basis of 67 pb^{-1} of data [8]. The first set of errors denotes statistical uncertainties and the second denotes systematic uncertainties.

1.2.2 Production and Decay of the Top Quark

At the Fermilab Tevatron collider with a center-of-mass energy $\sqrt{s} = 1.8$ TeV, the Standard Model predicts top quarks will be produced mainly in the form of $t\bar{t}$ pairs. Fig. 1.1 shows the $q\bar{q}$ annihilation and the gluon fusion diagrams for $t\bar{t}$ pair production. Fig. 1.2 shows that as m_t increases, $q\bar{q}$ annihilation dominates the production since the valence quarks are then more likely than gluons to have sufficient momenta to produce top quarks. For a given mass, the cross section for the $t\bar{t}$ process can be calculated using QCD [9, 10, 11]. Fig. 1.3 shows this cross section as a function of the top quark mass.

In the Standard Model, the top quark almost always decays into a W boson and a b quark. The lifetime of the top quark is $\sim 10^{-24}$ seconds, and it decays before it can form bound states with other quarks. Thus hadrons containing top quarks are unlikely to exist and only the decay products of the individual top quarks should be observable. For a $t\bar{t}$ pair, we expect 2 jets from the two b quarks, and additional particles from the decay of two W bosons. The W boson can either decay into a lepton-neutrino pair or to light quarks that fragment into jets. The specific W decays distinguish one $t\bar{t}$ decay channel from another.

Because the coupling strength of the W bosons to fermions is universal, we can predict the branching ratio for any possible $t\bar{t}$ decay channel simply by counting states. Taking into

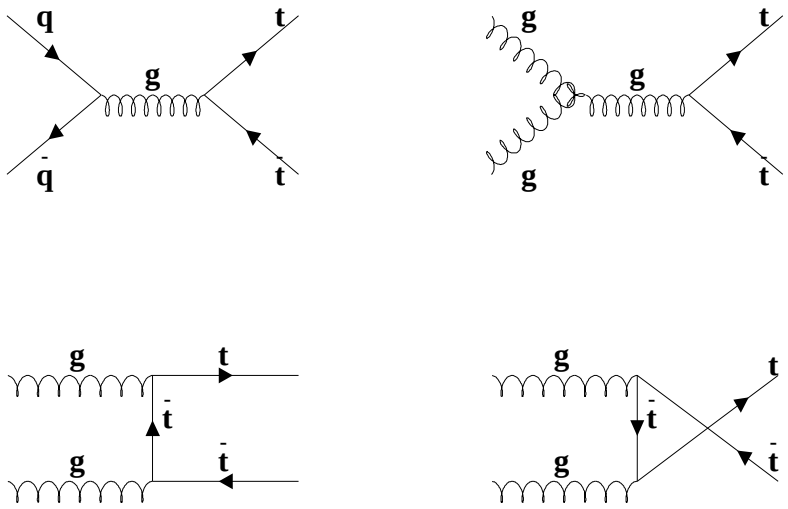

Figure 1.1: The leading order Feynman diagrams for QCD production of $t\bar{t}$.

account the three colors available for each quark pair, it follows that each leptonic decay mode of the W boson has a branching fraction of 1/9, and each quark decay mode has a branching fraction of 1/3. The expected branching fractions for $t\bar{t}$ decay into various channels can be read from Table 1.3. The channel where both W bosons decays hadronically has the largest branching fraction, but it has formidable background contributions from QCD multijet production and will not be discussed in this dissertation. DØ at present does not have a τ lepton identification capability, so the top decays containing a τ lepton will only enter indirectly as small contributions to the other channels when the τ decays to other leptons. All other channels can be classified as the dilepton or the lepton + jets channels depending on whether both or one of the W bosons decay to either a muon or an electron. It can be seen from the Table 1.3 that the total branching fraction for top decaying into e + jets is 12/81. Also the dilepton decay modes ee or $\mu\mu$ each have a branching fraction 1/81, whereas the $e\mu$ mode has branching fraction 2/81. The dilepton channels ee and $\mu\mu$ have a large background contribution from Z decays. All of the dilepton channels have $b\bar{b}$

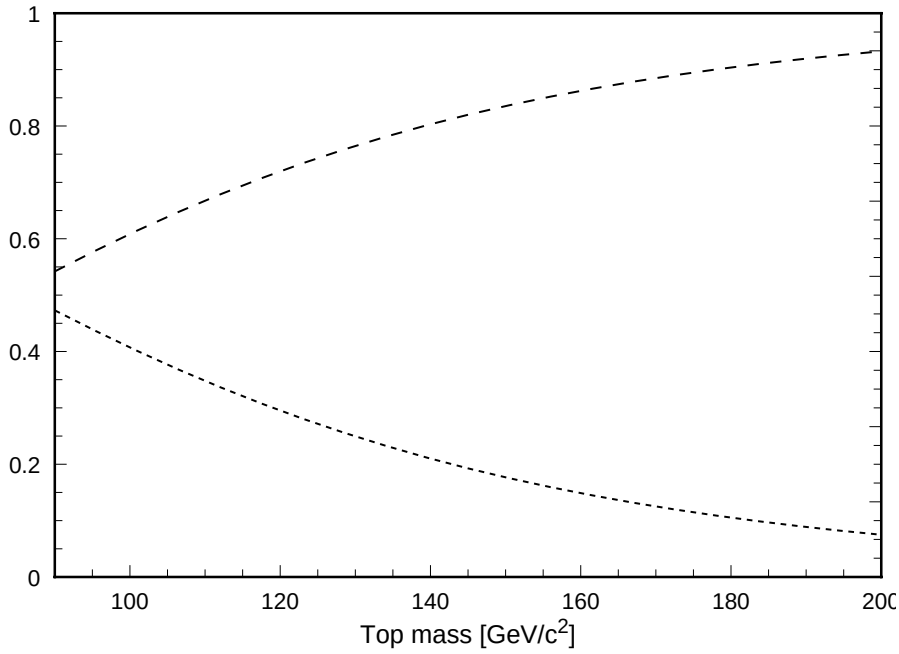

Figure 1.2: Fractional contributions of $q\bar{q}$ (dashed) and gg (dotted) processes (NLO) to the production of $t\bar{t}$ at the Tevatron.

decays and W^+W^- pair production as backgrounds, but their contribution decrease with increasing jet multiplicty.

The major focus of this dissertation is the $e+$jets channel, in which one of the W bosons decays into an electron-neutrino pair and the other W decays hadronically into light quarks as illustrated in Fig. 1.4. Since the neutrino is a neutral, weakly interacting particle, it cannot be observed in the detector. But its presence can be inferred from the presence of transverse energy imbalance (missing E_T or $\not\!\!E_T$) in the detector. The branching ratio of this decay mode is $\sim 15\%$. This decay channel has two major backgrounds. The first one is the physics background arising from the continuum production of the $W+$jets (as opposed to resonance production of $W+$jets in our signal). For the leptonic signatures coming from a real W which happens to have a p_T spectrum like our signal, we only have jet kinematics, event topologies and heavy flavor contents of the jets as discriminants. Fortunately, this background can be reduced to a level below signal without losing much of the efficiency for detecting signal. The second background is attributed to detector imperfections, which will occasionally allow multijet events not containing a real W to mimic the signature of our

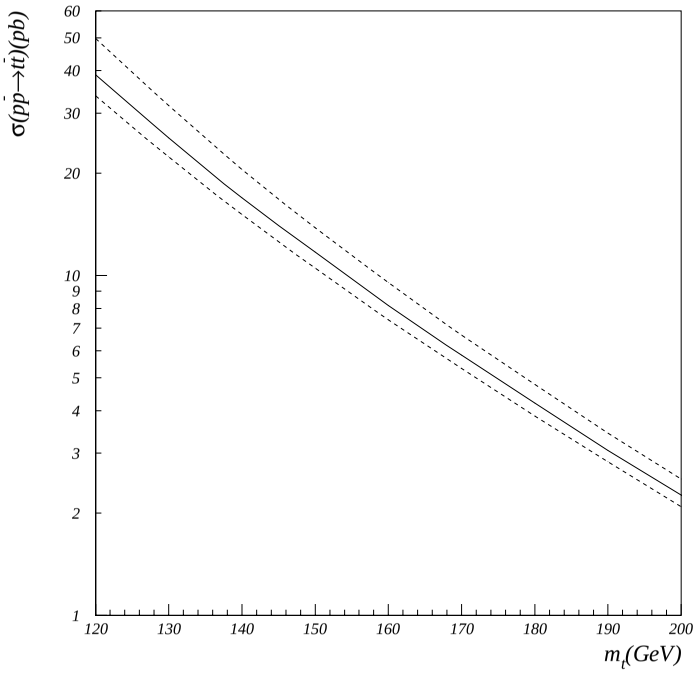

Figure 1.3: The predicted cross section of the process $p\bar{p} \to t\bar{t} + X$ at the Tevatron as a function of the top quark mass. Dashed lines show the uncertainty in the theoretical calculation.

signal. Here, in addition to the jets, the electrons and the $\not\!\!E_T$ can be used to reduce the contribution well below the physics background.

Since the backgrounds have a smaller fraction of b quarks, if one can identify b jets, an excessive fraction of the candidate events in any channel containing b jets would be a strong hint for signal. At present, the only way to accomplish this at DØ is using muon tags ($b \to \mu, b \to c \to \mu$). For $p_T(b) \gg m_b$, such a muon is expected to be buried within the b jet. Such non-isolated muons (as opposed to isolated prompt muons from W decay) can thus be used to tag b jets. This method of detecting the signal for $t\bar{t}$ production at DØ is used in the $\mu-$tag analysis summarized in this dissertation.

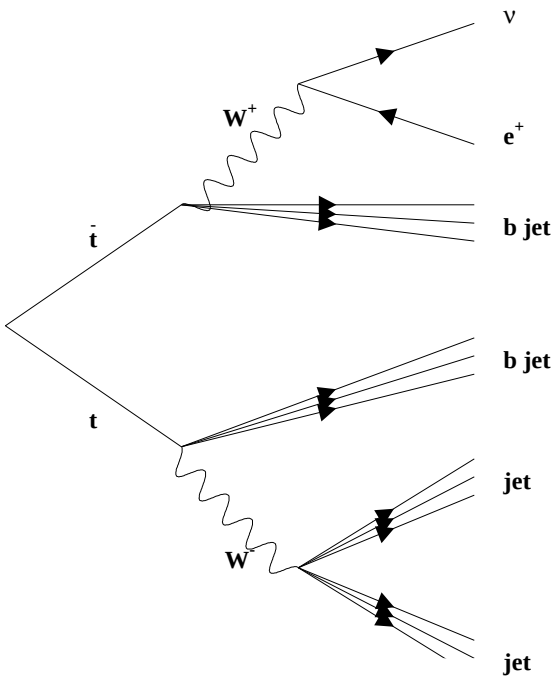

Figure 1.4: The Feynman diagram for the partonic decay sequence of $t\bar{t}$ into a final state containing an electron, a neutrino and four quarks (which hadronize as jets).

1.3 Why Beyond the Standard Model?

The Standard Model, although able to describe all the known phenomena of particle physics, is conceptually incomplete as it leaves many questions unanswered: Why must so many parameters (19 [12]) be derived experimentally? Why do there seem to be three generations of leptons and quarks or, for that matter, why do we need more than one or two? Electroweak symmetry breaking must be performed with the Higgs mechanism to make the weak gauge bosons massive. All these questions suggests the need for a larger, grander theory that would encompass the SM. The new physics will extend and strengthen the foundations of the SM, but because the SM is already a relativistic quantum field theory it will remain an effective description, whether it is fundamental theory or not. The new physics questions can be put

W^+/W^- decay modes	$W^+ \to c\bar{s}, u\bar{d}$ (6/9)	$W^+ \to e^+\nu_e$ (1/9)	$W^+ \to \mu^+\nu_\mu$ (1/9)	$W^+ \to \tau^+\nu_\tau$ (1/9)
$W^- \to c\bar{s}, u\bar{d}$ (6/9)	36/81	6/81	6/81	6/81
$W^- \to e^-\bar{\nu_e}$ (1/9)	6/81	1/81	1/81	1/81
$W^- \to \mu^-\bar{\nu_\mu}$ (1/9)	6/81	1/81	1/81	1/81
$W^- \to \tau^-\bar{\nu_\tau}$ (1/9)	6/81	1/81	1/81	1/81

Table 1.3: $t\bar{t}$ branching fractions can be read off from the table which displays the W^+W^- decay branching fractions, and resulting $t\bar{t}$ final state combinations.

into three categories.

1. The Higgs physics of the SM must be understood. This is the central problem facing particle physics today. While it is a part of the SM, the solution reflects the transition to new physics. If the Higgs bosons exist as light fundamental scalar particles with masses of the order of the Z boson mass, we will be led to one kind of world view, the kind suggested by the paths being pursued with names like supersymmetry or superstrings. If, on the other hand, Higgs physics does not exist in the form of discrete particle states, then a very different (and presently unclear) approach will be needed. Whatever the outcome, at present the question requires experimental input.

2. It could happen that the gauge theory of the SM gets extended. There can be many possibilities in this scenario:

   (a) More families could exist, interacting according to the SM. No limits have been set on the numbers or masses of quarks and leptons it is an experimental question.

   (b) The electroweak and QCD forces (and the quarks and leptons) could be unified into a simpler structure. This possibility is hinted by several properties and patterns of the SM. Theories that include such unification are called "Grand Unified Theories" or GUTs.

   (c) The SM treats left-handed and right-handed fermions very differently, putting them as $SU(2)$ doublets and singlets respectively. It could be possible that at a

higher energies they are treated symmetrically, and what we see is only true in the low energy limit. Approaches having this property are called the "Left-Right Symmetric Theories".

(d) Although so far no transitions have been observed between the weak eigenstates of families, such as $\mu \to e$, it could be that additional gauge bosons exist to generate such transitions. They would be very heavy, making the associated interaction very weak and observable only in rare decays or at very high energies. Gauge symmetries that connect the families in this way are called "Horizontal".

(e) There could be a larger group that contains all or part of the SM groups and has representations including both fermions we know and others. New fermions could occur that, for example, are like quarks but have both left-handed and right-handed states as $SU(2)$ singlets, or carry both quark and lepton number (Leptoquarks).

(f) A symmetry, called supersymmetry (SUSY), which relates fermions and bosons has been suggested. It has a number of attractive features and there are a number of strong theoretical motivations for hoping that supersymmetry might be a symmetry of nature. A locally gauge invariant supersymmetry can be shown to have a connection with gravity. Under certain conditions, which seem to be satisifed phenomenologically or experimentally (such as $m_t \geq m_W$), the Higgs mechanism can be derived from the supersymmetry theory rather than being a separate postulate. While some experimental results of recent years are encouraging, as yet there is no direct evidence for supersymmetry.

3. The third scenario can be in which some unanticipated strong interaction could enter. This would account for composite quarks and leptons, and gauge bosons through complicated dynamics. The SM would be an effective theory at its energy scale, but its form would be only incidentally connected to the underlying theory. Once experiments achieve the scale of the new interactions, a quite different world might appear. This is a logical possibility, though there are no indications at present that it might happen.

We do not know which new physics will occur (if any) but we do know that it will first show up as a small deviation from the SM behavior. In this dissertation, we will concentrate on the supersymmetry theory in the framework of the Minimal Supersymmetric Standard

Model (MSSM). Supersymmetry is a space-time symmetry and it introduces a fermionic partner for every boson (and vice versa) otherwise identical in all internal quantum numbers.

1.3.1 The Minimal Supersymmetric Standard Model (MSSM)

The MSSM is minimal in the sense of being the supersymmetric extension of the SM which has the least number of particles added, while still remaining consistent with the data. THe MSSM is not neccessarily a fundamental theory, it could be the low energy limit of several more fundamental theories like supergravity GUTs, or string-inspired supersymmetric models. These theories, if they have sufficient power, may predict specific ranges for the various parameters which specify the MSSM. Therefore the MSSM, although a model, is in fact quite general and is able to represent a variety of different GUT scale theories in the energy regime accessible at current or forseeable future colliders, and is an excellent starting point for experimental searches for SUSY.

The MSSM adds to the SM an additional Higgs doublet and the supersymmetric partners to the SM particles. Only a few extra parameters, other than the SM parameters need to be defined in the MSSM. With these extra parameters, all the processes in the model are calculable through standard perturbation theory.

Particle Content of MSSM

The supersymmetric partners of the SM gauge bosons and Higgs particle are called *gauginos* and *Higgsinos*. In the SM, electroweak symmetry is broken spontaneously by a single Higgs doublet. For technical reasons [13], the MSSM requires two Higgs doublet fields representing five massive Higgs particles: two charged scalars $H^{\pm}$, one neutral light scalar h, one neutral heavy scalar H and one neutral pseudoscalar A. These particles exist along with the weak gauge bosons: γ, the $W^{\pm}$ and the Z. As a result of electroweak symmetry breaking, gauginos and higgsinos mix to form four neutral mass eigenstates (*neutralinos,* $\tilde{\chi}_i^0, i = 1,2,3,4$) and two charged mass eigenstates (*charginos,* $\tilde{\chi}_j^{\pm}, j = 1,2$).

The fundamental matter particles of the SM are the fermions. In the MSSM, these SM fermions are supplemented by their scalar superpartners. The SM fermions are spin $\frac{1}{2}$ particles with two degrees of freedom. Thus, they each must have two supersymmetric (sparticle) partners called *sfermions*, each with spin zero. For example, an electron e will have two $selectrons, \tilde{e}_L$ and $\tilde{e}_R$, since an electron may have one of two helicities (left or

right handed) and thus has two degrees of freedom. The quarks similarly have *squarks* as their sparticle partners. The neutrinos have two helicity states (although only one couples to matter in the SM), and thus there are two massive scalar *sneutrinos*. The difference between left-handed and right-handed scalars is that while left-handed scalars interact with $W^{\pm}$ bosons (and with the $W^{\pm}$-partner component of the charginos), right-handed scalars do not. Both types interact with the Z and neutralinos and right-handed scalars may interact with the $H^{\pm}$-component of the charginos.

Particle name	Symbol	Sparticle name	Symbol
lepton	l	slepton	$\tilde{l}_L, \tilde{l}_R$
neutrino	ν	sneutrino	$\tilde{\nu}_L, \tilde{\nu}_R$
quark	q	squark	$\tilde{q}_L, \tilde{q}_R$
gluon	g	gluino	$\tilde{g}$
charged weak boson	$W^{\pm}$	chargino	$\tilde{\chi}^{\pm}_{1,2}$
charged Higgs	$H^{\pm}$		
light Higgs	h	neutralino	$\tilde{\chi}_{1,2,3,4}$
heavy Higgs	H		
pseudoscalar Higgs	A		
neutral weak boson	Z		
photon	γ		

Table 1.4: The particle content of the MSSM

1.4 Low Energy Gauge-Mediated Supersymmetry Breaking

Since supersymmetry predicts that elementary particles come in boson-fermion pairs, the absence of these same mass pairs implies that the supersymmetry must be broken. Most of the supersymmetric phenomenological models assume that supersymmetry is broken in a hidden sector at a scale Λ, which is then transmitted to the visible sector of the standard model particles and their supersymmetric partners through either the gravitational interactions (supergravity-inspired models) or the standard model gauge interactions (gauge-

mediated models). The supersymmetric models with gauge-mediated supersymmetry breaking (GMSB) have recently generated considerable theoretical interests [14, 15, 16]. In these models, the supersymmetry breaking scale can be as low as $\Lambda \sim 100$ TeV. Since the gravitino ($\tilde{G}$) mass is directly related to Λ through

$$m_{\tilde{G}} \sim 4.2 \times 10^{-5} \left(\frac{\Lambda}{500 \text{ GeV}} \right)^2 \text{ eV},$$

the gravitino is light (as light as a fraction of an electron-volt, the current gravitino mass limit is $\mathcal{O}(10^{-3})$ eV) and naturally becomes the lightest supersymmetric particle (LSP) in these models. The lightest standard model superpartner, often assumed to be the lightest neutralino ($\tilde{\chi}_1^0$), is the next-to-lightest supersymmetric particle (NLSP). It becomes unstable and decays into a photon plus a gravitino ($\tilde{\chi}_1^0 \rightarrow \gamma\tilde{G}$) if the $\tilde{\chi}_1^0$ has a non-zero photino component (as is often the case). These type of models have been considered for some time [17] though much of the recent speculative theoretical attention was sparked by a single CDF event [18].

In the rest frame of the decaying $\tilde{\chi}_1^0$, the photon is produced isotropically with energy equal to $m_{\tilde{\chi}_1^0}/2$. The gravitino will escape the detector, carrying away unobserved energy. Therefore the SUSY signals can involve up to two energetic photons and missing (transverse) energy, $\not\!\!E_T$, in the GMSB models. At Tevatron energies, the largest production cross sections typically involve the chargino and neutralino production, especially $p\bar{p} \rightarrow \tilde{\chi}_1^+ \tilde{\chi}_1^-$ and $\tilde{\chi}_1^\pm \tilde{\chi}_2^0$. If the sleptons and squarks are heavier than $\tilde{\chi}_1^0$, then $\tilde{\chi}_1^\pm$ and $\tilde{\chi}_2^0$ can decay to $\tilde{\chi}_1^0$ through an intermediate W and Z/γ as

$$\tilde{\chi}_2^\pm(\tilde{\chi}_2^0) \rightarrow \tilde{\chi}_1^0 + W^\pm(Z/\gamma)$$

One can therefore detect supersymmetric signatures using an inclusive $\gamma\gamma + \not\!\!E_T + X$ signal. The signatures for the SUSY with a prompt decay $\tilde{\chi}_1^0 \rightarrow \gamma\tilde{G}$ are so distinct that it can be possible to set quite significant bounds on the available SUSY parameter space and the neutralino and chargino masses using the existing DØ data.

CHAPTER 2

COLLIDER

The collider at Fermilab shown in Fig 2.1, consists of seven major components:

- a Cockroft-Walton accelerator (the pre-accelerator),
- a linear accelerator (the Linac),
- the booster synchrotron,
- the Main Ring synchrotron,
- the antiproton source,
- the antiproton debuncher, and
- the Tevatron Ring synchrotron.

First H^- ions are created in an "ion source" by passing hydrogen gas over a catalytic surface in the presence of free electrons. These ions are released into the pre-accelerator, which produces a static electric field to accelerate the ions to 750 keV. The ions are then injected into the 150 meter long Linac. This device induces an oscillating electric field between a series of electrodes which accelerates the ions to 200 MeV. The H^- ions are then sent through a carbon foil which strips both electrons from each ion. What comes out of the carbon foil are protons (H^+ ions). The protons are then steered into the booster synchrotron ring (500 meters in circumference). A synchrotron is a cyclic accelerator in which the particles are confined to a closed orbit by a series of bending magnets. Quadruple focusing fields keep the beam from diverging. During each pass around the ring, the particles' energy is increased by acceleration in a set of synchronized radio frequency (RF) cavities.

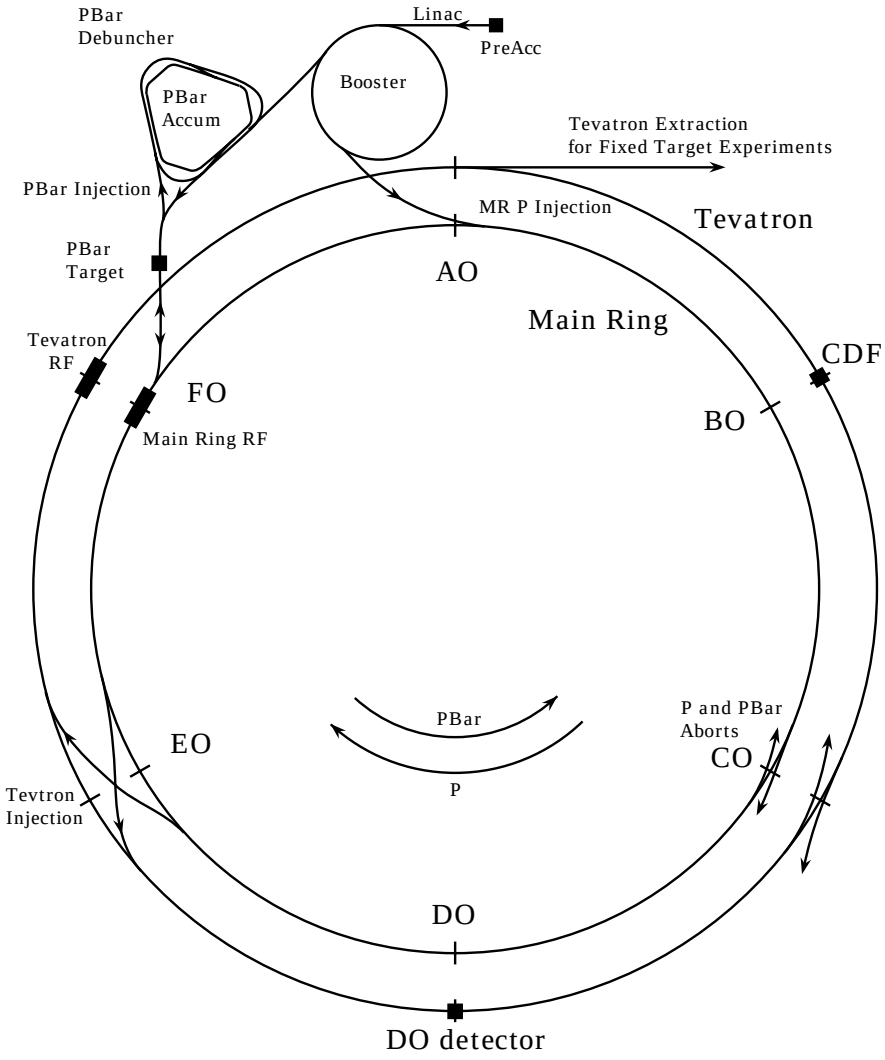

Figure 2.1: Layout of the Tevatron collider at Fermilab.

As the momentum increases, the magnetic field in the bending magnets must be increased to keep the particle in the ring: $p = q \times B \times r$ where p is the particle momentum, q its charge, B the magnetic field and r the radius of curvature. Protons exiting the booster have an energy of 8 GeV. These protons are injected into the Main Ring (MR) which is a synchrotron consisting of more than 1000 conventional copper-coiled magnets in a ring ~ 6 km in circumference. The MR accelerates the protons and coalesces them into shorter bunches. When the protons have attained 120 GeV, the bunches are extracted and directed onto a nickel/copper target, creating about 2×10^7 antiprotons per bunch. A cylinder of liquid lithium creates a focusing magnetic field from a pulsed current of 600,000 amperes which keeps the antiproton beam from diverging. Following this treatment, the antiprotons are injected into the first of two antiproton storage rings.

This first ring is known as the "Debuncher" which uses sophisticated RF techniques to squeeze the antiprotons beam into as compact a phase-space as possible. This process is known as "cooling". The debuncher uses two cooling process: first one is called "debunching" which reduces the fluctuations in the longitudinal component of the antiproton momenta by computer controlled RF manipulation and the second process is known as "stochastic cooling" which restricts the transverse oscillations of the antiproton beam. Fluctuations in the circulating current are detected by sensors which send correction signals to "kicker" electrodes which adjust the path of the particles. When the process is complete, the antiprotons form a ring that looks almost static in a rotating reference frame and are transferred into the antiproton storage ring known as the "Accumulator". The Debuncher and the Accumulator are in the same tunnel, which is 520 meters in circumference. Several different systems within the accumulator provide further cooling and increase the density of the antiprotons approximately by a factor of ten. It takes four to six hours for the antiproton population in the Accumulator to reach 2×10^{11} which is enough for a "shot" into the Tevatron.

Next the protons from the booster ring and antiprotons from the accumulator are transferred to the MR, accelerated to 150 GeV and injected into the Tevatron. The Tevatron is in the same tunnel as the MR, but uses much stronger superconducting magnets which, operating at a temperature of 4.7 K, producing a field of ~ 4 Tesla. In the final step, six bunches of antiprotons and six bunches of protons are simultaneously raised to full energy, i.e. 0.9 TeV. At this energy the beams are squeezed to small transverse dimensions at two beam crossing points, BØ (CDF) and DØ. Before the detectors start collecting data "scraping" is done in which halo and other debris from the beam are removed. In scraping, metal plates

collimate the beam. The typical lifetime of a beam is approximately 20 hours after which its quality falls below the lowest acceptable standard. During this time, the antiproton source runs continuously so that a stack of antiprotons is ready when the next shot is needed.

CHAPTER 3

THE DETECTOR

The DØ detector shown in Figure 3.1 has been constructed to study $p\bar{p}$ collision at a center-of-mass energy of $\sqrt{s} = 1.8$ TeV in the Tevatron collider. The primary focus of the DØ experiment is to study high mass states and large p_T phenomena. This includes the search for the top quark, the production of hadrons containing a b quark, as well as searches for new phenomena beyond the "Standard Model". Details about the DØ detector can be found in ref. [19]. The detector has following features :

- A compact, non-magnetic, central tracking system at the core. This system consists of four subdetectors and is known collectively as the Central Detector (CD). The CD traces the charged particle trajectories with adequate spatial resolution, offers measurements of the absolute charge (using $\frac{dE}{dx}$ in drift chambers) and the absolute charge-to-mass ratio of the particles using the transition radiation.

- A finely-segmented, thick, sampling calorimeter which is the heart of the DØ detector and provides accurate measurement of the energy for photons, electrons, and jets, and the total transverse momenta of neutrinos and other non-interacting particles. It can also provide confirmation for muons based on the minimum ionizing particle (MIP) signature left by them in the calorimeter. The calorimeter forms the layer between the innermost CD and the outermost muon system.

- A muon system with thick magnetized iron absorbers, sandwiched between layers of proportional wire drift chambers. This allows momentum measurement for muons.

We use a right-handed cylindrical coordinate system to describe the events at DØ. The direction of the proton beam defines the polar axis (the z axis, $\theta = 0$). The azimuthal

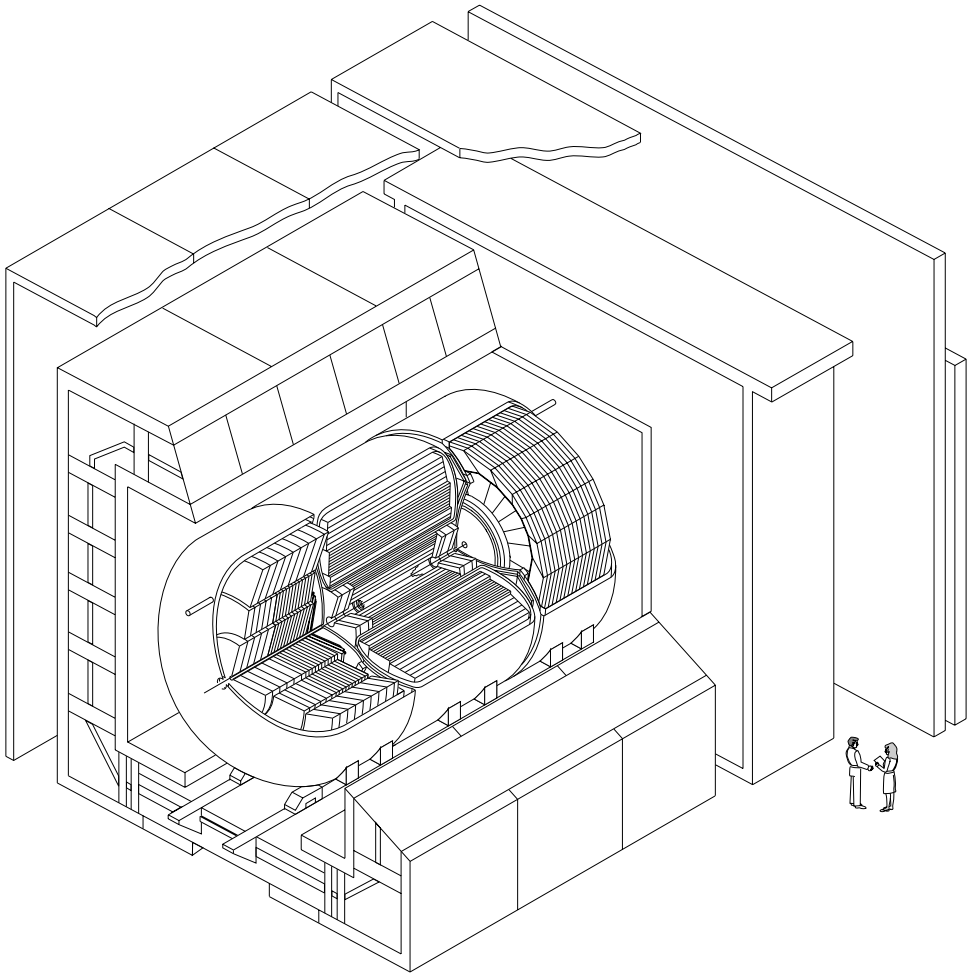

Figure 3.1: Cutway isometric view of the DØ detector.

axis is horizontal such that $\phi = \pi/2$ points vertically upward. The rapidity (y) is defined as

$$y = \frac{1}{2}\ln(\frac{E+p_z}{E-p_z})$$

and pseudorapidity (η) is defined as

$$\eta = -\ln(\tan\theta/2)$$

For $M \ll E$, $\eta \approx y$. Here E is the energy of the particle of mass M. The spatial vectors in the detector are usually defined by r, η and ϕ.

3.1 The Central Detector

The Central Detector system consists of the vertex drift chamber (VTX), the transition radiation detector (TRD), the central drift chamber (CDC) and two forward drift chambers (FDC) as shown in Fig. 3.2.

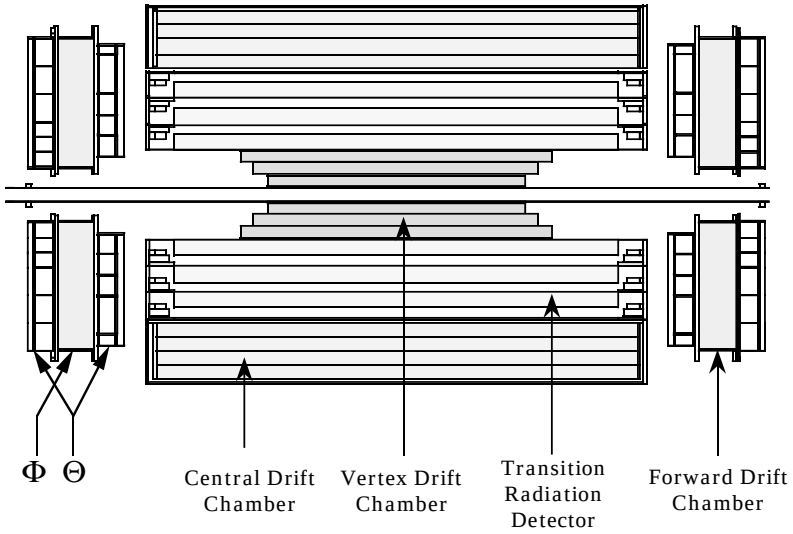

Figure 3.2: A side view of the DØ central tracking system .

The VTX, TRD and CDC are concentric with the beam pipe and cover a large angular region. The FDCs are oriented perpendicular to the beam axis. All central detectors are located within the region, $r = 78$ cm and $z = \pm 135$ cm which is restricted by the inner surfaces of the calorimeter.

3.1.1 The Vertex Detector

The VTX chamber is the innermost tracking detector and has an inner radius of 3.7 cm and outer radius of 16.2 cm. It consists of three independent concentric layers of cells mounted on carbon fiber tubes (as shown in Fig. 3.3). The innermost layer has 16 azimuthal cells and the outer two layers have 32 azimuthal cells each. The sense wires provide a measurement of the z coordinate by readout at both ends. To obtain good spatial resolution and track pair resolving power, a gas mixture of $CO_2(95\%)$ and ethane(5%) at 1 atm with a small admixture of H_2O was chosen.

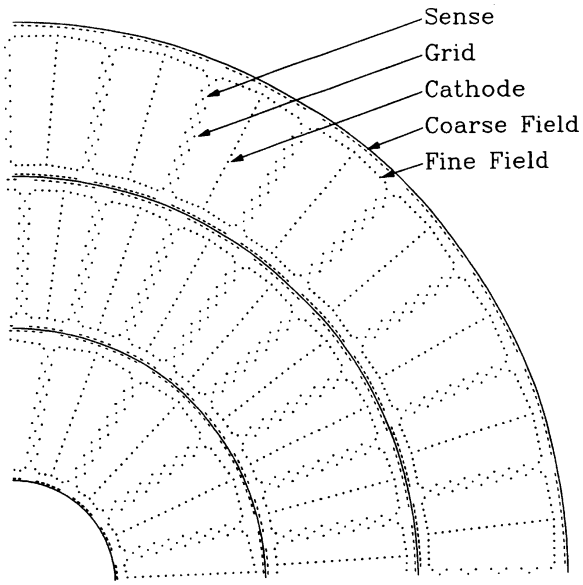

Figure 3.3: An end-view of one quadrant of the DØ vertex detector.

3.1.2 The Transition Radiation Detector

The TRD is located between the VTX and the CDC and provides independent electron/pion separation in addition to that given by the calorimeter. Transition radiation x-rays are produced when highly relativistic charged particles ($\gamma \gg 1$) traverse boundaries between media with different dielectric constants. The energies of radiated x-rays depend on the mass of the charged particle. The TRD consists of three separate units, each containing a radiator and an x-ray detection chamber. The energy spectrum of the x-ray, determined by the thickness of the radiator foil and the gap between the foils, peaks at 8 keV and is mainly contained below 30 keV. A two-stage proportional wire chamber (PWC) is mounted just after the radiator for the detection of x-rays. The x-rays convert mainly in the first stage of the chamber and the resulting charge drifts radially outward to the sense wire.

3.1.3 The Central Drift Chamber

The CDC sits in region between the TRD and the inner surface of the central calorimeter. It consists of four concentric layers of drift chambers and each layer has 32 azimuthal cells as shown in figure 3.4 . Each cell contains seven sense wires with its readout at one end and two delay lines read out from both ends. The delay lines propagate the signals induced from the neighboring anode wire; the difference between the arrival times at both ends provides the z-coordinate of the track. The gas mixture in the CDC is Ar(92.5%) CH_4(4%) CO_2(3%) with 0.5% H_2O. The CDC coverage extends to $|\eta| \leq 1.2$.

3.1.4 The Forward Drift Chamber

The FDCs extend the tracking coverage out to $|\eta| \approx 3$. They are positioned at both ends of the concentric barrels of the VTX, TRD and CDC as shown in Fig. 3.5. Each FDC consists of three separate chambers: a phi module (Φ) and two theta (Θ) modules, which provides phi and theta coordinates, depending upon the direction of the sense wire.

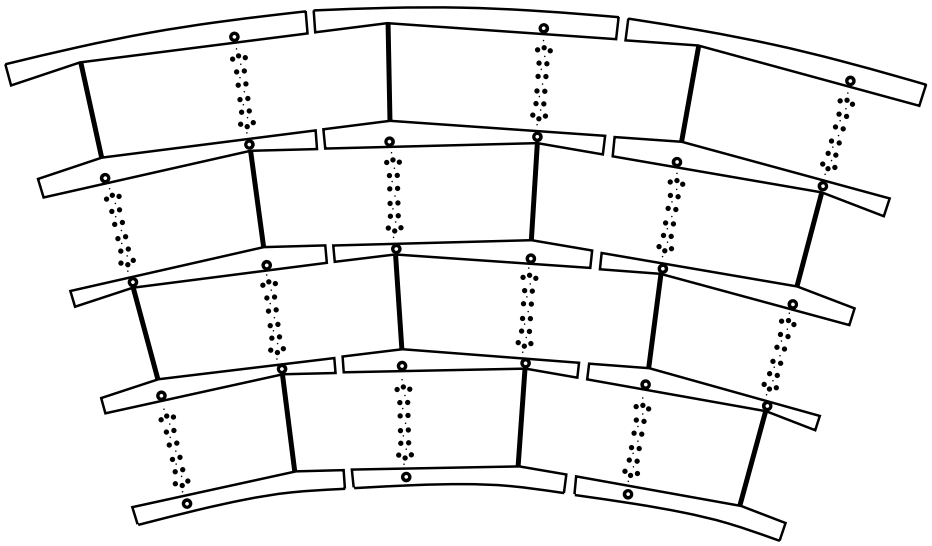

Figure 3.4: An end view of one $\frac{3}{32}$ of the DØ central drift chamber.

3.2 The Calorimeter

The primary purpose of a calorimeter is to measure energy. Liquid argon and depleted uranium are the active and passive (absorber) materials in the DØ calorimeter. As shown in figure 3.6 , it consists of three cryostat systems: a central calorimeter (CC) and two end-cap calorimeters (EC).

Since there is no central magnet, the DØ calorimeter plays a dominant role in the identification of high p_T objects: electrons, photons, jets & muons and in determining the missing transverse energy. Each cryostat calorimeter consists of three distinct types of calorimeter modules: an electromagnetic section (EM) with relatively thin uranium absorber plates, a fine hadronic section (FH) and a coarse hadronic section (CH) with thick copper or stainless steel plates.

3.2.1 Operation Principles

A typical unit cell of the calorimeter consists of a uranium plate and a readout board submerged in LAr (Liquid Argon), as shown in figure 3.7.

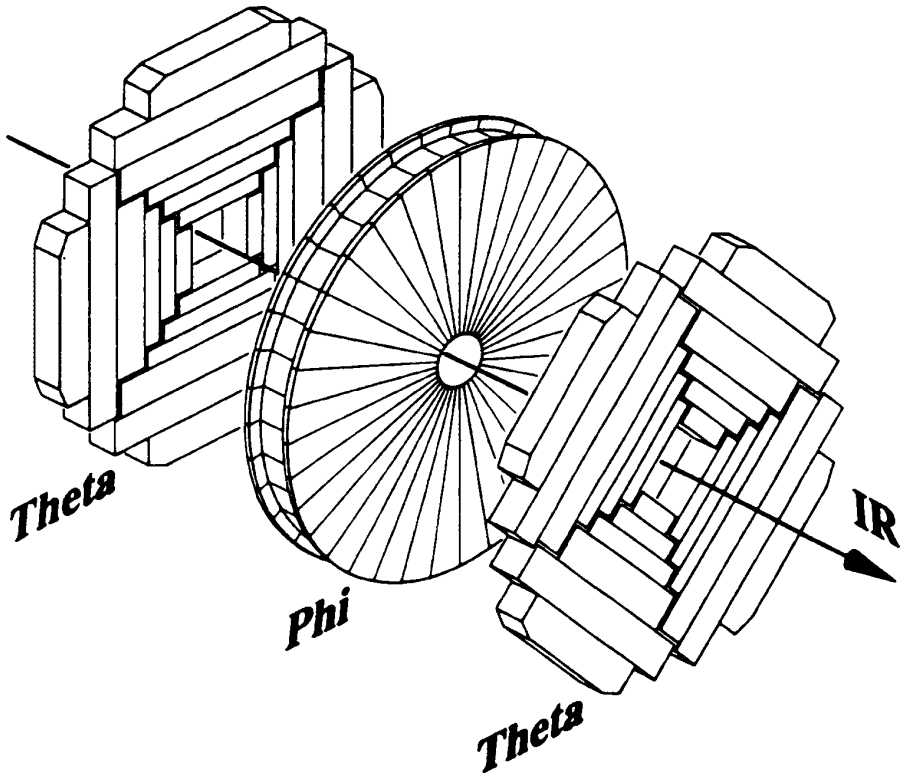

Figure 3.5: An exploded isometric view of one of the DØ forward drift chamber.

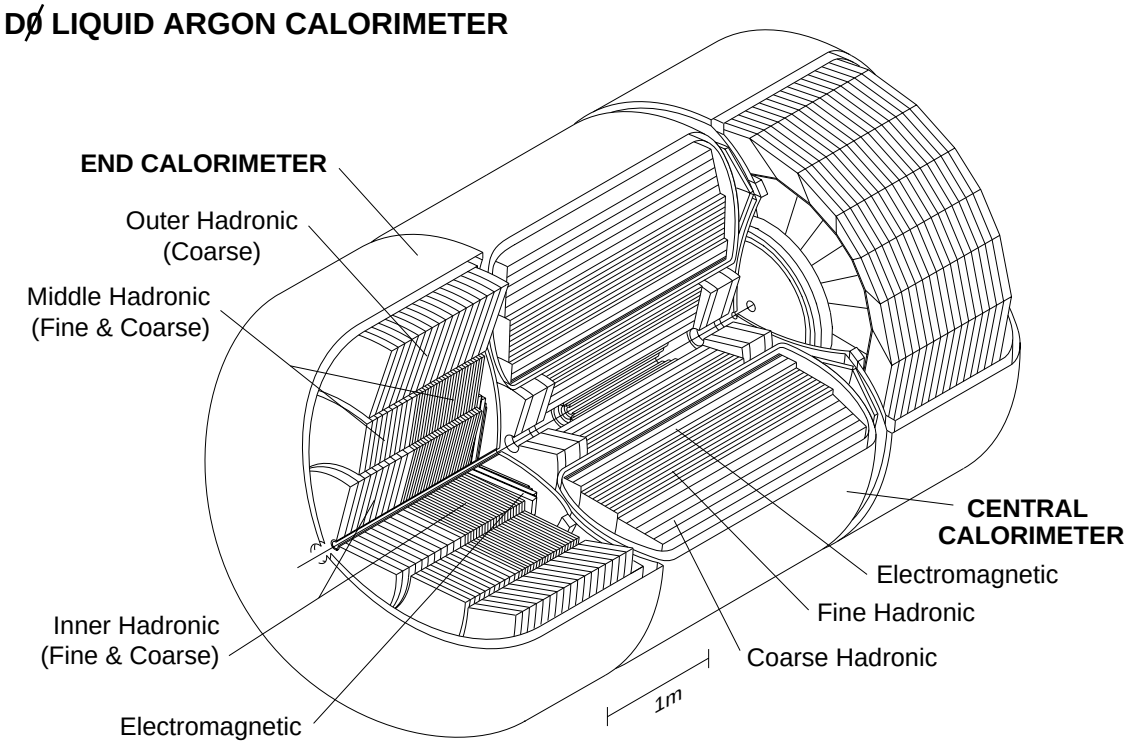

Figure 3.6: A cut-away view of the DØ calorimeter.

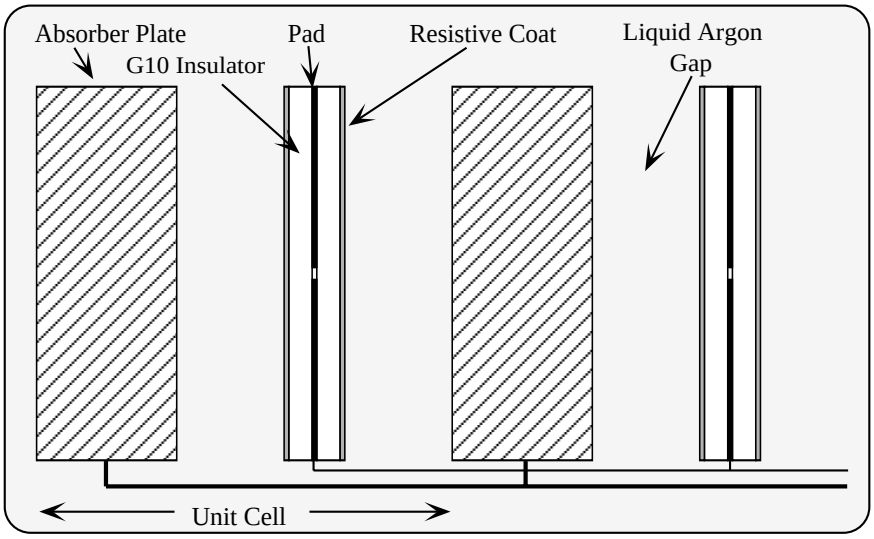

Figure 3.7: A schematic view of a unit cell of the DØ calorimeter.

The readout boards are constructed by laminating two separate 0.5 mm thick G-10 sheets. Each board has one surface coated with high resistivity, carbon-loaded epoxy. One of the inner surfaces is left with bare G-10 on the uncoated side; the other sheet, originally copper-clad, is milled into the pattern desired for the segmented readout. An electric field is formed by grounding the metal absorber plate and connecting the resistive surface of the readout board to positive high voltage. Thus the resistive surfaces act as anodes and the readout board operates as a capacitor.

When a high energy particle goes through dense material, e.g. uranium, a shower of particles occurs via various electromagnetic and hadronic interactions. These particles ionize the active material (e.g. LAr) via electromagnetic interactions and the ionization electrons drift toward the anode under the influence of the electric field. These electrons then induce an image charge on the inner copper surface. This charge is routed to external charge-sensitive preamplifiers and subsequently to a baseline subtracter (BLS) which is a shaping and sampling circuit. The baseline and the peak of the signal are sampled in the circuit and their difference is sent to an analog-digital converter (ADC), the output of which is transported to a computer. If the signal values are within a given range of their pedestal values, their channels are suppressed to reduce the quantity of the output data.

3.3 The Muon System

The DØ muon detection system consists of solid-iron toroidal magnets and three layers of proportional drift tube chambers (PDTs). One layer of PDT chambers inside the toroidal magnets has four drift planes. The other two layers each have three planes and are located outside the magnet. The purpose of this system is to identify muons produced in $p\bar{p}$ collisions and measure their momenta. The muon system is divided into two sub-systems: wide angle muon system (WAMUS) covering central region ($|\eta| < 2.5$) and small angle muon system (SAMUS) with forward and backward coverage ($2.5 < |\eta| < 3.6$). The toroidal magnets are also separated into three parts, a central toroid covering the region $|\eta| < 1.0$, two end toroids for $1 < |\eta| < 2.5$ and two SAMUS toroids covering $2.5 < |\eta| < 3.6$. Since a muon must traverse the calorimeter and the thick toroidal magnet, it must have a minimum momentum of 3.5 GeV/c at $\eta = 0$ and 5 GeV/c at $\eta = 2$.

3.4 Data Aquisition System

The collision rates at the Tevatron are very high and require a data acquisiton system which can reduce the rate at which events are written to tape to a manageable level. To accomplish this task, DØ employs a multi-level triggering scheme composed of two hardware triggers and one software trigger. The final rate out of this last level is about 3 events per second or approximately 2 MBytes/sec.

3.4.1 Level 0

The Level 0 trigger registers the presence of inelastic collisions and serves as the luminosity monitor for the experiment. It uses two hodoscopes of scintillation counters mounted on the front surfaces of the end calorimeters. These hodoscopes have an array of counters inscribed in a 45 cm radius circle to give partial coverage for the rapidity range $1.9 < |\eta| < 4.3$ and nearly full coverage for $2.3 < |\eta| < 3.9$. The rapidity coverage is set by the requirement that a coincidence of both Level 0 detectors be $\geq 99\%$ efficient in detecting inelastic collisions.

The difference in the arrival time of particles to the detectors at both ends is used to determine the $z-$coordinate of the collision point. Although most of the collisions happen

near $z = 0$, the large spread of the collision vertex distribution ($\sigma \approx 30$ cm gaussian) can introduce a large error in the transverse energy (E_T) computation. At high luminosity, the probability of multiple interactions is sizable. When multiple interactions are present, the time difference information from the Level 0 is ambiguous and a flag is set to identify these events for the subsequent trigger levels.

3.4.2 Level 1

Level 1 is a collection of hardware trigger elements arranged in a flexible, software-driven architecture that allows for easy modifications. All Level 1 triggers operate within the 3.5μsec time interval between the beam crossings and thus do not contribute to dead time. The overall control of the Level 1 trigger resides in the Level 1 framework [19] which houses hardware to process special fast readouts of the calorimeters and muon systems. There are 32 available trigger bits and basic decisions concerning the η and E_T of muons, electrons and jets can be performed according to several programmed thresholds. In muon triggers, crude tracks are found in wide roads and events are selected based on the number of muons and their rapidity. A fast sampling of calorimeter energy in 0.2×0.2 'trigger' towers with $|\eta| < 3.2$ is available so that electrons and jets can be defined and identified as EM or EM + FH trigger towers. The input rate is approximately 280 kHz with a rate reduction to about 2000 Hz to Level 2.

3.4.3 Level 2

Candidates from Level 1 are passed through the standard DØ data acquisition pathways to a farm of microprocessors which serve as Level 2 trigger systems [20] as well as event builders. Sophisticated software algorithms resident in the Level 2 processors reduce the output rate to 2-3 Hz before passing events to the host computer for event monitoring and recording on tape. There are 48 software event-filtering nodes in the Level 2 system. The VAX-ELN filtering process in each node is built around a series of filter tools. Each tool has a specific function related to the identification of a type of particle or an event characteristic.

CHAPTER 4

EVENT RECONSTRUCTION

Raw data consists of digitized electronic signals from different parts of the DØ detector. These signals are produced by the particles that are the final products of individual collisions ("events"). However, one cannot describe the kinematic parameters of these particles using the raw information. The process of turning this raw information into the kinematic parameters of the particles is known as event *reconstruction*. The reconstruction process in DØ is carried out by a software package called DØRECO (containing about 150,000 lines of Fortran code).

4.1 Event Vertex

The event vertex information is very important for reconstructing the 4-momenta of various final state particles produced in the detector. The vertex position is reconstructed using the following procedure:

- Tracks in the CDC are reconstructed and extrapolated to the center of the detector.
- The intersection of these reconstructed space tracks with the beam axis form a distribution in z. The estimated z position of the vertex is the mean of a gaussian fitted to this distribution. In the case of a z distribution with more than one peak and therefore multiple vertices, the vertex with the maximum number of tracks is considered to be the primary vertex.

The resolution of the vertex z-position is about 1-2 cm, depending on the number of reconstructed tracks associated with it. Multiple vertices can be typically separated if they are at least 7 cm apart [21].

4.2 Electrons and Photons

An electron or photon is identified as localized energy in the electromagnetic calorimeter. Electrons or photons are reconstructed by the following procedure:

- A cluster is constructed by starting with the highest-E_T EM tower and adding nearby towers with E_T above certain threshold to the cluster. The E_T of each $\Delta\phi \times \Delta\eta = 0.1 \times 0.1$ tower is calculated by summing up energies in all the EM and first hadronic (FH1) cells in the tower.

- At least 90% of the energy of the cluster should be from the EM calorimeter and 40% of its energy should be contributed by a single tower.

- The centroid of the cluster is calculated as the logarithm of energy ($\log_e(E)$) weighted mean of the cell positions in the third EM layer (as third layer is the most finely segmented EM layer).

- If there is a track in the central detector within a solid angle (frequently referred to as a "road") of $\Delta\eta = \pm 0.1$ and $\Delta\phi = \pm 0.1$, pointing from a vertex to the cluster, the cluster will be identified as an electron; otherwise it is considered a photon.

The electron energy resolution is

$$\left(\frac{\sigma}{E}\right)^2 = C^2 + \frac{S^2}{E} + \frac{N^2}{E^2}$$

where E is the mean energy, C is the constant term, S is the error due to statistical fluctuations, and N reflects the noise due to the electronics and the radioactivity of the absorber (uranium).

4.2.1 Electron Identification

The above reconstruction requirements are very loose. There are many variables that are used to refine the selection of electron candidates for the final analysis. The following variables can be used to further discriminate electrons from other objects.

- Isolation fraction:

The electrons coming from a W or Z are generally isolated in space from other objects. Therefore the fraction of the energy outside a certain well-defined cone should be small. In order to quantify this idea, the *isolation fraction* is defined as

$$f_{iso} = \frac{E_{TOT}(\mathcal{R} = 0.4) - E_{EM}(\mathcal{R} = 0.2)}{E_{EM}(\mathcal{R} = 0.2)}$$

where $E_{TOT}(\mathcal{R})(E_{EM}(\mathcal{R}))$ is the total (EM) calorimeter energy in a cone of radius $\mathcal{R} = \sqrt{\Delta\eta^2 + \Delta\phi^2}$. The typical requirement for good electron is $f_{iso} < 0.1$.

- Covariance Matrix χ^2:

  Suppose $\mathbf{X}$ is a vector whose components are a set of M linearly independent variables ($\mathbf{X} = x_1, x_2, \ldots, x_m$). The covariance matrix (the multi-dimensional analogue of the variance), V, is then given as

  $$V_{ij} = \overline{(x_i - \bar{x}_i)(x_j - \bar{x}_j)}$$

  where the overline stands for the average of the respective variables.

  Then the χ^2 for an event with $\mathbf{X}$ not in the sample is defined as

  $$\chi^2 = \sum_{i,j} (x_i - \bar{x}_i) V_{ij}^{-1} (x_j - \bar{x}_j)$$

  The components of $\mathbf{X}$ are linearly independent, so V is invertible and the above function is well defined. Since V is symmetric, it can be diagonalized. Suppose $\mathbf{Y} = (y_1, y_2, \ldots, y_m)$ are the eigenvectors of V and ${\sigma_i}^2$ $i = 1, \ldots, m$ are its eigenvalues. Then

  $$\chi^2 = \sum_i \frac{({y_k}^i - \bar{y}^i)^2}{{\sigma_i}^2}$$

  A small χ^2 requires that the event k be close to the means $\bar{y}^i$ if the $\mathbf{Y}$ distributions of the sample events are approximated by gaussians with variances σ_i.

  To have a better electron identification, the χ^2 has been calculated for a set of 41 variables. These variables are:

  -- The fractional energies in layer 1, 2 and 4 of the EM calorimeter;

-- The fractional energy in each cell of the 6×6 array in the third layer of the EM calorimeter;

-- The vertex $z-$component; and

-- The logarithm of the total energy of the cluster.

The covariance matrix V is obtained using Monte Carlo electrons.

- Track ionization:

  Since there is no central magnetic field in the DØ detector, e^+e^- pairs from photon conversions will not separate from each other and may be reconstructed as a single track. However, their energy deposition per unit length (dE/dx) will be twice that of a single charged particle. To remove photon conversions, dE/dX is required to have:

  $dE/dx \leq 1.5$ or $dE/dX \geq 3.0$ for CDC;

  $dE/dx \leq 1.3$ or $dE/dX \geq 2.7$ for FDC;

- Track match significance:

  At DØ, photon can be identified as an electron if it has a track reconstructed in its road due to the presence of a charged hadronic particle in close proximity. One can reduce the probability of a photon with a charged track overlap to be identified as an electron by requiring the CD track to point precisely to the centroid of the calorimeter cluster.

  The *track match significance* is defined as:

$$S = \sqrt{\left(\frac{\Delta\phi}{\sigma_{\Delta\phi}}\right)^2 + \left(\frac{\Delta z}{\sigma_{\Delta z}}\right)^2} \text{ for the CC;}$$

$$S = \sqrt{\left(\frac{\Delta\phi}{\sigma_{\Delta\phi}}\right)^2 + \left(\frac{\Delta r}{\sigma_{\Delta r}}\right)^2} \text{ for the EC;}$$

  where $\Delta\phi$, Δz and Δr denote the coordinate differences between the track hit and the cluster centroid, and $\sigma_{\Delta\phi}$, $\sigma_{\Delta z}$ and $\sigma_{\Delta r}$ are the corresponding resolutions.

- Electron Likelihood :

  In order to obtain a better background rejection, a multivariate discriminant L^e is constructed using the four variables: χ^2, S, dE/dx and f_{EM} where $f_{EM} = \frac{\text{EM energy}}{\text{Total energy}}$.

The likelihood method is applied to obtain this cut. The optimized cuts [22] on the discriminant are:

$$L^e < 0.25 \text{ for the CC and } L^e < 0.3 \text{ for the EC.}$$

These cuts have been used in the $t\bar{t}$ cross section measurement analysis. Table 4.1 summarizes the efficiencies for different electron-id cuts relevant to this thesis.

Cut	CC	EC
$f_{EM} > 0.95.\text{AND.}\chi^2 < 100$	0.923 ± 0.011	0.886 ± 0.023
$.\text{AND.}f_{iso} < 0.1$		
$L^e < 0.25.\text{AND.}f_{iso} < 0.1$	0.814 ± 0.013	
$L^e < 0.30.\text{AND.}f_{iso} < 0.1$		0.491 ± 0.020
Track finding (Data)	0.864 ± 0.014	0.861 ± 0.018
Track finding (Monte Carlo)	0.948 ± 0.006	0.907 ± 0.016

Table 4.1: Electron/photon identification efficiencies for various cuts in the central (CC) and end (EC) calorimeter. The likelihood cuts are used for electrons only and f_{EM}, χ^2 and f_{iso} cuts are used for photons.

4.2.2 Photon Identification

For the analysis in this thesis, photons are required to have an E_T above 12 GeV or 20 GeV, and they are required to be well separated from any other object in the event. Photons at DØ are detected in the same manner as electrons: through electromagnetic showers in the calorimeter. The EM showers of electrons and photons are practically identical, so the same calorimeter-based quantities are used to identify photons. Instead of using a likelihood variable for photons, we require photons to satisfy the following cuts:

- EM fraction $f_{EM} > 0.95$.
- H-matrix $\chi^2 < 100$.
- Fractional isolation $f_{iso} < 0.1$

The efficiency for these cuts is same as for electrons as shown in Table 4.1.

The efficiencies quoted in Table 4.1 are only valid for electrons or photons with $E_T > 20$ GeV. For lower E_T, the fractional isolation and χ^2 cuts are less efficient. The χ^2 cut is not as efficient at low E_T, as it is tuned using high E_T electrons. The fractional isolation suffers at low E_T because of the underlying event and other noise in the detector which can be a significant portion of a 12 GeV cluster but not a 20 GeV cluster. Since no high-statistics, low-background source of low-energy electrons or photons exists in the data, the E_T dependent decrease of the effciency is modeled using Monte Carlo photons overlaid with minimum bias data [23]. The E_T-dependent decrease of efficiency can be parametrized in a functional form as:

$$\epsilon(E_T) = A + BE_T + CE_T^2$$

The parameters A, B and C are given in Table 4.2. $\epsilon(E_T)$ is then multiplied by the efficiency for high E_T photons given in Table 4.1 . The curves showing variation of $\epsilon(E_T)$ are shown in figure 4.1 for both central and end calorimeters. It is important to note that even though there is a loss of efficiency for detecting low E_T photons, the efficiency for detecting photons with $E_T > 20$ GeV is quite high.

	A	B	C
CC	-0.1720	0.1023	-2.234×10^{-3}
EC	0.6660	0.0219	-3.211×10^{-4}

Table 4.2: Values of fit parameters for modeling photon-id efficiencies for $E_T < 20$GeV, for the CC and EC.

Since photons at DØ are required to have no associated track, tracking quality cuts such as those used for electrons have no meaning, but we still can use the central tracking information to improve the purity of the photon sample. The dominant sources of backgrounds to real photons tend to leave hits in the tracking chambers because they are either real electrons which fail to have a track reconstructed or they are neutral mesons which decay into 2 photons. Generally, these mesons are produced along with many other mesons, some electrically charged, in a jet. These charged mesons leave a signature in the tracking chambers similar to that of electrons. An analysis package was developed to check very tight

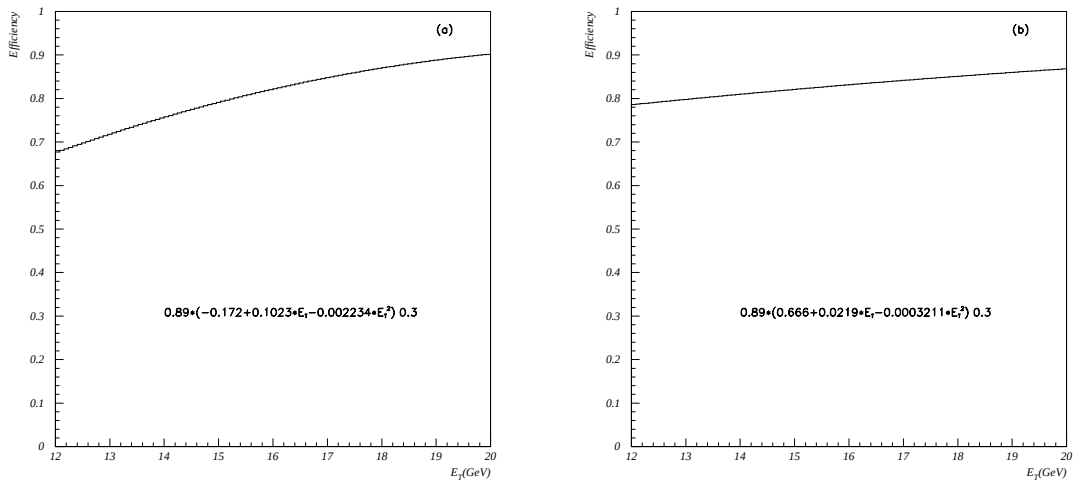

Figure 4.1: The curves showing the E_T dependent decrease in the photon-id. efficiency for CC (a) and EC (b).

roads (0.005×0.012 in $\theta - \phi$ space) pointing from EM calorimeter clusters towards the event vertex and counting the number of hits in the road.

We require the following cuts for selecting the sample of clean photons:

- Fraction of wires hit in the VTX chamber ≤ 0.3,
- Number of 3-dimensional hits in the VTX chamber ≤ 8.
- Photons passing through the CDC:
  - -- Fraction of wires hit ≤ 0.3,
  - -- Number of XY hits ≤ 20,
  - -- Number of 3-dimensional hits ≤ 1, and
  - -- Number of z-segment hits $= 0$.
- Photons passing through the FDC:
  - -- Fraction of wires hit ≤ 0.7,
  - -- Number of XY hits ≤ 30.

Along with these cuts (collectively called the HITSINFO cut), we also require that there is no track in the road pointing from the EM cluster to any of the reconstructed vertices.

The efficiency for the HITSINFO cut was measured using "emulated photons". Starting with the $Z \to ee$ sample, the calorimeter cluster positions of electrons are rotated in ϕ by $\pi/2$ and a new, tight road was constructed between this emulated photon and the vertex. This method has the advantage of implicitly taking into account, effects such as instantaneous luminosity and multiple interactions. To truly model the effects of underlying events, $Z+$jets events are rejected by requiring the $r-\phi$ opening angle of the electrons to be greater than 170°. The efficiency loss due to random track overlap in the tracking road is taken into account by rejecting any rotated calorimeter cluster which has a track pointing to it in a tracking road for any of the vertices. All of the HITSINFO variables are recomputed using the new rotated clusters; the efficiency is then the fraction of "emulated photons" passing the HITSINFO cut. The efficiency of the 'no track in road' and the HITSINFO cuts for photons obtained this way is:

- For photons through the CDC: 0.78 ± 0.02, and
- For photons through the FDC: 0.80 ± 0.05.

A photon would not be identified if it interacts in the material in front of the tracking chambers. The photon conversion probability (P_C) is estimated using single photon Monte Carlo events, which are run through the detector simulation program, DØGEANT [24]. The computed P_C is a function of pseudorapidity. The average efficiency loss due to photon conversion is about 10%(30%) for CC (EC). The estimated systematic error is about 10% of the conversion probability. Fig. 4.2 shows the conversion probability as function of photon η.

The combined identification efficiency ϵ_γ $(= \epsilon_C \times \epsilon_H \times \epsilon_X)$ from the calorimeter cluster reconstructed as a photon (PPHO) with $E_T > 20$ GeV is about 75% in the CC and 60% in the EC. Here ϵ_C is the efficiency for calorimeter cuts, ϵ_H is the efficiency for HITSINFO cuts and $\epsilon_X = (1 - P_C)$.

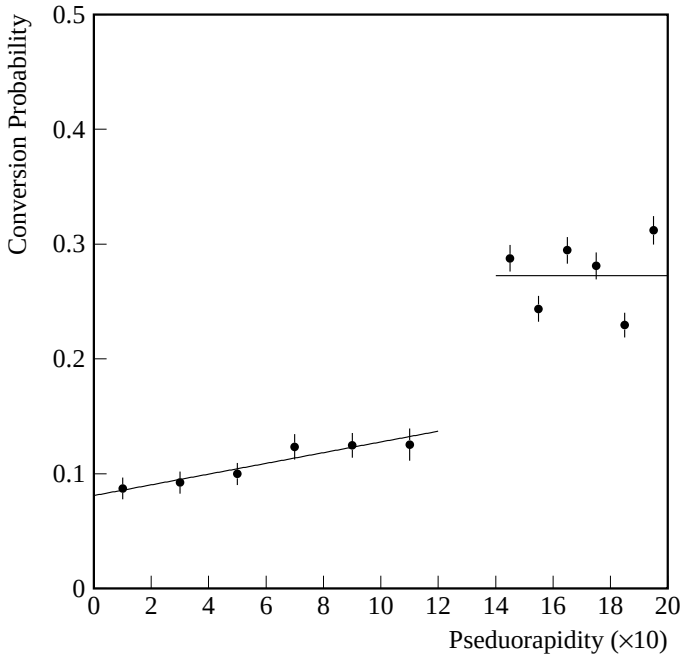

Figure 4.2: Photon conversion probability as a function of pseduorapidity. The errors are statistical only. The systematic error is estimated to be about 10% of the conversion probability.

4.3 Jets

Jets reconstruction is carried out using the "cone algorithm", which defines a jet as the energy inside a cone with a fixed size in $\eta - \phi$ space. In this algorithm, the calorimeter towers are sorted in E_T to form a set of "seed" clusters. A precluster is constructed using all of the towers above an E_T threshold of 1 GeV within $|\Delta\eta| < 0.5$ and $|\Delta\phi| < 0.5$ around the highest-E_T tower which has not yet been assigned to a precluster. The axis of the jet is defined as the E_T weighted centroid. Some cells may contribute to more than one jet. If the fraction of the energy shared by two jets is more than 50% of the energy of the highest E_T jet, the two jets are merged and a new jet axis is defined using all the cells in the merged jet. If the fraction of energy shared is less than 50%, the two jets are considered separate jets and each shared cell is assigned to the closest jet. A threshold of 8 GeV is required for the E_T of the jets. However, response of the calorimeter is non-linear for low energy (< 2 GeV) particles and the sum of the calorimeter responses does not give the correct total energy. Moreover, a hadronic shower may develop beyond the jet cone. Corrections are applied to take these effects into account [26].

The jet energy resolution is expressed by:

$$\left(\frac{\sigma}{E_T^j}\right)^2 = C^2 + \frac{S^2}{E_T^j} + \frac{N^2}{E_T^{j\,2}}$$

where C,S, and N are constants depending on the calibration error, the shower fluctuations in the sampling gap and the detector noise respectively. The values of these constants obtained from data are:

$C = 0.010 \pm 0.005$, $S = 0.74 \pm 0.07$ $(\text{GeV})^{\frac{1}{2}}$, $N = 2.16 \pm 0.22$ GeV.

4.4 Missing Transverse Energy

According to the conservation of transverse momentum, the sum of the transverse momenta of all the particles produced by $p\bar{p}$ collisions should be zero. If the total transverse momentum is significantly different from zero, the difference is attributed to neutrinos escaping the detector. In order to calculate the transverse energy of the neutrinos, a vector $\vec{E}_T$ is assigned to each calorimeter cell, whose magnitude is the measured energy in the cell and it points

from the interaction vertex to the center of the cell. Then the calorimeter missing E_T is defined as:

$$\vec{\not\!\!E}_T^{\,cal} \equiv - \sum_{all\ cells} \vec{E}_{cell}.$$

Since muons deposit small amounts of energy in the calorimeter, the transverse momenta of all good muons should be subtracted from $\not\!\!E_T{}^{cal}$ to get the total transverse missing energy, $\vec{\not\!\!E}_T$. Also, since all the objects in the calorimeter contribute to $\not\!\!E_T{}^{cal}$ any mismeasurement in the energy of these objects would cause a mismeasurement in $\not\!\!E_T{}^{cal}$. Therefore $\not\!\!E_T$ is also corrected when any correction is applied to any of the calorimeter objects.

The $\not\!\!E_T$ resolution has been studied using the QCD dijet data samples. The $\not\!\!E_T$ resolution is parametrized as follows [27] :

$$\sigma = a + bS_T + cS_T^2,$$

where S_T is the summed transverse energy in the calorimeter and

$a = 1.89 \pm 0.05$ GeV, $b = (6.7 \pm 0.7) \times 10^{-3}$, $c = (9.9 \pm 2.1) \times 10^{-6}$ $(\text{GeV})^{-1}$.

4.5 Monte Carlo Simulation

In order to optimize the selection criteria to be efficient for selecting signal events and rejecting background, one needs a model for the final states expected from both signal and background events. For some sources of background (mainly those arising from detector effects, like hadronic jets being misidentified as electrons), the model is provided by the collider data sample. On the other hand, most other sources of background and the signal must be simulated using Monte Carlo programs which model both the physics of the event production and the detector response.

The first step in the simulation is the event generation; physics events are generated according to theoretical calculations and phenomenological models. The second step is the simulation of the detector response to the generated events. Finally, the simulated events are reconstructed and analyzed as if they were collider data. Since there is an uncertainity about how well the calculational model corresponds to what is happening in the experiment, a major effort is made to check the Monte Carlo using data and direct determination of the background from data.

4.5.1 Generators

ISAJET

The ISAJET [28] Monte Carlo program is the default event generator used at DØ to simulate the $p\bar{p}$ collisions and to model the hard parton-parton scattering processes. The simulation algorithm incorporates perturbative QCD cross sections, leading order QCD radiative corrections for initial and final state partons, and phenomenological models for hadronization. ISAJET event generation process follow four distinctive steps:

- **Hard Scattering:** The initial step is the calculation of the $p\bar{p}$ cross sections for partons i and j to (inclusively) produce parton k, from the QCD perturbative leading order two body scattering interaction

$$\sigma_{ij\to k} = \int dx_i \int dx_j f_i(x_i, Q^2) f_j(x_j, Q^2) \hat{\sigma}_{ij\to k}$$

  where $x_i = p_i/p$ is the momentum fraction of parton i, Q^2 is the momentum transfer, $f(x, Q^2)$ is the parton density distribution function, and $\hat{\sigma}_{ij\to k}$ is the cross section calculated in QCD perturbation theory.

- **QCD Radiative Corrections:** After the primary hard scattering is generated, QCD radiation is added to the model in order to obtain the correct event structure. The radiation of photons, W's and Z's from the final state quarks are also included in the same approximation as QCD radiation.

- **Jet Fragmentation:** Colored quarks and gluons fragment into colorless hadrons when ejected into free space. Fragmentation is governed by soft non-perturbative processes that cannot be calculated apiori. ISAJET uses the Feynman-Field fragmentation model [29] to simulate the process. In this fragmentation model, a quark generates quark-antiquark pairs by the color force with the ratios $u : d : s :: 0.43 : 0.43 : 0.14$. These numbers show the smaller probability for the production of the heavier s quark.

- **Beam Jets:** The remaining feature of $p\bar{p}$ collisons is the underlying event, defined as the interactions of the incident partons which do not participate in the hard scatterring. The underlying event model is based on the experimental observation of minimum-bias events, which show that the multiplicity of the charged clusters follow a negative

binomial distribution. The hadronization of the cluster is modeled in the same manner as for the final state clusters.

HERWIG

The HERWIG Monte Carlo program follows the same steps as ISAJET, but HERWIG adopts the cluster hadronization model to handle the fragmentation process.

HERWIG models the fragmentation by assuming that the hadronization process occurs between locally color-connected partons and is independent of the scale of the hard process. In particular, all of the final state gluons are split into light quark pairs, and the color lines are followed to form color-singlet clusters of partons. If a cluster is too light to decay into hadrons, it is assumed to represent the lightest hadron of its flavor. Otherwise, the cluster is fragmented into two or three hadrons selected at random from those compatible with the flavor of the cluster. Any unstable hadrons resulting from this process are assumed to decay to final state particles according to their measured branching ratios.

VECBOS

In addition to ISAJET and HERWIG, the VECBOS Monte Carlo program [30] is used to study the kinematics of the W+jets background. VECBOS is a parton level program using exact tree-level matrix elements for W or(Z) + njets processes, where $1 \leq n \leq 4$. To generate events one has to specify the value of n, so each order has to be generated separately. The VECBOS program processes the interaction of the incoming partons to produce W/Z bosons plus a definite number of jets in the final state. We then have to use a separate model to add the underlying event, initial and final state radiations, and to model the hadronization of the final state partons. For most of the studies, the HERWIG program is used. As a cross-check, ISAJET was also used to model these processes.

SPYTHIA

SPYTHIA is the supersymmetric extension of the program PYTHIA 5.7 [32] Monte Carlo program. SPYTHIA simulates $2 \rightarrow 2$ and $2 \rightarrow 3$ body processes involving particles in the Minimal Supersymmetric Standard Model (MSSM) at $p\bar{p}$ machines. Final state partons are hadronized using a string hadronization model [32].

4.5.2 Detector Simulation

The DØ detector simulation program, DØGEANT [24], is a customized version of the CERN GEANT2 [25] program. It is used to simulate the response of the detector to the particles generated by the Monte Carlo programs by taking into account the physics processes involved, including $\delta-$ray production, multiple coulomb scattering, full electromagnetic and hadronic showering, electron and muon bremsstrahlung, and particle decays. Since such a detailed simulation is extremely CPU intensive, it would not be possible to obtain the Monte Carlo statistics necessary for analysis by using the full power of GEANT. Hence a compromise is reached by running the full GEANT simulation on the large sample of electrons, hadrons and muons, and storing the resultant showers in a library (called SHOWERLIBRARY) [33]. When new Monte Carlo events are sent through the simulation, a shower is selected from the library to model the response of each particle. The total energy of the shower is scaled by the ratio of energy of the particle to be simulated to that of the library particle which created the shower.

The Monte Carlo produces single events, while in the actual data there is the possibility of multiple $p\bar{p}$ interactions during the same beam crossing. In order to account for this effect, parton level ISAJET minimum bias events are added to the parton level Monte Carlo events before passing them through DØGEANT.

To further model the response of the Level 1 and Level 2 triggers, the utilities L1SIM and L2SIM are used. L1SIM simulates the Level 1 hardware trigger and L2SIM uses the same code as is used in the online Level 2 software filter.

Once the detector response has been simulated, the event is stored in a format identical to that for actual data, and it is processed by DØRECO to reconstruct various objects (electrons, muons and jets). The only difference between the data and Monte Carlo event reconstruction code is that the determination of the z vertex is not done in the latter, since the shower library procedure doesn't simulate particle tracks. The Monte Carlo samples are generated with the distribution of z vertices similar to that of the data sample, and the reconstruction makes use of this generated vertex.

CHAPTER 5

MEASUREMENT OF $t\bar{t}$ CROSS SECTION

At DØ, the $t\bar{t}$ production cross section is measured using both leptonic decay channels, where at least one of the W bosons decays leptonically, and the hadronic decay channel, where both the W's decay into jets. The leptonic decays of $t\bar{t}$ events are divided into two broad categories: the lepton+jets and dilepton modes, depending on whether one or both the W bosons decay into lepton-neutrino pairs. The lepton+jets decay channels have the advantage of higher branching fractions, accounting for about 30% of all $t\bar{t}$ decays with the disadvantage of higher backgrounds; whereas dilepton channels have lower backgrounds but account for only 5% of all decays.

In this chapter all the leptonic decay channels, except the channels involving τ leptons, will be discussed. The dilepton channels results will be summarized for the ee, $\mu\mu$ and $e\mu$ channels. The lepton + jets channels results will be summarized for analyses using topological cuts and the $\mu-$tag requirement to enhance the signal to background ratio for the both $e+$ jets and $\mu+$ jets channels. In addition to these channels, the $e\nu$ channel will also be discussed. This channel has acceptance in regions of phase space rejected by other channels. All eight channels discussed in this in dissertation are listed in Table 5.1 (counting the lepton + jets analysis involving the $\mu-$tag as a different channel from the analysis requiring topological cuts). Only the $e+$ jets channel with topological cuts will be discussed in detail.

Since in leptonic channels there is at least one W boson decaying into a lepton (l) and a neutrino (ν), we look for events with: an isolated high E_T lepton, high $\not\!\!E_T$, and high E_T jets coming from the b-quark and the hadronic decay of the second W boson.

5.1 Data Sample

The data used for this analysis was collected between 1992 and 1996. The total luminosity used by all the channels is listed in Table 5.1. The total luminosity is different for different channels for three main reasons: 1) The muon triggers were not fully efficient at the beginning of the run, leaving channels which require muons with slightly lower luminosity, 2) the analysis of different decay channels place different cuts on the type of main ring activity allowed, and 3) the last period of running in early 1996 is not included by some analyses.

Channel	Luminosity (pb^{-1})
ee	125.3
$e\mu$	108.3
$\mu\mu$	104.5
e+jets (topol.)	115.0
e+jets (μ tag)	103.7
μ+jets (topol.)	108.3
μ+jets (μ tag)	104.0
$e\nu$	115.0

Table 5.1: Integrated luminosity of the different analysis channels of $t\bar{t}$ decay. There is a 5.3% uncertainty on the luminosity measurement.

5.2 Event Cleanup

Several steps are taken to ensure that the data sample is not contaminated by events arising from detector pathologies. A list of runs with known problems is kept, and no events from these runs are used. If for any jet in the event the difference between the fractions of the jet energy in the coarse hadronic and electromagnetic calorimeters is greater than 0.5 (typical of Main Ring energy deposition), the event is discarded.

Since the Main Ring (MR) passes through the DØ detector, events which were recorded during the periods when Main Ring was active were further processed to correct

for Main Ring energy deposition and included in the analysis only for some of the decay channels. Finally, as a general cleanup procedure during DØRECO, large hadronic deposits in isolated cells ("hot cells") are removed.

For final selection of events for the $e+$jets channel, we have used the events taken during the periods when the MR was active after correcting for energy depositions in the region of the MR. However, for estimating backgrounds, we have only used the events taken during the periods of no MR activity, as otherwise it would have involved reprocessing of a large amount of data to correct for the MR activity. The estimated backgrounds are then raised to take into account the increased luminosity due to the inclusion of events taken during the periods of MR activity in the final selection.

5.3 Online Event Selection

An event is entered into our data sample if it passes either one of the two Level 2 filters listed in Table 5.2 for the corresponding periods of data taking (Run 1A or 1B and 1C) which correspond to 3 periods of running of the Tevatron between 1992 and 1996. We outline in Table 5.2 the specific definitions of the two triggers (filters) used to select data for this analysis. All the triggers listed in the table require at least one electromagnetic (EM) cluster in the calorimeter with or without additional jet or $\not\!\!E_T$ requirements.

All these triggers were stable throughout the data taking. The $\not\!\!E_T$ threshold and the E_T cutoff of the electron in the EM1_EISTRKCC_MS were more restrictive than those in the ELE_JET_HIGH, but EM1_EISTRKCC_MS is used to improve the efficiency for low jet multiplicity events. The trigger efficiency of the combination of the two triggers for $t\bar{t}$ decays is $\approx 98\%$ as discussed later in section 5.6.1 for both run 1A and 1B/1C.

Because different trigger definitions are used for run 1A and 1B/1C, backgrounds for run 1A and 1B/1C are computed separately.

5.4 e+jets Event Selection

Since the data set for the $t\bar{t} \to e+$ jets events is a subset of that for inclusive $W \to e\nu$ production, we select events with an isolated high E_T central electron and significant $\not\!\!E_T$. The electron candidates must pass the quality cuts described in section 4.2.1. The following W boson selection criteria are applied:

Trigger Name	Level 1	Level 2
Run 1A		
ELE_HIGH	$\geq$ 1 EM cluster $E_T^e > 10$ GeV	$\geq$ 1 EM cluster $E_T^e > 20$ GeV
ELE_JET	$\geq$ 1 EM cluster $E_T^e > 10$ GeV $\|\eta^e\| < 2.5$	$\geq$ 1 EM cluster $E_T^e > 15$ GeV $\|\eta^e\| < 2.5$
	$\geq$ 1 Jet $E_T^j > 5$ GeV	$\geq$ 1 Jet $E_T^j > 10$ GeV $\|\eta^j\| < 2.5$
		$\not\!\!E_T > 10$ GeV
Run 1B and 1C		
EM1_EISTRKCC_MS	$\geq$ 1 EM cluster $E_T^e > 12$ GeV	$\geq$ 1 EM cluster $E_T^e > 20$ GeV
		$\not\!\!E_T > 15$ GeV
ELE_JET_HIGH	$\geq$ 1 EM cluster $E_T^e > 12$ GeV $\|\eta\| < 2.6$	$\geq$ 1 EM cluster $E_T^e > 15$ GeV $\|\eta^e\| < 2.5$
	$\geq$ 1 Jet $E_T^j > 5$ GeV	$\geq$ 1 Jet $E_T^j > 10$ GeV $\|\eta^j\| < 2.5$
		$\not\!\!E_T > 14$ GeV

Table 5.2: Summary of triggers used in this analysis.

- The electron E_T and $\not\!\!E_T$ threshold: The E_T distribution of the leptons from real W decay is expected to peak at about 40 GeV ($\sim$ half the W mass), leading us to use following thresholds:

$$E_T^e \ > \ 20 \text{ GeV}$$

$$\not\!\!E_T \ > \ 25 \text{ GeV}.$$

The $\not\!\!E_T$ cut is slightly stronger than the E_T^e cut. Unlike electrons for which we can make quality requirements to pick a clean sample, we have no tools available for selecting

neutrinos.

- The η range of the electron: Most of the background to the leptonic W comes from hadronic jets which are misidentified as electrons in the calorimeter. This "fake" electron problem is more severe in the forward region of the calorimeter, limiting the useful η range. Moreover the electrons from W and $t\bar{t}$ decay tend to be more central, so we require the electrons to satisfy

$$|\eta^e| \ < \ 2.0$$

  without any significant loss in efficiency. Since there is no EM coverage in the region of the Inter Cryostat Detector (ICD), along with the above η range, electrons are also required to have $|\eta_d| < 1.2$ or $|\eta_d| > 1.5$ where η_d refers to "detector η", which is pseudorapidity calculated using $z = 0$ for the vertex.

- Events with two or more electrons passing the kinematic cuts are rejected as they are possibly a Z boson, W^+W^-, or $t\bar{t} \to ee$ candidates.

- We require at least 4 jets[1] in the event. The jets are required to satisfy following selection criteria:

$$E_T^j > 15 \text{ GeV} \ \ \& \ \ |\eta^j| < 2.0$$

5.5 Backgrounds

The major sources of backgrounds in the $t\bar{t} \to e +$ jets channel are:

- The non-W background (also known as QCD multijet or *"fake electron"* background): This background is due to detector effects, when a jet in an event is misidentified as an electron and the event also has a significant $\not\!\!E_T$ due to mismeasurement.

- The $W +$ jets background: This is the real physics background, which arises because of the direct QCD production of jets with a W boson, where the W decays to an electron and a neutrino. Such events have the same final state as that of the $t\bar{t} \to e +$ jets decay mode.

---

[1] We start by selecting events with at least one jet, as we need the jet multiplicity distribution for $e +$ jets events to estimate the background from QCD production of the W boson discussed later in section 5.5.2.

5.5.1 Estimation of non-W background

We estimate the amount of non-W background as function of jet multiplicity. This background was estimated from the data itself. The method uses the $\not\!\!E_T$ spectrum of events with an electromagnetic cluster and jets. Such a sample was obtained from the trigger that we are using for the analysis. The sample is divided into two subsamples depending on the quality of the EM cluster, such that one subsample consists of almost no real electrons ("fake sample") while the other is enriched in electrons ("electron sample"). To select the "electron sample", we apply the same quality and kinematic cuts to electrons as for our signal sample. To select the "fake sample", the kinematic requirements on the fake electron are kept the same, but we require that the fake electron has:

- H-matrix $\chi^2 > 200$ and
- track match significance, $S > 10$.

These anti-electron cuts make sure that we have very little electron contribution in our "fake sample" and the sample is dominated by those events where jets are identified as electrons. Figure 5.1 shows the $\not\!\!E_T$ spectrum for the two samples. It is observed that at low $\not\!\!E_T$, where both samples are dominated by the $\not\!\!E_T$ resolution of the detector, the shape of the $\not\!\!E_T$ distribution is the same. At high $\not\!\!E_T$, the shape of the fake sample is due to detector resolution effects, whereas in the electron sample the high $\not\!\!E_T$ region is dominated by the $W \to e\nu$ events. We can use the shape of the $\not\!\!E_T$ spectrum for the fake sample, normalized to that of the electron sample in the low $\not\!\!E_T$ ($\not\!\!E_T < 12$ GeV) region to estimate the contribution of QCD multijet events in the electron sample at higher $\not\!\!E_T$. Details of this method can be found in [34]. Table 5.3 lists the non-W background in the $e+$ jets sample as a function of jet multiplicity for both run 1A and 1B/1C.

5.5.2 $W(\to e\nu)+$ jets Background

Once we have estimated the non-W background in our $e+$jets sample, we can estimate the W background by exploiting a noteworthy feature of our data, namely the simple exponential behavior of the number of events as function of jet multiplicity (this behaviour is predicted by Monte Carlo generation of $W+$ jets events). Theoretical expectations [30] for $W+$ jets

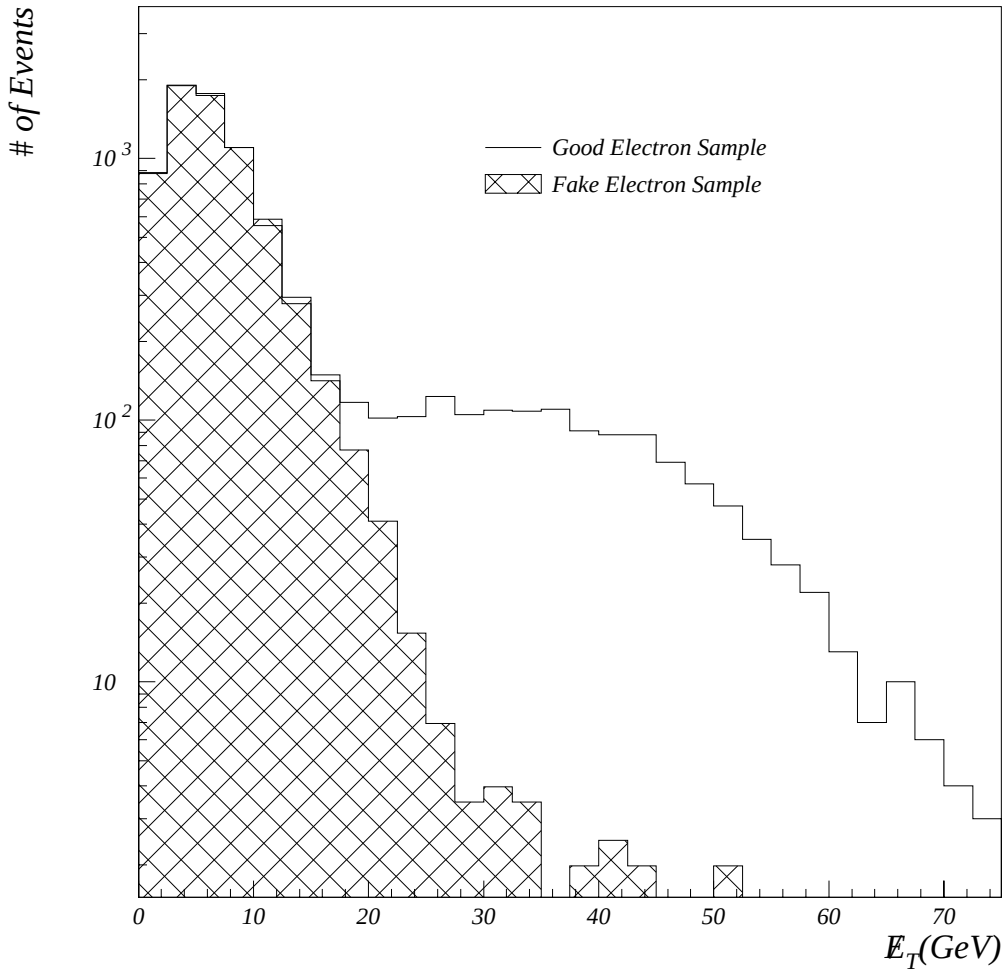

Figure 5.1: The $\not\!\!E_T$ distribution for the good electron and "fake" electron sample. The two distributions are normalized to same number of events for $\not\!\!E_T < 12$ GeV.

events suggest that the ratio of number of events when the jet multiplicty increases by one should be roughly constant, i.e,

$$\frac{N_n}{N_{n-1}} = \alpha \text{ (const. independent of } n)$$

where N_n is the number of events with n or more jets. Using this scaling rule (called the Berend's scaling rule), we can predict number of events with three (four) or more jets if we know the number of W events with one or more and two or more jets. Figure 5.2 shows

# of Jets	# of Events observed (N_{total})	Non-W Bkg. (N_{QCD})	$N_{total} - N_{QCD}$
RUN 1A			
≥ 1	1389	76.57 ± 3.2	1312.4 ± 51.0
≥ 2	250	24.0 ± 2.8	226.0 ± 18.9
≥ 3	37	7.1 ± 1.7	29.9 ± 7.2
≥ 4	7	1.7 ± 1.0	5.3 ± 3.0
RUN 1B and 1C			
≥ 1	7620	378.7 ± 5.3	7241.3 ± 120.3
≥ 2	1379	161.3 ± 5.1	1217.7 ± 46.8
≥ 3	250	38.0 ± 3.0	212.0 ± 19.2
≥ 4	46	8.5 ± 1.6	37.5 ± 8.0

Table 5.3: Non-W background as a function of jet multiplicity for $\not\!\!E_T >$ 25 GeV.

the jet multiplicity spectrum for three different jet E_T thresholds for data and the VECBOS Monte Carlo. Also shown in the figure are the fits to the above equation for various jet E_T thresholds. This figure shows that the Berend's scaling rule works well for both the data and VECBOS $W +$ jets samples.

To estimate how much $t\bar{t}$ production can be accomodated and still satisfy the scaling rule, we fit our $e +$ jets data after subtracting the non-W background to the following equation:

$$N_n^{obs} = N_1^W * \alpha^{n-1} + f_n * N^{top} \tag{5.1}$$

where N_n^{obs} is the number of events observed with "n" or more jets after the subtracting non-W background (column 4 of Table 5.3), f_n is the fraction of $t\bar{t}$ events expected with n or more jets (determined from Monte Carlo for $m_t = 170$ GeV/c^2) and α, N_1^W, N^{top} are the parameters obtained from the fit (ratio of multiplicities, number of $W+ \geq 1$ jet events, and total number of top events). The values of the variables obtained from the fit are listed in Table 5.4 both for Run 1A and 1B/1C. From these fits, we compute the contribution of

$W+ \geq 4$ jets in the $e+ \geq 4$ jets sample[2] using the following equation:

$$N_4^W = N_1^W \times \alpha^3.$$

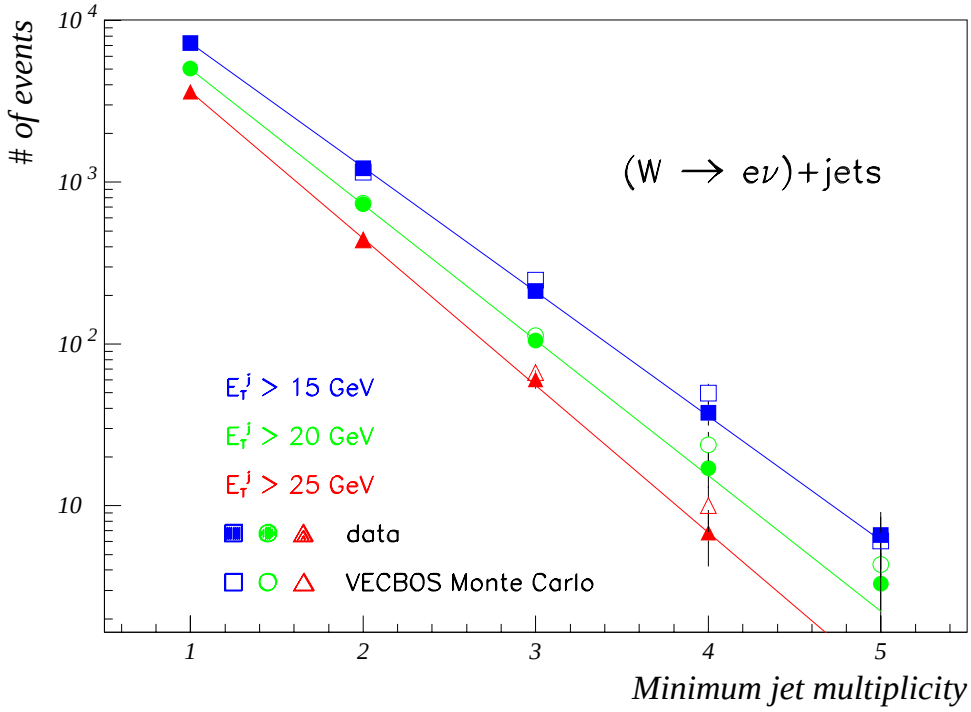

Figure 5.2: Jet multiplicty spectrum for data and the VECBOS W+jets sample for jet $E_T > 15$, 20 and 25 GeV. Also shown are the fit to the Berend's scaling rule for the data sample. The data and VECBOS distributions are normalized to have same number events with one or more jet.

5.5.3 Topological Cuts

As can be seen from Table 5.4, even after requiring 4 or more jets in the event, our data sample is still dominated by background. Figure 5.3 shows the inclusive jet multiplicity

[2] $e+ \geq 4$ jets sample here refers to events with an electron and four or more jets. This notation will also be used later in this chapter.

Data Sample	α	N_1^W	N^{top}	N_4^W
Run1A	0.160 ± 0.023	1315.7 ± 50.9	-1.3 ± 8.9	5.4 ± 2.3
Run1B and 1C	0.168 ± 0.008	7232.5 ± 118.8	7.56 ± 20.9	34.3 ± 4.9

Table 5.4: Results of the Berend's fit to the e+jets data sample.

distribution for the e+jets data sample and the $t\bar{t}$ Monte Carlo for $m_t = 170$ GeV/c^2. This plot also clearly shows that we are still far from achieving a reasonable signal to background ratio. At DØ, we use two techniques to reduce the background further: requiring a μ-tag (defined later in section 5.8.2) or making some additional topological requirements like event shape, total energy content of the event etc. This analysis uses the second approach of requiring topological cuts on the $e+ \geq 4$ jets sample.

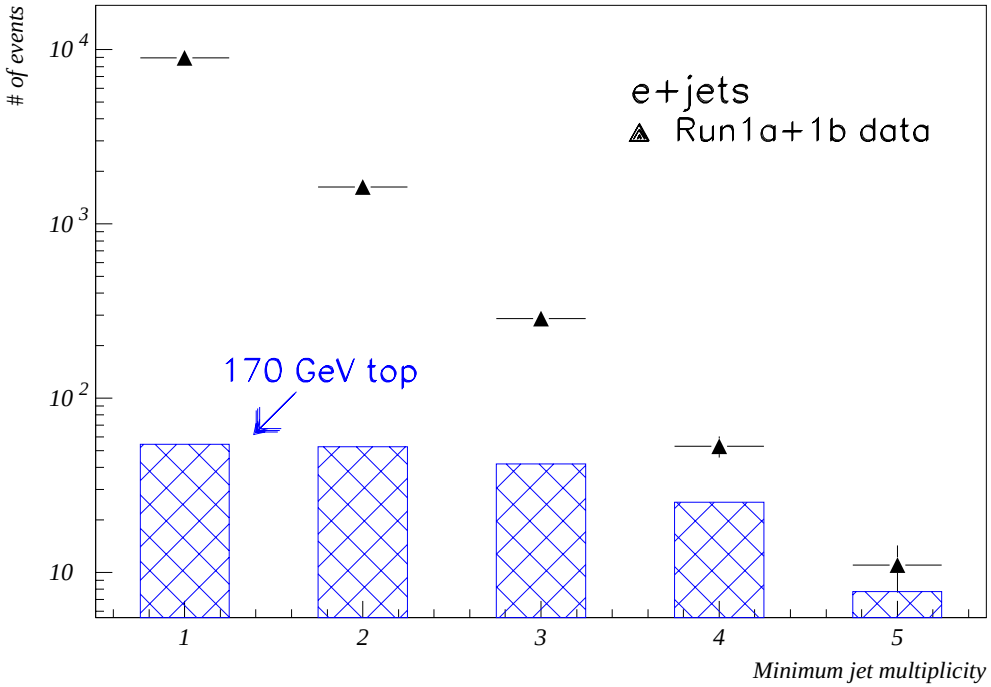

Figure 5.3: Number of e+jets events as a function of inclusive jet multiplicity, along with the expected contribution from $t\bar{t}$ production.

The variables which are found to be useful in distinguishing signal from the background are:

- H_T : Scalar sum of E_T's of all the jets in the event with $E_T > 15$ GeV and $|\eta| < 2.0$.

$$H_T = \sum_{i=1}^{n} E_T^{j_i}$$

here n is the number of jets in the event. This variable is a measure of total hadronic activity in the event.

- Aplanarity ($\mathcal{A}$) : This quantity exploits the difference in the shapes of the $t\bar{t}$ and background events. For each event we define a normalized momentum tensor ($\mathcal{M}$) with components:

$$\mathcal{M}_{ab} = \frac{\sum_i p_{ia} p_{ib}}{\sum_i {p_i}^2}$$

where p_i is the three momentum of the i^{th} object in the laboratory frame and a, b run over x, y and z components of the momentum vector. The objects used in defining the tensor are the jets and the reconstructed W boson. $\mathcal{M}_{ab}$ is the symmetric matrix which can be diagonalized, with its eigenvalues Q_j computed and ordered as

$$Q_1 \leq Q_2 \leq Q_3.$$

The following relations hold:

$$Q_1 + Q_2 + Q_3 = 1,$$

$$Q_1 \geq 0.$$

These eigenvalues can then be used to quantify the shape of the event. For roughly spherical events, $Q_1 \approx Q_2 \approx Q_3$; for planar events, $Q_1 \ll Q_2$; for linear events, $Q_2 \ll Q_3$.

Aplanarity is then defined as

$$\mathcal{A} = \frac{3}{2} Q_1$$

normalized to lie in range $0 \leq \mathcal{A} \leq 0.5$. Large values of $\mathcal{A}$ characterize spherical events. The shape of a $t\bar{t}$ event is expected to be spherical.

- L_T (Lepton E_T): This quantity is defined as the scalar sum of the electron E_T and $\not\!\!E_T$ in the event:

$$L_T = E_T^e + \not\!\!E_T.$$

Once the proper variables for distinguishing signal from background have been identified, it remains to select the ideal cut points for these variables. This is done using a *random grid search* [35] in which an array of possible cut points is tested on the signal and background models. For each prospective $(\mathcal{A}, H_T, L_T)$ cut, the expected number of signal and background events for the given data luminosity is calculated and, from this, the point which gives the minimum expected fractional uncertainty in the cross section measurement is picked. This point for $e+$jets analysis is found to be:

$$H_T > 180 \text{ GeV}$$

$$\mathcal{A} > 0.065$$

$$L_T > 60 \text{ GeV}$$

Figure 5.4 shows the scatter plot for the $\mathcal{A} - H_T$ distribution for the data, $t\bar{t}$ Monte Carlo and backgrounds.

Once these cuts are established, the expected total background can be estimated as:

$$N_{total}^{Bkg} = N^{QCD} \times f_{QCD} + N_4^W \times f_W \tag{5.2}$$

where, N^{QCD} (from Table 5.3) and N_4^W (from Table 5.4) are the expected number of events with four or more jets for the QCD multijet and W backgrounds respectively. $f_{QCD} = 0.027 \pm 0.004$ and $f_W = 0.083 \pm 0.008$ are respectively the fraction of QCD multijet and VECBOS W events with four or more jets passing the topological cuts.

The final background estimates are summarized in Table 5.5 along with the number of events observed in our data surviving all the cuts after including the events taken during the periods of MR activity. The estimated number background events are raised by 10% for run 1A and 18% for run 1B/1C to take into account the increase in luminosity due to inclusion of events with MR activity.

5.5.4 Systematic Uncertainties in the Background Determination

Since the non-W background is estimated using data, the systematic uncertainties on this background are small. The only source of systematic error arises from the uncertainty on the normalization factor between low the $\not\!\!E_T$ region for the "electron" and the "fake" sample. This uncertainty is included while estimating the error on the non-W background.

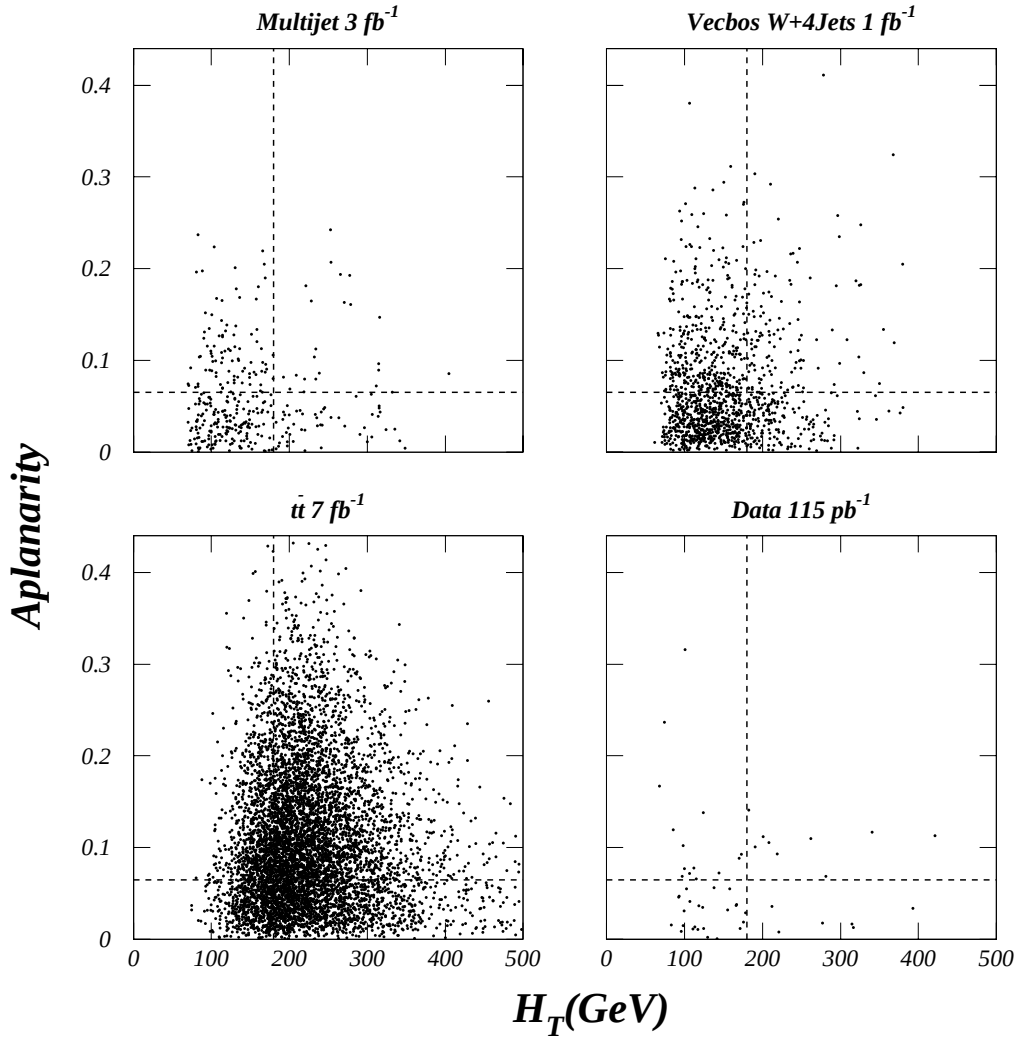

Figure 5.4: $\mathcal{A} - H_T$ distribution for non-W and W backgrounds, expected $t\bar{t}$ (m_t = 170 GeV/c^2) and data after requiring 4 or more jets in the event. The dashed line shows the cut values for aplanarity and H_T.

The W background is estimated by methods which rely on theoretical predictions and Monte Carlo techniques. Monte Carlo models may have many sources of systematic uncertainties, most notably:

- uncertainty of the Berend's scaling rule (i.e. how well the data follows this rule),
- uncertainty in the jet energy scale, and

Run	No. Events Observed	Non-W Bkg	W Bkg.	Total Bkg.
1A	2	0.05 ± 0.03	$0.49 \pm 0.24 \pm 0.09$	$0.54 \pm 0.24 \pm 0.09$
1B and 1C	8	0.27 ± 0.08	$3.36 \pm 0.68 \pm 0.63$	$3.63 \pm 0.69 \pm 0.63$

Table 5.5: Number of events observed, and expected backgrounds for run 1A and 1B/1C. The second errors on the W and total background are the systematic uncertainty. The systematic uncertainty on the non-W are included in the error.

- differences in the H_T distribution between the data and VECBOS W+jets sample.

Berend's Scaling

We examine a variety of data sets (QCD multijet, Z+jets and VECBOS W+jets) to check the validity of the Berend's scaling law. Any differences between the observed and predicted number of events are then assigned as the systematic uncertainty on the W background. We can predict the number of events with $\geq n$ jets by using the number of events with $\geq n-1$ and $\geq n-2$ jets for all these data sets using the Berend's scaling rule:

$$\frac{N_n}{N_{n-1}} = \alpha = \frac{N_{n-1}}{N_{n-2}}$$

or

$$N_n = \frac{N_{n-1}^2}{N_{n-2}}$$

Table 5.6 shows the observed number of events and number of events predicted using the Berend's scaling rule for the QCD multijet, Z+jets and VECBOS sample.

For this study, the QCD multijet sample was selected by requiring events with at least one jet with $E_T > 20$ GeV and the same η requirements as for electrons in our data sample, $\not\!\!E_T > 25$ GeV and additional jets with $E_T > 15$ GeV. The number of events observed for a given jet multiplicity is then corrected for the probability of the event to be identified as an $e+$jets event. This probability is related to the number of jets in the event which satisfy the same E_T and η requirements as that for an electron, (e.g. an event having two jets with $E_T > 20$ GeV and $|\eta| < 2.0$ has twice the probability of being identified as an $e+$jets events as compared to the event with one such jet). To obtain this correction factor, we count the the number of jets with $E_t > 20$ GeV and $|\eta| < 2.0$ ($N_{\rm jet\,20}$) in this sample and define this

Event sample	Jet Mult.	Observed # of Events	Correction Factor	Corrected # Events	Predicted # of Events	Fractional Difference
QCD multi-	≥ 1	21566	1.0	21566.0		
jet	≥ 2	8925	1.6	5578.1		
	≥ 3	2796	1.9	1471.6	1442.8	0.02
	≥ 4	774	2.2	351.8	388.2	0.10
Z+Jets	≥ 0	1697				
	≥ 1	265				
	≥ 2	40			41.4	0.04
VECBOS	≥ 2	11.6				
W+Jets	≥ 3	2.4				
	≥ 4	0.5			0.5	0.00

Table 5.6: Number of events observed and predicted using the Berend's scaling rule for various data sets.

factor as:

$$\text{Correction factor} = N_{\text{jet}\,20}/(\text{total number of events})$$

The correction factor is then normalized to unity for events with at least one additional jet with $E_T > 15$ GeV.

For the Z+jets sample, because of small number of events with $Z + 3$ or more jets, we use $Z + 0$, $Z + 1$ and $Z + 2$ jet events to test the predictions of the scaling rule. The Z events used for this study are selected by requiring two high E_T ($E_T > 20$ GeV) electrons satisfying our electron quality requirements. For testing the validity of the Berend's scaling rule in the VECBOS Monte Carlo sample, we have used the number of events expected/pb^{-1}.

In addition to these data sets, we also tested the validity of the Berend's scaling rule for the photon+jets sample. In this sample the predictions of the Berend's scaling rule hold to better than 5%.

For all the data sets, the QCD multijet sample shows the maximum difference between observed and predicted number of events. To take into account the differences in the observed and predicted number of events using the Berend's scaling rule, we assign 10% systematic uncertainty to our estimate of the W background.

Jet Energy Scale

This uncertainty arises because of the difference in the jet energy scale between data and Monte Carlo. Since the non-W background is estimated from the data, it is not affected by this difference, but the jet energy scale can affect the W background estimate in two ways : it can change the fraction, f_n (eqn. 5.1), of the $t\bar{t}$ events for a given jet multiplicity, which can change the amount of the W background before topological cuts; and it can also change the fraction, f_W (eqn. 5.2), of VECBOS $W + 4$ jets events passing the $\mathcal{A} - H_T$ cut.

To estimate this uncertainty, we apply the nominal, high (one standard deviation above nominal) and low (one standard deviation below nominal) energy corrections to our Monte Carlo sample. Table 5.7 shows the fraction f_n and f_W for events with four or more jets for the $t\bar{t}$ and VECBOS $W +$ jets Monte Carlo samples.

	Jet energy corrections		
	Low	Nominal	High
f_3	0.74	0.75	0.76
f_4	0.43	0.44	0.45
W Bkg. before topological cut	34.3	34.3	34.4
f_W	0.082	0.083	0.087
W Bkg. after topological cuts	2.81	2.85	2.99

Table 5.7: Effect of the difference in the jet energy scale between data and Monte Carlo on f_n and f_W, and the W background before and after applying topological cuts. Here f_n is the fraction of $t\bar{t}$ events with n or more jets ($n = 2, 3$) and f_W is the fraction of VECBOS $W+ \geq 4$ jets events passing the topological cuts.

From Table 5.7, we can see that if the jet energy correction is changed by one standard deviation around its nominal value, the W background changes at most by $\sim 5\%$. We assign 5% systematic uncertainty on our W background to take into account the differences in the energy scale between data and Monte Carlo.

H_T Shape Difference between Data and VECBOS

The systematic uncertainty in the estimate of the W background due to differences in the shapes of the H_T distribution for data and VECBOS e + jets events can be determined by comparing the H_T distribution for data and VECBOS for the events with four or more jets. For comparing the H_T distribution between data and VECBOS, the top and non-W background contributions are added to the VECBOS sample in the appropriate proportions. The number of $t\bar{t}$ events added to the VECBOS sample are equal to the number of events expected for the given jet multiplicity using theoretical cross sections for $m_t = 170$ GeV/c^2. Due to limited number of $e+ \geq 4$ jets events in the data, we estimate this uncertainty by comparing the H_T per jet (H_T/jet) distribution for the events with two or more jets and for events with three or more jets for data and VECBOS and extrapolating the results to the events with ≥ 4 jets. To use H_T/jet instead of H_T, we pick a value of H_T/jet cut, which gives the same signal to background ratio as the H_T cut of 180 GeV. This cut corresponds to H_T/jet ~ 44 GeV. If we compare the mean of the H_T/jet distributions for the data and VECBOS sample, this difference is less than 4% (Fig. 5.5-5.6). Figure 5.7 shows the ratio of number of events observed to the number of events predicted using the VECBOS sample, passing the given H_T/jet cut for events with two or more jets and for events with three or more jets. As can be seen from the Fig. 5.7, the fractional difference of the number of events passing the H_T/jet > 44 GeV between the data and VECBOS sample is 6%(10%) for events with two(three) or more jets. By extrapolating the results from the H_T/jet shape comparison for events with two or more jets and for events with three or more jets to events with four or more jets, we expect the difference to be $\sim 15\%$, which is assigned as a systematic uncertainty to the W background to take into account the effect of the difference of H_T distributions for data and VECBOS W sample.

Table 5.8 summarizes the various systematic uncertainties in the estimate of the W background.

5.6 Signal Acceptances

To calculate the efficiency for $t\bar{t} \rightarrow e +$jets events, we simulate top pair production and their subsequent decay using the HERWIG Monte Carlo program. Since the branching ratio of $t\bar{t}$ decays to $e +$ jets is only about 15%, to get reasonable statistics one must generate a large

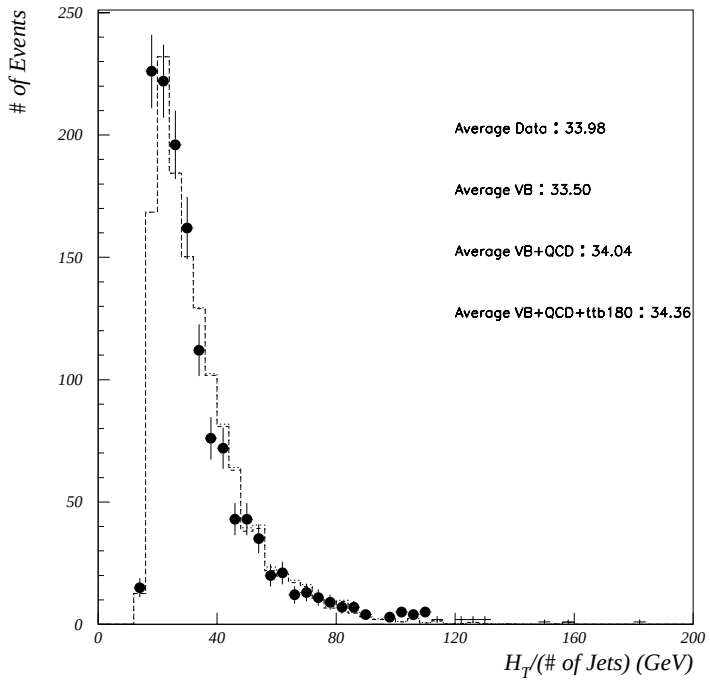

Figure 5.5: Comparison of the H_T/jet distribution for data and Monte Carlo, for events with $\geq$ 2 jets. Solid dots are for data, dashed histogram is for VECBOS with QCD multijet contribution added and the dotted histogram is for VECBOS with QCD multijet and $t\bar{t}$ contribution added in appropriate proportions.

Source of uncertainty	% error
Berend's scaling	10%
Jet energy scale	5%
H_T shape difference	15%

Table 5.8: Systematic uncertainties in the estimation of the W background.

number of events. To avoid this problem, in our Monte Carlo program we force that one of the W bosons from the $t\bar{t}$ decay decays into a lepton-neutrino ($e\nu$, $\mu\nu$, or $\tau\nu$) pair. This way, one needs to generate a much smaller number of Monte Carlo events. These Monte Carlo events are run through the GEANT-based DØ detector simulation program (DØGEANT)

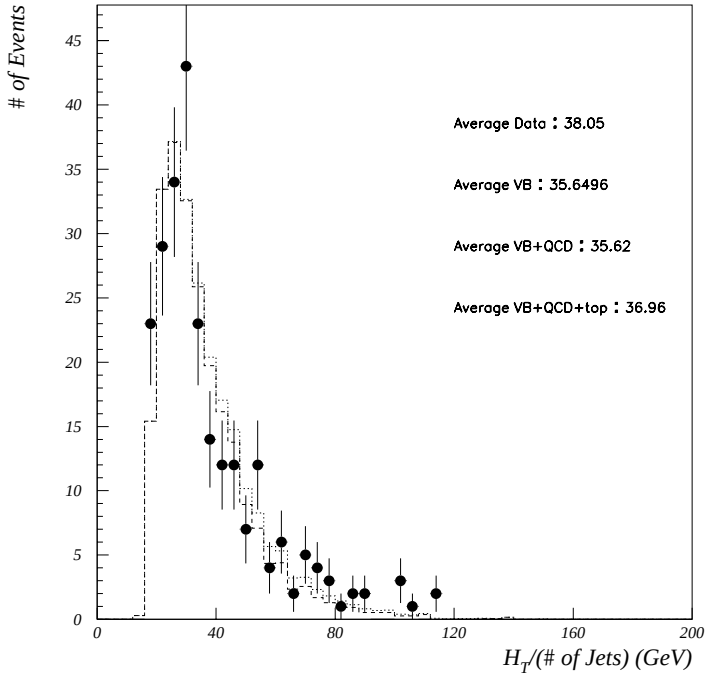

Figure 5.6: Comparison of the H_T/jet distribution for data and Monte Carlo, for events with $\geq$ 3 jets. Solid dots are for data, dashed histogram is for VECBOS with QCD multijet contribution added and the dotted histogram is for VECBOS with QCD multijet and $t\bar{t}$ contribution added in appropriate proportions.

to model the detector response. Since detailed simulation of each event is time consuming and CPU intensive, we have used the SHOWERLIBRARY (see section 4.5.2) to simulate the detector effects. The output events from the DØGEANT program are then reconstructed using the same reconstruction program as is used for the data (DØRECO).

The efficiency for detecting $t\bar{t}$ events can be factorized into: trigger efficiency $\epsilon_{\rm trig}$ and offline identification and kinematic requirement efficiency $\epsilon_{\rm offline}$. The trigger efficiency can be determined directly from the data by comparing the different triggers. The offline efficiency is determined from the events generated using HERWIG Monte Carlo.

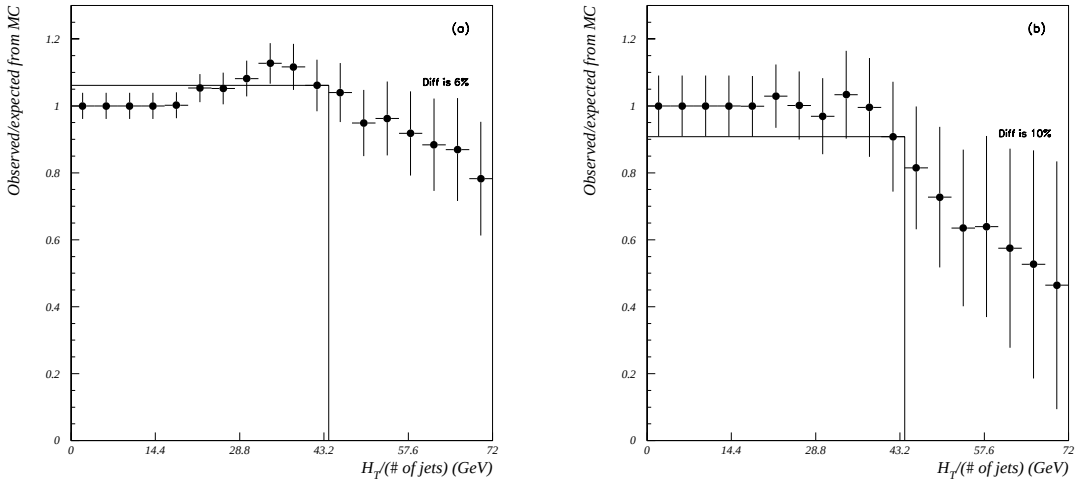

Figure 5.7: Ratio of number of events passing the H_T/jet cut for Data and VECBOSsample, (a) for ≥ 2 jets and (b) for ≥ 3 jets.

5.6.1 Trigger Efficiency

To measure the trigger efficiency for the set of two triggers used in the analysis (listed in Table 5.2), we factor triggers into the electron, $\not\!\!E_T$ and jet parts, measure the efficiency of a given part and then combine the results.

To measure the efficiency of the electron requirement in the trigger, we preselect the $e+$jets events by making all our electron identification and kinematic cuts (except the topological cuts) using a MISSING_ET trigger which requires $\not\!\!E_T > 30$ or 40 GeV and makes no other requirement. We then count how many of these $e+$jets events satisfy any of the electron triggers used in this analysis. We find the efficiency for finding an electron by "ELE" (ELE_HIGH and ELE_JET_HIGH) and "EM" (EM1_EISTRKCC_MS) triggers to be $98.7 \pm 0.1\%$ and $95.6 \pm 0.2\%$ respectively.

To measure the $\not\!\!E_T$ efficiency, we preselect $e+$jets by requiring all the offline cuts using an electron monitor (ELE_1_MON) trigger, which simply requires an electron with $E_T > 16$ GeV, and impose Level 2 $\not\!\!E_T$ requirements. For a Level 2 $\not\!\!E_T$ requirement of 15 GeV, we find the efficiency to be $99.1 \pm 0.1\%(99.6 \pm 0.1\%)$ for offline $\not\!\!E_T$ cut of 20 (25) GeV.

To measure the jet trigger efficiency, we start with the W events which fire ELE_HIGH

(or EM1_EISTRKCC_MS) and have 4 or more jets and then count the number of events passing the ELE_JET (ELE_JET_HIGH) trigger for run 1A (1B/1C) data samples.

The combined efficiency for the triggers used in this analysis for run 1A and 1B/1C can be obtained by combining the electron, $\not\!\!E_T$ and jet efficiencies. The total trigger efficiencies obtained this way for run 1A and 1B/1C events with four or more jets are $97.8 \pm 1.8\%$ and $98.2 \pm 4.4\%$ respectively.

5.6.2 Offline Efficiency

We used the HERWIG 5.7 Monte Carlo to generate $t\bar{t} \rightarrow l + \text{jets}$ events for various top quark masses (m_t =140, 150, 160, 170, 180, 190 and 200 GeV/c^2). To simulate the detector effects, we used the SHOWERLIBRARY version of DØGEANT, which does not trace the path electrons through the tracking chambers. Thus the quality of electrons generated using DØGEANT is different from the real data. However, the kinematics of the events are well modelled in the DØGEANT using SHOWERLIBRARY. For this reason, we do not apply any quality cuts to the electrons in the Monte Carlo sample and use the efficiencies given in Table 4.1, but we apply all other offline kinematic cuts to the Monte Carlo events along with the trigger efficiencies obtained above. The $\epsilon \times BR(t\bar{t} \rightarrow e + \text{jets})$ for various m_t thus obtained are listed in Table 5.10. The following systematic uncertainties are also included in the errors on $\epsilon \times BR$:

- Monte Carlo Generator: To estimate the uncertainty due to Monte Carlo modelling of $t\bar{t}$ production and decays, we compare the acceptance for events generated by HERWIG 5.7 and ISAJET 7.13. The difference in the acceptance is assigned as the uncertainty. This uncertainty is dependent on the top quark mass used to generate the events. This uncertainty lies between $\sim 23\%$ for $m_t = 140$ GeV/c^2 to $\sim 8\%$ for $m_t = 200$ GeV/c^2.

- Jet Energy Scale: Another major source of uncertainty is the relative energy scale for the jets between data and Monte Carlo. To measure this uncertainty, the energy correction for MC is varied by one standard deviation from its nominal value. The change in acceptance due to this change is assigned as the systematic uncertainty. This uncertainty is also dependent on the top quark mass used to generate the events. This uncertainty lies between $\sim 25\%$ for $m_t = 140$ GeV/c^2 to $\sim 6\%$ for $m_t = 200$ GeV/c^2.

- Electron Efficiency: Both electron reconstruction and offline quality cut efficiencies have been studied using the $Z \rightarrow ee$ data. The overall systematic uncertainty of 3% arises from the uncertainty in the measurement of the efficiency for the electron quality variables used in this analysis.

- Trigger Efficiency: This is the uncertainty on the trigger efficiency as described in section 5.6.1.

Table 5.9 lists the major sources of systematic error in the estimation of $\epsilon \times BR$ for the $t\bar{t} \rightarrow e + \text{jets}$ decay mode for the top quark mass of 172 GeV/c^2. The total error on $\epsilon \times BR$ is obtained by adding the statistical and systematic uncertainties in quadrature.

Source of uncertainty	% error
Event generator	8%
Energy scale	12%
Electron efficiency	3%
Trigger	4%

Table 5.9: Sources of systematic uncertainty in the determination of $\epsilon \times$ BR($t\bar{t} \rightarrow e + \text{jets}$) for $m_t = 170$ GeV/c^2.

Top Mass GeV/c^2	$\epsilon \times BR(\%)$	$< N_{top} >$
140	0.61 ± 0.17	11.91 ± 3.36
150	0.83 ± 0.20	11.12 ± 2.81
160	1.06 ± 0.19	9.98 ± 1.84
170	1.31 ± 0.19	8.80 ± 1.38
180	1.48 ± 0.18	7.14 ± 0.93
190	1.58 ± 0.17	5.54 ± 0.66
200	1.73 ± 0.16	4.49 ± 0.48

Table 5.10: $\epsilon \times BR$ and expected $t\bar{t}$ yields in the e+jets channel for various top masses. $< N_{top} >$ corresponds to an integrated luminosity of 115.0 ± 6.1 pb^{-1}.

5.7 Cross Section Measurement for e+ jets Channel

To measure the $t\bar{t}$ cross section, we assume that the excess of observed events over the expected background is due to $t\bar{t}$ production. The $t\bar{t}$ production cross section ($\sigma_{t\bar{t}}$) can then be computed as:

$$\sigma_{t\bar{t}} = \frac{N^{obs} - N^{bkg}}{(\epsilon \times BR) \times \mathcal{L}}$$

where

- N^{obs} is the total number of events surviving all cuts (from Table 5.5),
- N^{bkg} is the total expected background after all cuts (from Table 5.5),
- $\epsilon \times BR$ is the efficiency $\times$ branching ratio (from Table 5.10), and
- $\mathcal{L}$ is the total luminosity for the data sample used (115 pb^{-1}).

Table 5.11 summarizes the measured $t\bar{t}$ production cross section in the e+jets channel for various m_t.

Top Mass (GeV/c^2)	$\sigma \pm \Delta\sigma_{stat} \pm \Delta\sigma_{sys}(pb)$
140	$8.3 \pm 4.7 \pm 3.8$
150	$6.2 \pm 3.4 \pm 2.3$
160	$4.8 \pm 2.7 \pm 1.3$
170	$3.9 \pm 2.2 \pm 0.9$
180	$3.4 \pm 1.9 \pm 0.7$
190	$3.2 \pm 1.8 \pm 0.6$
200	$2.9 \pm 1.6 \pm 0.5$

Table 5.11: $t\bar{t}$ production cross section measured using the e+jets channel at DØ for range of the top quark masses.

The cross section at the DØ measured top quark mass $m_t = 172$ GeV/c^2 [36] can be interpolated using values of the cross section in table 5.11 and is found to be $3.8 \pm 2.1(\text{stat}) \pm 0.8(\text{sys})$ pb. Figure 5.8 shows the measured cross section for the e+jets channel as function

of the top quark mass. Also shown in the figure are the expected cross sections from 3 different theoretical calculations [9, 10, 11].

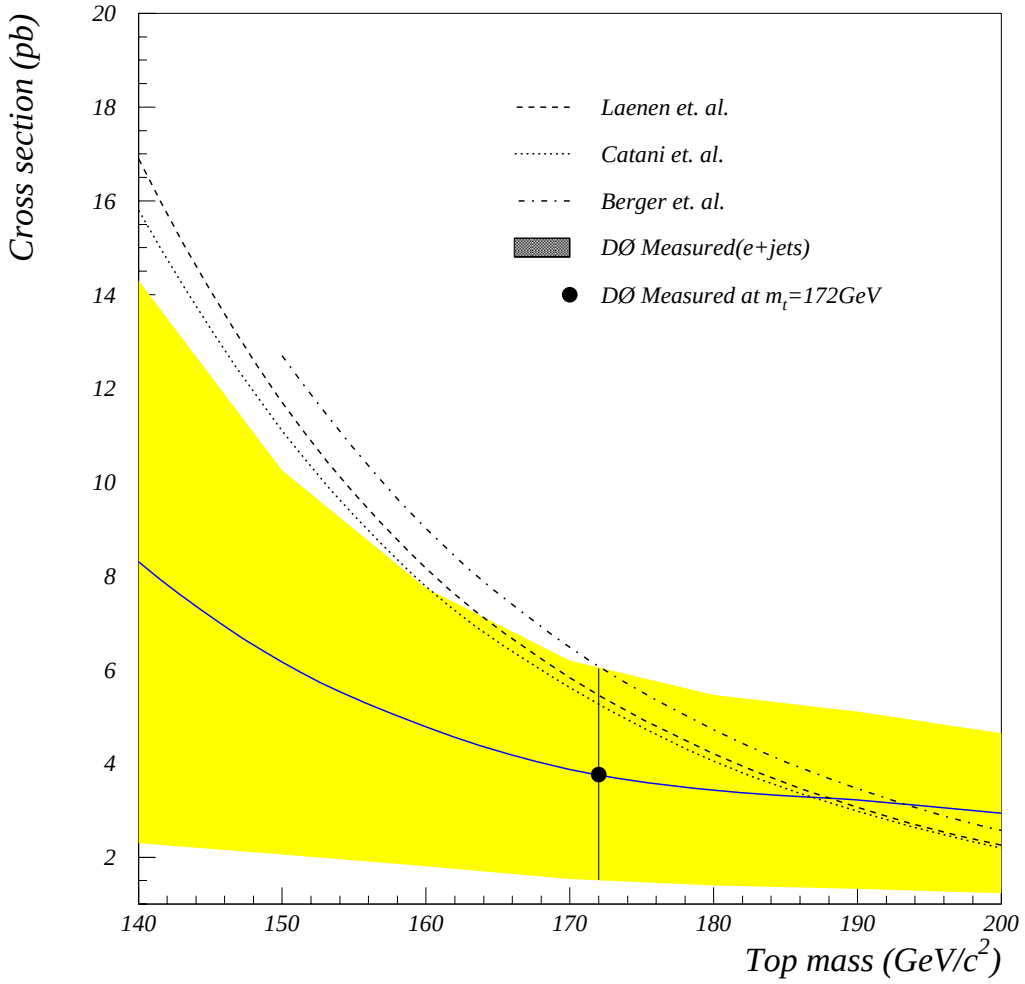

Figure 5.8: Measured cross section as a function of top quark mass. The solid line shows the central value of cross section measured using topological cuts and the lighter band shows its one standard deviation error. Also shown are various theoretical calculations.

5.8 Summary of Measurement of $t\bar{t}$ Production Cross Section at DØ

In the previous sections, the analysis for the measurement of the $t\bar{t}$ production cross section in the e+jets channel using topological cuts is described in detail. In this section, we will summarize the measurement of the cross section in other decay channels at DØ, including the e+jets $\mu-$tag analysis.

5.8.1 Dilepton Channels

Although the $t\bar{t}$ branching fraction to dileptons is small, there are also relatively few other processes which can mimic the signature of the $t\bar{t}$ decay to dileptons, which will generally have two high E_T isolated leptons, significant jet activity and $\not\!\!E_T$. This allows us to isolate the sample of events with a good signal to background ratio. The dilepton backgrounds can come from a variety of processes, none of which has a large production cross section.

The kinematic selection of the dilepton events is summarized in Table 5.12. These requirements are designed to isolate events with the expected final state signature.

	ee	$e\mu$	$\mu\mu$
Leptons	$E_T^e > 20$ GeV $\lvert\eta^e\rvert < 2.5$	$E_T^e > 15$ GeV,$p_T^\mu > 15$GeV/c $\lvert\eta^e\rvert < 2.5$	$p_T^\mu > 15$GeV/c
Jets	≥ 2 with $E_T > 20$GeV and $\lvert\eta\rvert < 2.5$		
$\not\!\!E_T$	> 25 GeV	$\not\!\!E_T > 20$ GeV $\not\!\!E_T{}^{cal} > 10$ GeV	N/A
H_T^e	> 120 GeV	> 120 GeV	> 100 GeV

Table 5.12: Kinematic requirements for the dilepton event selection. For the $\mu\mu$ channel, instead of $\not\!\!E_T$ cut, a cut (described in text) is used to reject $Z \to \mu\mu$ events. H_T^e is sum E_T's of all the jets and the leading electron in the event, for $\mu\mu$ channel H_T^e reduces to H_T used in the e+jets analysis.

The major sources of backgrounds and their expected values for all of the dilepton channels are listed in Table 5.13.

Background	ee	$e\mu$	$\mu\mu$
$Z \to ll$	0.058 ± 0.013	N/A	0.56 ± 0.22
$Z \to \tau\tau \to ll$	0.078 ± 0.025	0.099 ± 0.076	0.03 ± 0.02
W pair production	0.083 ± 0.026	0.074 ± 0.019	0.007 ± 0.004
Drell-Yan	0.054 ± 0.033	0.002 ± 0.003	0.07 ± 0.03
Instrumental	0.197 ± 0.052	0.04 ± 0.13	0.07 ± 0.03

Table 5.13: Expected background events in each dilepton channel from major sources. The nature of instrumental backgrounds differs between channel.

$e\mu$ Channel

The $e\mu$ channel is most privileged of all the dilepton channels, having twice the branching ratio as that of the ee and $\mu\mu$ channels and is free from much of the background coming from Z decay. The largest background to this channel comes from $Z \to \tau\tau \to e\mu$. Additional physics backgrounds sources are from W pair production and other rarer processes. For majority of these sources, the level of background is calculated begining with a measured cross section and corrected for the kinematic difference between the data and Monte Carlo. These are also corrected for differences in particle identification and trigger efficiencies between data and Monte Carlo. For example, by comparing the hadronic energy in DØ's $Z \to ee$ events with that in the ISAJET model of $Z \to ll$, it is found that the efficiency from the Monte Carlo must be multiplied bt 1.9 ± 1.2 to properly calculate this background.

The instrumental backgrounds in the $e\mu$ channel can arise from the misidentification of a jet as an electron. This background can arise from the W+jets events, where the W decays to $\mu\nu$ and one of the jets is misidentified as an electron. The amount of background can then be estimated by multiplying the number of W plus 3 or more jet events by the probability that a jet would satisfy the electron identification criteria.

Three events are observed in this channel, with the expected background of 0.21 ± 0.16 events [37].

ee Channel

The primary source of background in this channel is from Z boson production with additional jets produced by gluon radiation. As these events have no neutrinos, any $\not\!\!E_T$ must be due to

the detector resolution and a $\not\!\!E_T$ cut is effective in reducing this background, without having much impact on the $t\bar{t}$ acceptance. In addition to the $\not\!\!E_T > 25$ GeV cut, if the dielectron invariant mass is within 12 GeV of the Z mass, the event is required to have $\not\!\!E_T > 40$ GeV. This background is estimated entirely from data.

Besides direct decay to e^+e^-, Z bosons can also produce dielectron pairs via τ pair production, where both τ's decay into electrons. Since there is no well-defined sample in the data to study this background, it is estimated using Monte Carlo. One estimates the rejection power of the kinematic cuts against this background, which is then multiplied by known Z production cross section and $Z \to \tau\tau \to ee$ branching ratio to get an absolute prediction of this background.

The last physics backgrounds considered are Drell-Yan and WW production. For the former, the cross section is based on the DØ measured value for $30 < m_{ee} < 60$ GeV/c^2, divided by the fraction of Monte Carlo events that fall into this range. For the latter, a theoretical calculation of the cross section is used. In both cases, the Monte Carlo event kinematics are used to estimate the rejection power of the selection cuts.

The instrumental background in the dielectron channel can arise from $W(\to e\nu)$ production in association with jets, with one jet misidentified as an electron, or the misidentification of two jets in multijet events. To determine this background, a parent sample containing two electromagnetic jets, one of which passes the electron identification criteria, is selected. Then the second jet is treated as an electron and all of the kinematic cuts are applied. The number of events in this sample are then multiplied by the probability that a jet will pass the electron identification requirements to get the expected background.

One event is observed in this channel with the expected background of 0.47 ± 0.09 events [38].

$\mu\mu$ Channel

The $\mu\mu$ channel shares the Z background with the ee channel, but the limited muon momentum resolution makes separation of the $t\bar{t}$ signal from this background more difficult. One cannot make the $\not\!\!E_T$ and the invariant mass cut in this case, as both the quantities are poorly measured. In order to deal with this background, a kinematic fit to the $Z \to \mu\mu$ hypothesis is applied [39], and event is required to have a χ^2 probability less than 1% for this fit.

This background is estimated from the $Z \to \mu\mu$ Monte Carlo. In order for the Monte

Carlo generation to be reasonably efficient for producing events with 2 jets in association with the Z bosons, cuts are applied on the Monte Carlo generation, either by requiring the Z p_T to be above a certain value or by requiring that there be two final state partons included in the hard process calculation. Rather than relying on a theoretical calculation for the Z cross section, one proceeds by applying analogous cuts to the $Z \to ee$ event sample, and scaling the well-measured inclusive Z production cross section by the fraction of events which pass the cut. An identical procedure is used to estimate the contribution of $Z \to \tau\tau \to \mu\mu$ events.

The remaining backgrounds, mainly $WW \to \mu\mu$ and Drell-Yan, are determined solely from the Monte Carlo acceptance, multiplied by the theoretical cross section.

The background due to a heavy quark jet being misidentified as an isolated muon is determined from the sample of events with a single muon and three or more jets. Each jet in the sample is then multiplied by its probability for appearing as an isolated muon to give this background.

In the $\mu\mu$ channel, a total of one event is observed with expected background of 0.73 ± 0.25 [40].

5.8.2 Lepton + Jets Channels

In addition to measuring the $t\bar{t}$ cross section in the e+jets channel with topological cuts, DØ also measures the cross section in the μ+jets channel with topological cuts and both e and μ plus jets channels with a μ tag.

The measurement of the $t\bar{t}$ production cross section in the μ+ jets channel using topological cuts is very similar to that of the e+jets channel and is not discussed here, but the details can be found in ref. [41].

μ-tag Selection

As an alternative to the tight topological cuts, one can also isolate the $t\bar{t}$ events by requiring that at least one of the jets is likely to arise from b quark decay. One factor which distinguishes b quarks from u and d quarks and gluons is their semileptonic decays (both direct or in a cascade $b \to c \to l$). Those that involve a muon are of particular interest, since the DØ detector can reliably identify muons even in midst of hadronic activity.

The crucial requirement for the μ (or b) tagging searches is that there exists a muon within $\Delta R < 0.5$ from the axis of one of the jets in the event. A minimum p_T cut of 4 GeV/c is applied to this muon.

Aside from a tagging muon, the kinematic requirements for the objects in the μ-tagging channels are quite similar to the topological channels. The exception is the jet requirement. Since the presence of the tagging muon considerably reduces the background, one can gain some efficiency by requiring three jets and still maintain a good signal to background ratio. The jet E_T cut is however raised to 20 GeV.

Additional requirements are applied to ensure that the $\not\!\!E_T$ is not introduced by mismeasurement of the muon momentum. The e+jets channel raises the $\not\!\!E_T$ cut to 35 GeV if $|\Delta\phi_{\not\!\!E_T,\mu}| < 25°$. Here $\Delta\phi_{\not\!\!E_T,\mu}$ is opening angle between $\not\!\!E_T$ and μ in the $r-\phi$ plane. For the μ+jets channel, a contour cut in the plane of $\Delta\phi_{\not\!\!E_T,\mu}$ vs. $\not\!\!E_T$ is made, where the muon considered is the highest momentum muon, be it isolated or tagging. The same Z-fit χ^2 cut used in the $\mu\mu$ channel is used to remove the Z boson events. Finally, to further increase the efficiency, less stringent $\mathcal{A} - H_T$ cuts are applied.

$$H_T > 110 \text{ GeV}$$

$$\mathcal{A} > 0.04$$

The sources of backgrounds in the μ-tagging channels are similar to those in the topological searches ($Z \to \mu\mu$ is an additional background in the tagged μ plus jets channel), but the methods for calculating the background are different. In μ tagging analysis, it is critical to understand the probability for a given jet to have a muon within its cone. This probability is measured by using a large sample collected from a multijet trigger, and is found to increase linearly with increasing jet E_T.

The calculation of the backgrounds due to multijet events with jets misidentified as electrons or isolated muons then proceeds similarly to that for the topological channels. The W+multijet backgrounds are estimated by considering the sample of events without a tagging muon which passes all of the kinematic cuts except $\mathcal{A}$ and H_T. The probability for each jet in this sample producing a false tag is then calculated, and the total probability is summed to give the expected number of false tags. This number is multiplied by the efficiency of the $\mathcal{A}$ and H_T cuts when applied to this sample to give the total number of expected events in the final sample.

The small background in the tagged μ+ jets channel from $Z \rightarrow \mu\mu$ events is estimated from Monte Carlo samples and relies on the calculated Z plus multijet production cross section.

5.8.3 The $e\nu$ Channel

Another channel used to measure the $t\bar{t}$ cross section is the $e\nu$ channel. This channel has acceptance in the regions of phase space rejected by the other channels. One example is a dilepton event where one W decays to an energetic electron and soft neutrino, and the other W decays to a soft lepton and an energetic neutrino. Then it is quite likely that the soft lepton will fall below the kinematic requirements of the dilepton selection and will have too few jets to be included in the single lepton sample.

The selection for this channel is based on this scenario and imposes tight $\not\!\!E_T$ (> 50 GeV) and $e\nu$ transverse mass ($> 115\text{GeV/c}^2$) cuts to eliminate events containing only a single leptonic W as well as misidentified multijet events. In addition, the second leading jet is required to have E_T greater than 30 GeV and the azimuthal angle between $\not\!\!E_T$ and second-leading E_T object is required to be greater than 0.5 radians.

After these cuts are imposed, one finds that in addition to the above source of events, this channel also accepts events in which one of the W decays to a τ, which in turn decays to an electron and the other W decays hadronically, as well as a small percentage of single lepton+jets events. In order to keep this channel orthogonal to the others, any events which pass the requirements of any of the dilepton or lepton plus jets channels are explicitly vetoed.

Four events are observed in this channel with an expected background of 1.2 ± 0.4 events [42].

5.9 Top Quark Production Cross Section from All Channels

Adding the contributions of all the eight channels discussed above, DØ observes a total of 40 with a background of 13.3 ± 2.2 events. The $t\bar{t}$ production cross section from all channels can be determined using the equation:

$$\sigma_{t\bar{t}} = \frac{\sum_{i=1}^{8}(N_i - B_i)}{\sum_{i=1}^{8}(\epsilon \times BR)_i \mathcal{L}_i}$$

where the sum is over all channels, N_i, B_i, $(\epsilon \times BR)_i$ and $\mathcal{L}_i$ are the number of events observed, the expected background, the $t\bar{t}$ efficiency times branching ratio, and luminosity respectively for a given channel. Table 5.14 summarizes these numbers for individual channels for the top quark mass of 170 GeV/c^2.

Decay Mode	$\epsilon \times BR(\%)$	$< N_{\rm top} >$	$N_{\rm Bkg}$	Observed
ee	0.17 ± 0.02	1.20 ± 0.18	0.47 ± 0.09	1
$e\mu$	0.35 ± 0.07	2.20 ± 0.48	0.21 ± 0.16	3
$\mu\mu$	0.11 ± 0.01	0.64 ± 0.09	0.73 ± 0.25	1
$e\nu$	0.26 ± 0.08	1.66 ± 0.48	1.16 ± 0.26	4
$e +$ jet (topo.)	1.31 ± 0.19	8.80 ± 1.38	4.17 ± 1.02	10
$e +$ jet ($\mu-$tag)	0.57 ± 0.08	3.59 ± 0.56	1.05 ± 0.39	10
$\mu +$ jet (topo.)	0.91 ± 0.27	5.51 ± 1.67	4.16 ± 1.02	5
$\mu +$ jet ($\mu-$tag)	0.37 ± 0.09	2.25 ± 0.54	1.39 ± 0.23	6

Table 5.14: Summary of each of the top decay channels. Here $< N_{top} >$ is the expected number of top events based on the theoretical cross section [9] for $m_t = 170$ GeV/c^2.

In assigning an uncertainty to the measurement of the cross section, one must take care to properly account for all the correlations between the uncertainties in each individual measurement [43]. While the channels are orthogonal by definition, they all rely on the same luminosity measurement, all share the uncertainty in the jet energy scale measurement, and many use the same Monte Carlo samples to estimates the backgrounds. The final results for $\sigma_{t\bar{t}}$ at DØ measured top quark mass of 172 GeV/c^2 is:

$$\sigma_{t\bar{t}} = 5.9 \pm 1.8 \text{ pb}$$

The measured cross section as function of the top quark mass is shown in Fig. 5.9. The measured cross section agrees well with the theoretical predictions.

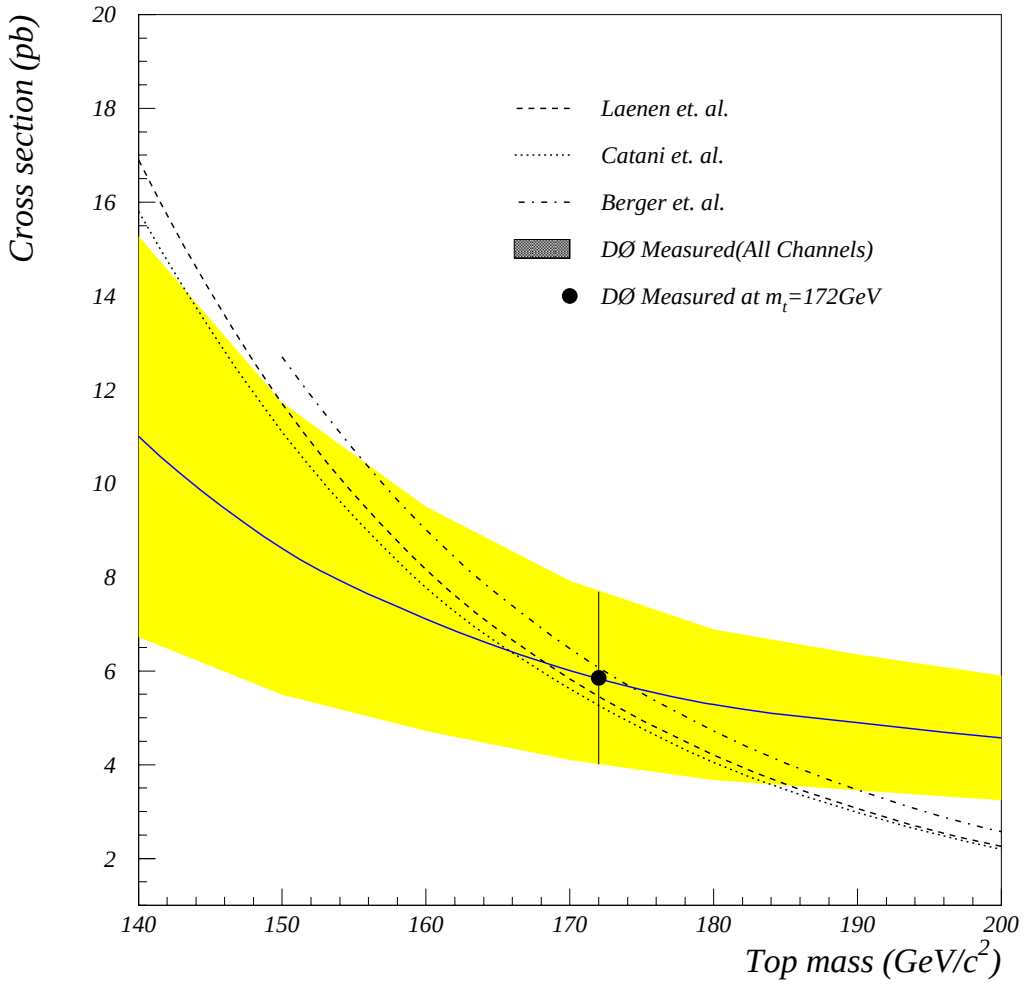

Figure 5.9: Measured cross section as a function of top quark mass. The solid line shows the central value of cross section measured using all the 8 channels. The lighter band shows its one standard-deviation error. Also shown are various theoretical calculations.

5.10 Conclusions

We performed a measurement of the production cross section of the top quark in the single electron decay channel using topological cuts. We observed a total of 10 events in this channel with an expected background of 4.2 ± 1.0 events. Assuming the excess to be due to

$t\bar{t}$ production, we measure the $t\bar{t}$ cross section in the $e+$jets channel at the DØ measured top quark mass as $3.8 \pm 2.1(\text{stat}) \pm 0.8(\text{sys})$ pb. Using all the single lepton and dilepton channels, we observe total of a 40 events with an expected background of 13.3 ± 2.2, corresponding to a $t\bar{t}$ production cross section of 5.9 ± 1.8 pb at the DØ measured top quark mass of 172 GeV/c^2. The measured cross section in the $e+$jets channel is consistent with the cross section determined using all the leptonic decay channels.

CHAPTER 6

SEARCH FOR SUPRESYMMETRY IN MODELS WITH A LIGHT GRAVITINO

In this analysis, we attempt a direct search for supersymmetry with a light gravitino in the framework of the minimal superesymmetric standard model (MSSM). We search for neutralino and chargino pair production in $p\overline{p}$ collisions at the Tevatron with R-parity conservation. In the analysis described in this chapter, the squarks and sleptons are assumed to be heavy such that the decays of charginos and neutralinos to the lightest neutralino proceed through intermediate W and Z/γ exchanges. Futhermore, the $\tilde{\chi}_1^0$ is assumed to be short-lived and to decay within the detector to $\gamma\tilde{G}$ with a branching ratio of 100%. Since the LSP is stable and non–interacting, pair production of the charginos and neutralinos will yield inclusive high E_T diphoton events with large missing transverse energy ($\not\!\!E_T$) with or without jets. The presence of high E_T photons and large $\not\!\!E_T$ provide a powerful tool for identifying these events over backgrounds.

In the framework of the MSSM, the gaugino-higgsino sector is parameterized by the four parameters: M_1, M_2, μ and $\tan\beta$, where M_1 and M_2 are the $U(1)$ and $SU(2)$ gaugino mass parameters at the electroweak scale, μ is the higgsino mass parameter and $\tan\beta$ is the ratio of the vacuum expectation values of the two higgs doublets. With the gaugino mass unification at the GUT scale which is assumed here, the M_1 and M_2 have the following relationship: $M_1 = \frac{5}{3}\tan^2\theta_{\rm W} M_2$. There are four neutralinos ($\tilde{\chi}_i^0,\ i = 1,2,3,4$) and two charginos ($\tilde{\chi}_j^{\pm},\ j = 1,2$) with their masses and couplings among each other and with the Standard Model particles fixed by the three parameters (M_2, μ and $\tan\beta$) in the MSSM.

6.1 Chargino and Neutralino Pair Productions

Chargino and neutralino pair production and the subsequent $\tilde{\chi}_i^0$ and $\tilde{\chi}_j^\pm$ decays are modelled using the SPYTHIA program [31], a supersymmetric extension of the PYTHIA 5.7 program [32]. As discussed above, the cross sections are functions of supersymmetry parameters M_2, μ and $\tan\beta$ [1]. To explore the parameter space, we chose to work in the (μ, M_2) plane while keeping $\tan\beta$ fixed, a strategy used by LEP extensively for studying supersymmetric models with $\tilde{\chi}_1^0$ as the LSP. We began our studies by investigating the cross sections in the (μ, M_2) plane to minimize time-consuming Monte Carlo simulations. Figure 6.1 (a) shows contours of constant cross section obtained from the SPYTHIA program for $\tan\beta = 2$. A value of $m_{\tilde{q}} = 800$ GeV/c^2 and the CTEQ3L parton distribution function [44] are used in the calculation. Futhermore, the renormalization scale is set to be equal to the average transverse mass of the processes. Although the production of all possible pairs of charginos and neutralinos are included in the calculation, most of the cross section is due to $\tilde{\chi}_1^\pm\tilde{\chi}_1^\pm$ and $\tilde{\chi}_1^\pm\tilde{\chi}_2^0$ production.

The constant mass contours of the $\tilde{\chi}_1^0$ and $\tilde{\chi}_1^\pm$ are shown in Fig. 6.1 (b) in the same plane. Evidently, the cross section is strongly correlated with the chargino and neutralino mass. It suggests that kinematics are largely responsible for the dependence of the cross section in the (μ, M_2) plane.

The dependence of the cross section on $\tan\beta(> 1)$ [2] is illustrated in Fig. 6.2 for four representative points in the (μ, M_2) parameter plane. The cross section is almost independent of $\tan\beta$ for $\tan\beta > 20$. When $\tan\beta < 20$, it increases slightly for $\mu < 0$ and decreases for $\mu > 0$. The variation in the cross section is strongly correlated with the variation in the chargino and neutralino masses. Unless it is otherwise specified, a $\tan\beta = 2$ is used in this analysis. Through t–channel diagrams, squarks also play a role in chargino and neutralino pair production. However, unless the squarks are lighter than $\sim$ 200 GeV/c^2, the effect is very small. In this analysis, we assume squark mass ($m_{\tilde{q}}$) degeneracy and set $m_{\tilde{q}}$ to be 800 GeV/c^2 which generally yields the lowest cross section for a reasonable variation of the

---

[1] The SPYTHIA program takes M_1 instead of M_2 as an input parameter. In order to compare our results directly with those from the LEP experiments, a small modification is made to the program with the consent of the author of the program to use M_2 as the input parameter .

[2] Since the top quark is much heavier than the bottom quark, one expects $\tan\beta > 1$. Futhermore, if the top quark Yukawa coupling remains perturbative up to the GUT scale, then $\tan\beta > 1.2$ [45]. The restriction $\tan\beta > 1$ is imposed in this analysis, but it is worth noting that the chargino and neutralino masses and couplings are symmetric under the transformation $\tan\beta \to \cot\beta$.

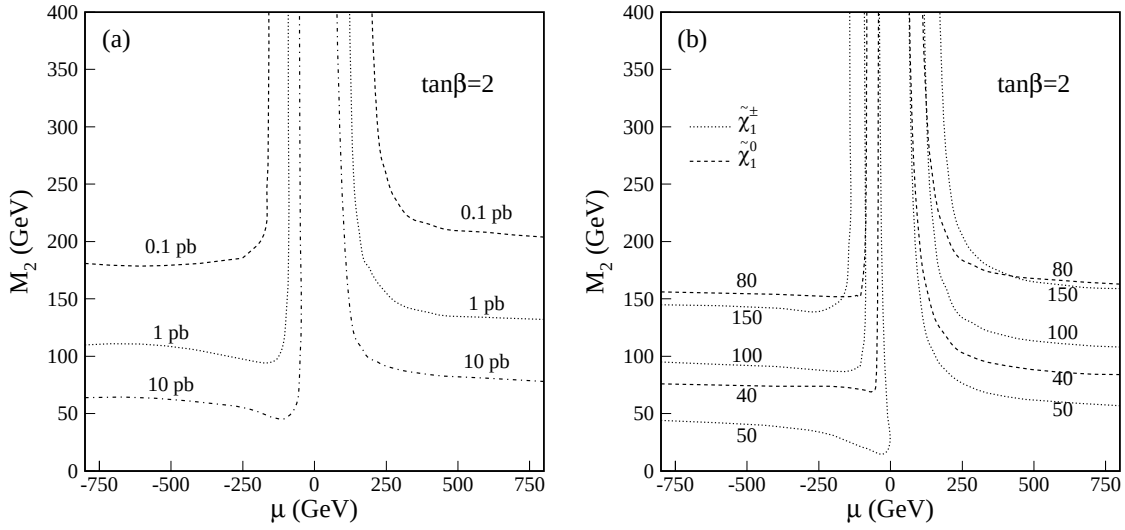

Figure 6.1: The constant contours in (μ, M_2) plane for $\tan\beta = 2$ of the cross section for the sum of $\tilde{\chi}_i^0\tilde{\chi}_j^0$, $\tilde{\chi}_i^0\tilde{\chi}_j^\pm$, and $\tilde{\chi}_i^\pm\tilde{\chi}_j^\pm$ production and (b) the mass of the lightest chargino (dotted line) and the lightest neutralino (dashed line) in units of GeV/c^2.

squark mass.

Event selection is best optimized by examining the expected distributions from supersymmetry. The generator–level E_T distributions of the leading (γ_1) and the second (γ_2) photon expected from an integrated luminosity of 100 pb^{-1} are shown in Fig. 6.3 (a) for two points in the (μ, M_2) plane. No event selection is applied. The photon E_T distributions vary widely from point to point in the parameter space and are strongly correlated with the chargino and neutralino masses. The photon pseduorapidity distributions for the same two points are shown in Fig. 6.3 (b). The two distributions are normalized to an equal area. Most photons are centrally produced, in particular when the charginos or neutralinos are heavy.

Topological distributions such as the diphoton opening angle and the smallest angle between $\not\!\!E_T$ and the two photons in the $r-\phi$ plane are shown in Fig. 6.4(a) and 6.4(b) respectively, where the $\not\!\!E_T$ is defined as the transverse energy of the two gravitinos. Events in these plots are required to have $E_T^{\gamma_1} > 20$ GeV, $E_T^{\gamma_2} > 12$ GeV and $\not\!\!E_T > 25$ GeV. Moreover, both photons must be within $|\eta| < 2.0$. Not surprisingly, these topological distributions depend strongly on the values of the supersymmetry parameters. For example, the $\Delta\phi$

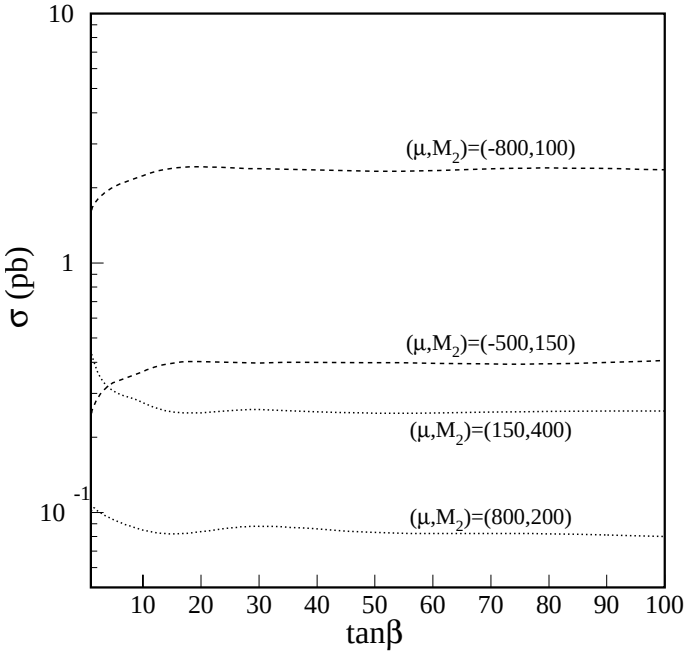

Figure 6.2: The cross sections as functions of $\tan\beta(> 1)$ for four representative points in the (μ, M_2) parameter plane.

distribution peaks strongly towards 180° when the chargino or neutralino is light,a fact expected from the Lorentz boost and is almost flat when the chargino or neutralino is heavy and their mass difference is small. For the same reason, the $\not\!\!E_T$tends to point in the direction of one of the two photons when the charginos/neutralinos are light. Therefore, to maximize the sensitivity to supersymmetry in a large parameter space, topology based selection is undesired, given the wide difference in topologies across the space.

6.2 Event Selection

The data used in this analysis were collected with the DØ detector during the 1992–1996 Tevatron run at a center–of–mass energy of 1.8 TeV. Runs with the Main Ring active are vetoed. The total luminosity used in this analysis is 106.3 ± 5.6 pb^{-1}. This analysis is restricted to events from the Level 2 filter ELE_JET for Run 1A and ELE_JET_HIGH for Run 1B/1C as summarized in table 5.2.

The signature of pair production of charginos and neutralinos is two high E_T photons

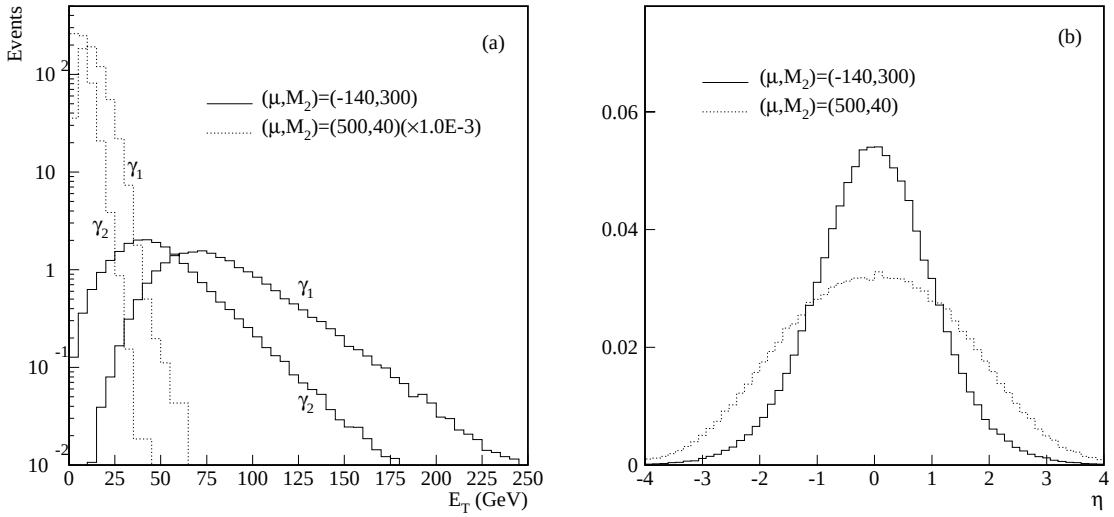

Figure 6.3: The generator–level E_T distributions of the leading (γ_1) and the second (γ_2) photons (a) and photon pseudorapidity distributions (b) for two points in the parameter space without any selection. The lightest chargino and neutralino masses are (149,131) GeV/c^2 for the point $(-140, 300)$ GeV and (30,15) GeV/c^2 for the point $(500, 40)$ GeV. Note that the E_T distribution for the point (500,40) GeV has been scaled down by a factor of 1000.

associated with large missing transverse energy. As discussed above, the event topology of pair production of charginos and neutralinos is substantially different across the parameter space. Topological cuts (such as the angle between two photons, $\not\!\!E_T$ direction etc.) will result in a loss of efficiency in some region of the space. With excellent photon identification and good $\not\!\!E_T$ resolution, we found that simple kinematic requirements are sufficient to reduce backgrounds to a negligible level. To be selected as $\gamma\gamma\not\!\!E_T$ candidates, events must have two photons satisfying quality requirements outlined in Sec. 4.2.2 and satisfy the following kinematic requirements:

(1) $E_T^{\gamma_1} > 20$ GeV with $|\eta^{\gamma_1}| < 1.2$ or $1.5 < |\eta^{\gamma_1}| < 2.0$,

(2) $E_T^{\gamma_2} > 12$ GeV with $|\eta^{\gamma_2}| < 1.2$ or $1.5 < |\eta^{\gamma_2}| < 2.0$,

(3) $\not\!\!E_T >$ 25 GeV.

In addition, there must be at least one reconstructed vertex in the event to ensure good

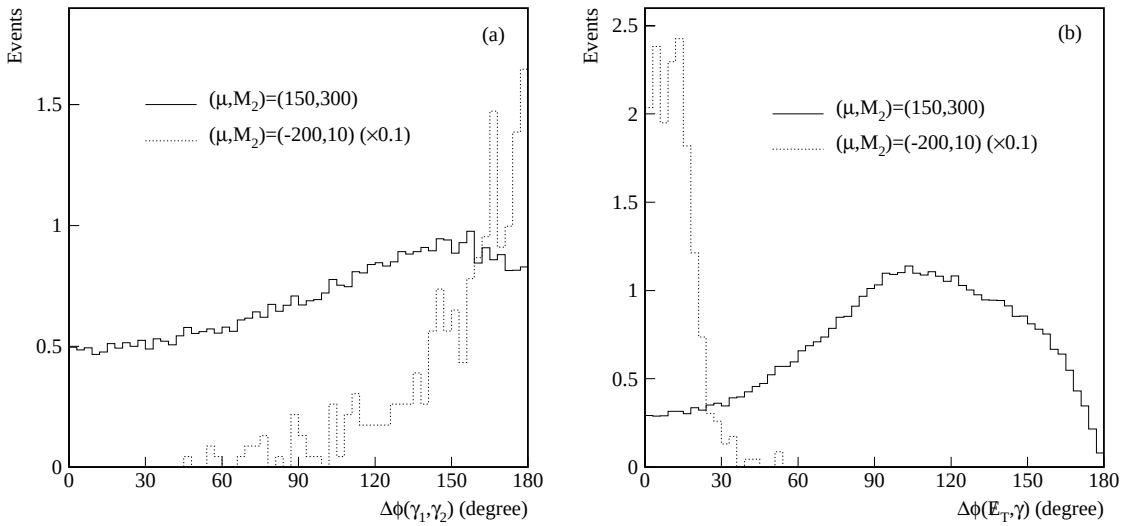

Figure 6.4: Topological distributions of (a) the diphoton opening angle and (b) the smallest angle between the photon and $\not\!\!E_T$in $r-\phi$ plane for events passing the generator–level selection. The corresponding $(m_{\tilde{\chi}_1^\pm}, m_{\tilde{\chi}_1^0})$ are (120,93) GeV/c^2 for the point (150,300) GeV and (31,6) GeV/c^2 for the point $(-200, 10)$ GeV. Note that the distributions for the point $(-200, 10)$ GeV have been scaled down by a factor of 10.

measurement of the missing transverse momenta. No requirement on jets is made in the event selection. The higher E_T requirement on the leading photon is necessitated by the trigger threshold. Nevertheless, the requirement is efficient for the parameter region with heavy charginos and neutralinos as shown, for example, in Fig. 6.3(a). The pseduorapidity requirement is dictated by the detector acceptance. After these cuts, two events (one from Run 1A and the other from Run 1B) survived [3].

Since only $\sim 15\%$ of the data were processed with good HITSINFOcuts, events which passed all the selection criteria above except the HITSINFO and the $\not\!\!E_T$ selections (229 events) are picked and reprocessed with the good HITSINFO package. These events are referred to as the $\gamma\gamma$ events in the following discussion. Twenty-eight events survived the HITSINFO

[3] The Run 1A event (Run # 62433, Event # 10839) has $\not\!\!E_T$ pointing to the Main Ring direction while the Run 1B event (Run # 91267, Event # 38689) has a photon in the Main Ring region and a $\not\!\!E_T$ back-to-back with that photon. We note that these events can be easily removed by applying additional requirements based on event topology. However, any topology based selection will undoubtly reduce the sensitivity to events from supersymmetry.

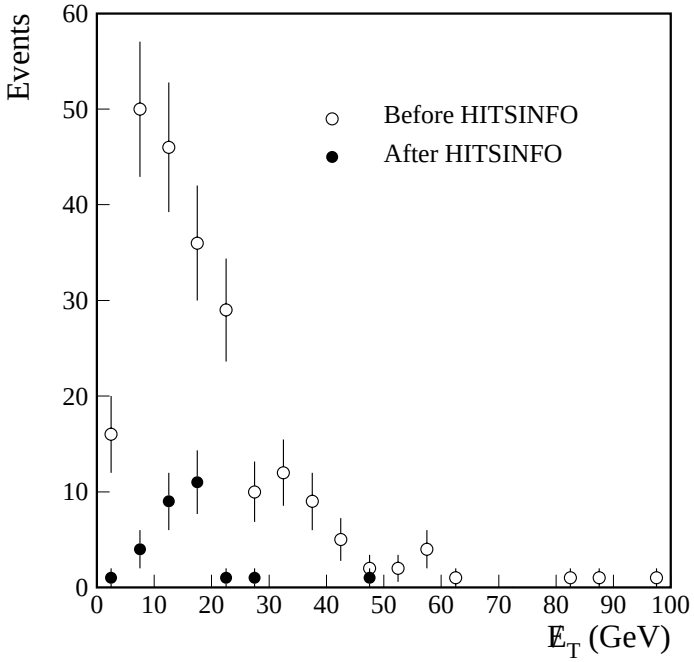

Figure 6.5: The $\not\!\!E_T$ distribution of diphoton events before (open circle) and after (solid circle) HITSINFO selection. After the HITSINFO selection, two events have $\not\!\!E_T$ greater than 25 GeV.

selection after reprocessing. Two of these events have $\not\!\!E_T$ above 25 GeV. The $\not\!\!E_T$ distributions before and after the HITSINFO selection are shown in Fig. 6.5.

6.2.1 Comments on $\not\!\!E_T$ Requirement

Large missing transverse energy is a key signature for the production of supersymmetric particles, while most of the background events from the standard model processes have zero or small $\not\!\!E_T$. Therefore, it is important to understand the cut on $\not\!\!E_T$. Table 6.1 [4] shows the numbers of candidate and background events together with the expected efficiencies of the supersymmetry model for the two representative points in parameter space. As expected, the number of background events and the efficiency for supersymmetry detection decrease as the $\not\!\!E_T$ threshold increases. A 25 GeV $\not\!\!E_T$ threshold is used in many previous analyses to

[4] $e\gamma\not\!\!E_T$ events with $\not\!\!E_T <$ 20 GeV are not picked for reprocessing with the good HITSINFO package. Therefore, no background estimation is made.

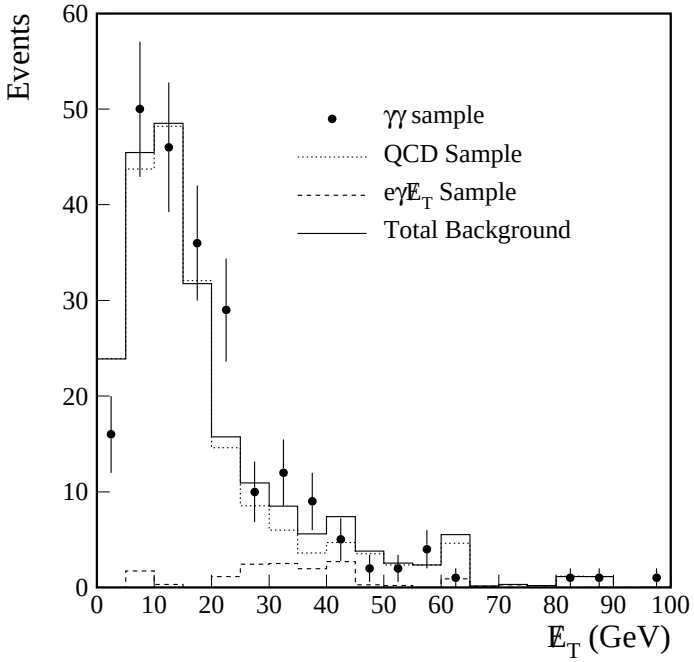

Figure 6.6: The $\not\!\!E_T$ distributions of the $\gamma\gamma$ and the background samples before the HITSINFO and $\not\!\!E_T$ selection. The number of events with $\not\!\!E_T <$ 20 GeV in the background samples is normalized to that of the $\gamma\gamma$ sample. The $e\gamma\not\!\!E_T$ contribution is obtained from those of the $ee, e\gamma$ events after subtracting QCD backgrounds by applying the electron rejection factor of the track (R_T). The apparent peak in the distribution is a result of falling spectrum with a trigger threshold.

select $W \to e\nu$ events and is adopted in this analysis. As shown in the table, it represents a reasonable compromise between good efficiency and good background rejection.

6.2.2 Electron Rejection

Due to the imperfect tracking detector and algorithm, an electromagnetic cluster produced by an electron can be misidentified as a photon. To aid in the background estimation discussed in the following Sec. 6.3, we introduce an electron rejection factor (R) which is defined as the ratio between the numbers of electrons and photons identified from a sample of electron–originated electromagnetic clusters. Unless otherwise specified, electrons are selected from PELC objects (EM clusters identified as an electron by DØRECO) and must pass the criteria

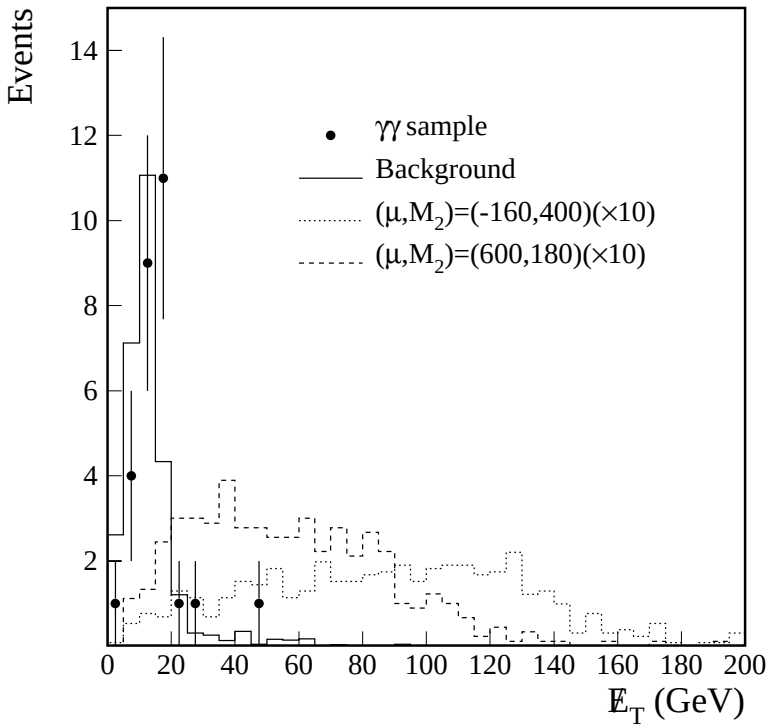

Figure 6.7: The $\not\!\!E_T$ distributions of the $\gamma\gamma$ and the background samples after the HITSINFO selection. Two $\gamma\gamma$ events have $\not\!\!E_T >$ 25 GeV after HITSINFO selection. The number of events with $\not\!\!E_T <$ 20 GeV in the background sample is normalized to that in the $\gamma\gamma$ sample. As discussed in Sec. 6.3, the $e\gamma\not\!\!E_T$ background is small after the HITSINFO selection. Also shown are the expected distributions from supersymmetry. Note that the distributions of the supersymmetry predictions have been scaled up by factor of ten.

for the electromagnetic clusters and have track–match significances (σ_{trk}) less than 5. The rejection is calculated using the method described in [46]. It consists of two components: rejection provided by the tracking and the rejection provided by the HITSINFO selection.

The rejection from the track (R_T) is calculated using the tracking finding efficiency (ϵ_t) and the efficiency (ϵ_m) for track–match significance reported in [47] using the formula:

$$R_T = \frac{\epsilon_t \epsilon_m}{1 - \epsilon_t}.$$

It is found to be 6.1 ± 0.3 for CC and 4.7 ± 0.2 for EC for the efficiencies ($\epsilon_t = 0.864 \pm 0.014$, $\epsilon_m = 0.934 \pm 0.009$ for CC and $\epsilon_t = 0.861 \pm 0.018$, $\epsilon_m = 0.766 \pm 0.028$ for EC)

$\not\!\!E_T$	Candidates	Backgrounds		Efficiencies	
Threshold	$N_{\gamma\gamma}$	QCD Sample	$e\gamma\not\!\!E_T$ Sample	$(-160, 400)$	$(600, 180)$
> 20 GeV	3	3.3 ± 1.4	$--$	0.256	0.184
> 25 GeV	2	2.1 ± 0.9	0.18 ± 0.09	0.247	0.172
> 30 GeV	1	1.4 ± 0.7	0.12 ± 0.07	0.241	0.160
> 35 GeV	1	1.0 ± 0.6	0.12 ± 0.07	0.238	0.149

Table 6.1: Numbers of $\gamma\gamma\not\!\!E_T$ and background events for four different thresholds on the $\not\!\!E_T$. The efficiencies for supersymmetry for the two representative points are also shown.

presented in [47]. The rejection of the HITSINFO selection in DØRECO version 12.20 or higher is estimated using the loose $W \rightarrow$'e'ν events. This sample is selected by requiring one PPHO (EM clusters identified as photon candidates by DØRECO) cluster passing the electromagnetic identification criteria and with $E_T > 20$ GeV. In addition, the events are required to have $\not\!\!E_T >$ 25 GeV. The HITSINFO selection is then applied to the PPHO in this sample. After subtracting QCD backgrounds from the sample both before and after HITSINFO selection, rejection factors (R_H) of 37.5 ± 5.9 for CC and 35.9 ± 8.4 for EC are obtained. Combining the rejections of the track and the HITSINFO selection, the tracking provided a total electron rejection factor ($R = R_H \times R_T$) of 229 ± 38 for CC and 169 ± 37 for EC. These numbers are in good agreement with 245 ± 60 for CC and 160 ± 50 for EC reported in [46] for Run 1A. The HITSINFO selection in DØRECO versions earlier than 12.20 is found to be inefficient in reducing the backgrounds for photons.

The validity of the HITSINFO rejection of electrons is checked using a sample of $Z \rightarrow ee$ events, which are selected by requiring two electromagnetic clusters each with $E_T > 20$ GeV and an invariant mass of the pair $86 < M_{ee} < 96$ GeV/c^2. The electromagnetic cluster can either be a PELC or a PPHO object. The HITSINFO rejection is then obtained by imposing the selection to the PPHO clusters. The rejection factor obtained for the CC is 40 ± 7, in good agreement with that estimated using the loose W events.

6.3 Background Estimations

The multijet, direct photon, $W+\gamma$, $W+$jets, $Z \to ee$ and $Z \to \tau\tau \to ee$ events from Standard Model processes with misidentified photons and/or mismeasured $\not\!\!E_T$ are the background sources for the $\gamma\gamma\not\!\!E_T$ events. The numbers of background events from these sources are estimated using data for the following two cases: diphoton events (genuine or misidentified) without genuine $\not\!\!E_T$ and events with genuine $\not\!\!E_T$.

Genuine or misidentified diphoton events without genuine $\not\!\!E_T$ will be misidentified as $\gamma\gamma\not\!\!E_T$ events if the $\not\!\!E_T$'s are significantly mismeasured. This background is estimated using a QCD sample selected by requiring:

(1) EM fraction > 0.9 for both clusters,

(2) isolation < 0.1 for both clusters,

(3) at least one cluster with H–matrix $\chi^2 > 200$,

(4) no track in road for PPHO clusters, and

(5) track–match significance greater than 10 for PELC objects

from the same dataset with the same trigger. The EM clusters can be either PELC or PPHO objects. In addition, the events are required to pass the kinematic requirements except the cut on $\not\!\!E_T$. As discussed above, the HITSINFO selection in DØRECO versions earlier than 12.20 are inefficient in rejecting backgrounds for photons. To avoid any inconsistency, no HITSINFO selection is applied here. These events are similar to those of the $\gamma\gamma$ sample and are expected to suffer from similar $\not\!\!E_T$ mismeasurement. For this reason, the $\not\!\!E_T$ distributions of the two samples are assumed to be the same for small $\not\!\!E_T$ in the analysis. They are compared in Fig. 6.6. Using a subset of the QCD sample processed with DØRECO version 12.20 or higher, the fraction of events passing the HITSINFO selection is computed as a function of $\not\!\!E_T$. Convoluting the fraction to the $\not\!\!E_T$ distribution of the QCD sample before the HITSINFO, a $\not\!\!E_T$ distribution of the QCD sample after the HITSINFO is obtained. By normalizing the number of events with $\not\!\!E_T < 20$ GeV in the QCD sample to that in the $\gamma\gamma$ sample (see Fig. 6.7), a background of 2.1 ± 0.9 events due to $\not\!\!E_T$ mismeasurement is obtained for $\not\!\!E_T > 25$ GeV.

The other backgrounds are due to events with genuine $\not\!\!E_T$ such as those from $W+$'γ' (where 'γ' can be a real or a fake photon), $Z \to \tau\tau \to ee$ and $t\bar{t} \to ee +$ jets production. These events (labelled as $e\gamma\not\!\!E_T$ events) would fake $\gamma\gamma\not\!\!E_T$ events if electrons are misidentified as photons. Their contribution is estimated from the data with electrons. A sample of e'γ' events (29 events in CC and 8 events in EC) passing the kinematic requirements including that on $\not\!\!E_T$ is selected. Standard electron and photon identification cuts are applied to select these events. By applying the electron rejection factors discussed in Sec. 6.2.2, an estimated 0.2 ± 0.1 events is expected.

Figure 6.6 compares the $\not\!\!E_T$ distributions of the $\gamma\gamma$, the QCD and the $e\gamma\not\!\!E_T$ samples before the HITSINFO selection. The number of events in the background samples is normalized to the corresponding number in the $\gamma\gamma$ sample. The $e\gamma\not\!\!E_T$ distribution is obtained by adding the distributions of ee events scaled down by a factor of R_T^2 and $e\gamma$ events scaled down by a factor of R_T after background subtraction. The ee and $e\gamma$ events are selected using the above kinematic requirement except the cut on $\not\!\!E_T$.

Adding the two background contributions together, a total 2.3 ± 0.9 background events is expected.

6.4 Signal Acceptances

Based on the theoretical cross sections of chargino and neutralino pair productions and acceptance studies at the generator–level, we have generated and simulated $\tilde{\chi}_i^0\tilde{\chi}_j^0$, $\tilde{\chi}_i^0\tilde{\chi}_j^\pm$ and $\tilde{\chi}_i^\pm\tilde{\chi}_j^\pm$ events for a large number of points in the (μ, M_2) parameter space. The Monte Carlo events are required to pass a GEANT [25] based DØ detector simulation program and a trigger simulator. They are subjected to the DØRECO version 12.22. For simplicity, the decay $\tilde{\chi}_1^0 \to \gamma\tilde{G}$ is assumed to occur close to the event vertex in the simulation and the gravitino mass is set to zero. Tables 6.2 and 6.3 lists the points in the (μ, M_2) parameter plane for $\tan\beta = 2$ with GEANT simulations together with the corresponding masses of the lightest chargino and neutralino and the theoretical cross sections obtained from the SPYTHIA program. The cross section is calculated using the CTEQ3L parton distribution function [44], but is found to be insensitive to the choice of the parton distribution function. The renormalization scale is set to the average transverse mass of the processes in the calculation.

The total efficiency for the supersymmetry model and the different components of

μ	M_2	$m_{\tilde{\chi}_1^0}$	$m_{\tilde{\chi}_1^\pm}$	σ_{th}	Efficiency (%)					σ_D	σ
GeV	GeV	(GeV/c^2)		(pb)	ϵ_K	ϵ_R	ϵ_{ID}	ϵ_D	$\epsilon(=\epsilon_K\epsilon_D)$	(pb)	(pb)
-10	10	6.2	51.4	985	0.062		40.8	–	0.025±0.008	–	286
-10	300	8.7	25.5	3458	0.072		38.5	–	0.029±0.008	–	223
-10	500	8.9	19.8	3810	0.022		36.6	–	0.008±0.004	–	477
-100	10	6.1	42.3	974	0.026		52.0	–	0.014±0.003	–	391
-200	10	6.1	31.4	4822	0.020		51.9	–	0.010±0.002	–	540
-145	300	134.6	153.6	0.19	67.7	86.6	42.5	35.7	24.2±1.4	0.13	0.20
-145	400	140.2	152.9	0.19	66.9	83.3	42.9	35.1	23.5±1.3	0.14	0.21
-160	200	103.6	163.1	0.18	65.9	71.0	42.7	29.8	19.6±1.3	0.16	0.25
-160	300	143.9	167.8	0.12	71.5	85.7	42.9	36.4	26.0±1.4	0.13	0.18
-160	400	154.4	167.5	0.12	66.2	87.4	42.9	37.0	24.5±1.4	0.13	0.20
-160	500	156.5	166.8	0.12	66.0	91.7	42.8	38.1	25.2±1.4	0.13	0.19
-180	200	103.9	177.4	0.13	62.3	76.5	42.6	32.3	20.1±1.3	0.15	0.24
-200	160	84.3	163.1	0.23	60.5	71.7	42.6	29.9	18.1±1.2	0.16	0.27
-300	160	83.7	167.8	0.19	56.1	68.0	42.1	28.4	15.9±1.2	0.17	0.30
-400	150	78.2	157.8	0.25	57.2	78.1	42.7	32.8	18.8±1.2	0.15	0.26
-400	160	83.2	167.5	0.20	58.1	68.5	42.6	28.8	16.8±1.2	0.17	0.29
-500	160	82.8	166.8	0.22	57.0	62.5	42.5	26.4	15.1±1.1	0.18	0.32
-600	140	72.5	146.4	0.36	53.5	76.8	42.6	32.1	17.2±1.2	0.15	0.28
-600	160	82.5	166.1	0.21	58.0	57.7	42.5	24.3	14.1±1.1	0.20	0.35
-800	150	77.1	155.1	0.31	58.2	77.9	42.3	32.6	19.0±1.2	0.15	0.25
-800	165	84.7	170.0	0.20	57.2	61.7	42.8	26.4	15.1±1.1	0.18	0.32
-1000	160	81.9	164.2	0.23	58.0	70.5	42.4	29.7	17.2±1.2	0.16	0.28
-1000	170	86.9	174.2	0.17	60.9	62.8	42.7	26.8	16.3±1.2	0.18	0.30

Table 6.2: Shown is a list of points in the (μ, M_2) plane for $\tan\beta = 2$ and $\mu < 0$ with GEANT simulation. The errors on the total efficiencies are statistical only. The systematic errors are estimated to be 6%. The last two columns list the 95% CL upper limits on the detectable (σ_D) and the total (σ) cross sections.

μ	M_2	$m_{\tilde{\chi}_1^0}$	$m_{\tilde{\chi}_1^\pm}$	σ_{th}	Efficiency (%)					σ_D	σ
GeV	GeV	(GeV/c^2)		(pb)	ϵ_K	ϵ_R	ϵ_{ID}	ϵ_D	$\epsilon(=\epsilon_K\epsilon_D)$	(pb)	(pb)
10	300	6.1	6.7	3523	0.140		51.0	–	0.078±0.008	–	65
145	500	117.4	130.4	0.39	66.1	62.8	42.5	26.0	17.2±1.2	0.18	0.28
170	500	139.0	154.2	0.18	68.3	80.4	42.8	33.9	23.2±1.4	0.14	0.21
180	300	109.7	144.4	0.24	62.3	62.1	42.4	26.2	16.3±1.2	0.18	0.30
180	350	123.2	152.1	0.18	66.0	76.9	42.8	32.7	21.6±1.3	0.15	0.22
200	300	118.1	160.2	0.15	66.8	75.5	42.6	31.9	21.3±1.3	0.15	0.23
300	190	85.6	152.4	0.28	61.3	62.6	41.9	25.7	15.8±1.2	0.19	0.31
300	205	92.9	164.0	0.19	61.6	77.0	42.4	32.4	20.0±1.3	0.15	0.24
400	190	89.4	166.4	0.19	61.7	77.2	42.8	32.5	20.1±1.3	0.15	0.24
500	185	88.6	168.5	0.19	62.2	76.4	42.6	31.9	19.9±1.3	0.15	0.24
600	175	84.6	162.6	0.24	61.8	63.1	42.3	26.4	16.3±1.2	0.18	0.30
600	180	87.1	167.5	0.20	59.5	68.9	42.4	28.8	17.2±1.2	0.17	0.28
800	170	83.2	161.6	0.25	58.7	79.8	42.5	33.4	19.6±1.3	0.14	0.25
1000	170	83.8	163.6	0.24	62.3	72.1	42.2	29.8	18.5±1.2	0.16	0.26

Table 6.3: Shown is a list of points in the (μ, M_2) plane for $\tan\beta = 2$ and $\mu > 0$ with GEANT simulation. The errors on the total efficiencies are statistical only. The systematic errors are estimated to be 6%. The last two columns list the 95% CL upper limits on the detectable (σ_D) and the total (σ) cross sections.

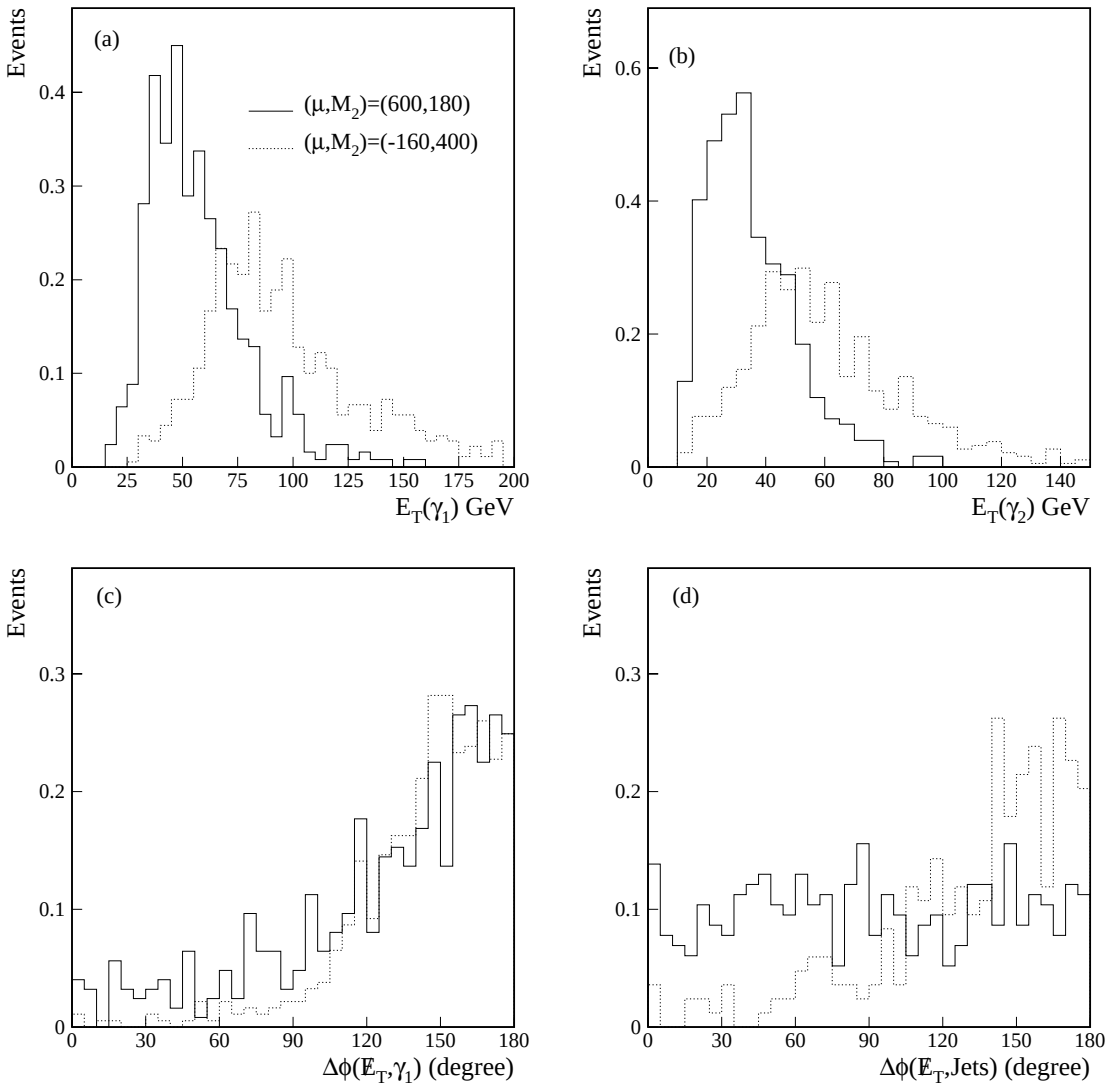

Figure 6.8: The Monte Carlo distributions of (a) the leading photon E_T, (b) the second photon E_T, (c) the opening angle between $\not\!\!E_T$ and the leading photon in $r-\phi$ plane, and (d) the smallest angle between $\not\!\!E_T$ and jets in $r-\phi$ plane for the two points in the supersymmetry parameter space. The corresponding ($m_{\tilde{\chi}_1^\pm}$,$m_{\tilde{\chi}_1^0}$) are (167,154) GeV/c^2 for the point ($-$160,400) GeV and (168,87) GeV/c^2 for the point (600,180) GeV. All distributions are normalized to the expected numbers of events in the data.

efficiency are listed in Tables 6.2 and 6.3. The followings are brief definitions of the efficiencies:

ϵ_K parton-level efficiency of kinematic requirements on photons and $\not\!\!E_T$;

ϵ_R reconstruction efficiency;

ϵ_T trigger efficiency (not listed in the table);

ϵ_{ID} identification efficiency for both photons
$\epsilon_{ID} = (\epsilon_C \times \epsilon_H \times \epsilon_X)^2$;

ϵ total efficiency for the supersymmetry model
$\epsilon = \epsilon_K \times \epsilon_T \times \epsilon_R \times \epsilon_{ID}$;

ϵ_D detecting efficiency for events passing kinematic requirements on photons and $\not\!\!E_T$
$\epsilon_D = \epsilon_T \times \epsilon_R \times \epsilon_{ID}$.

The trigger efficiency estimated using the trigger simulator for events which passed kinematic cuts ranging from 90% for light chargino or neutralino to almost 100% for heavy charginos or neutralinos. The photon identification efficiency includes the efficiencies of the calorimeter and tracking based selections as well as the efficiency loss due to the conversion of the photons into electrons. It also takes into account the over-estimation of the efficiency loss in the CCEM $\phi-$crack by the SHOWERLIB version of GEANT. By comparing the ϕ distribution (after mapping back onto a single CCEM module) of electromagnetic clusters between the data (W events) and the Monte Carlo (signal events), it is estimated that the inefficiency due to the $\phi-$crack is over-estimated by $(5 \pm 3)\%$ per object by the SHOWERLIB simulator. The total efficiency for the supersymmetry varies greatly from $\sim 0.01\%$ to $\sim 26\%$, depending largely on the masses of $\tilde{\chi}_1^{\pm}$ and $\tilde{\chi}_1^0$ and their mass difference. The estimated systematic error on the total efficiency is 6% which includes the efficiency uncertainties of the electromagnetic cluster identification (3%), the HITSINFO selection (3%), the reconstruction (2%), the photon conversion (2%), and the CCEM $\phi-$crack modeling (4%).

Sample distributions of the Monte Carlo events which passed the event selection for the two selected points in the (μ, M_2) plane are shown in Fig. 6.8. All distributions are normalized to the expected numbers of events in our sample after selection. The jets are reconstructed using a cone algorithm of radius $\sqrt{(\Delta\phi)^2 + (\Delta\eta)^2} = 0.5$ and are required to have $E_T > 15$ GeV and $|\eta| < 2.0$. As shown in Fig. 6.8 (c), the opening angle between $\not\!\!E_T$ and the leading photon is large, a topology expected from heavy $\tilde{\chi}_1^0$ decays. Also the distribution of the smallest opening angle between $\not\!\!E_T$ and jets in $r - \phi$ is flat when $m_{\tilde{\chi}_1^{\pm}} - m_{\tilde{\chi}_1^0}$ is large

and favors large angles when $m_{\tilde{\chi}_1^\pm} - m_{\tilde{\chi}_1^0}$ is small, as expected from the decay kinematics. In the case of small $m_{\tilde{\chi}_1^\pm} - m_{\tilde{\chi}_1^0}$, there is little jet activity in the events (see Fig. 6.9). In this case, most of the energy in an event is carried by photons and gravitinos, resulting in hard photon E_T spectra as demonstrated in Fig. 6.8 (a) and (b) and $\not\!\!E_T$ distribution shown in Fig. 6.7.

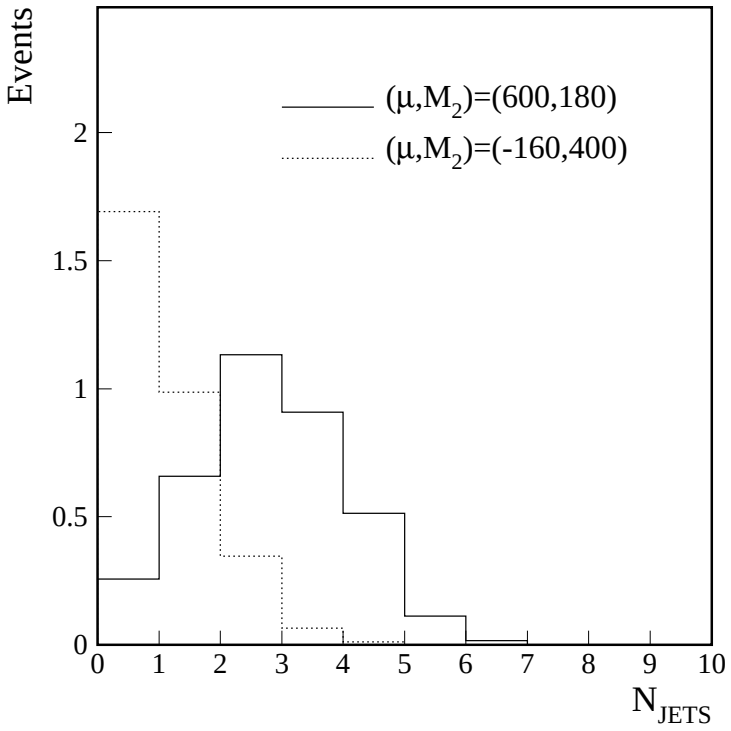

Figure 6.9: The distributions of the number of jets expected from pair productions of charginos and neutralinos for the two points in the (μ, M_2) plane.

6.5 Results and Discussion

6.5.1 Cross Section Limits

With two events observed and 2.3 ± 0.9 events expected from the backgrounds, we observe no excess of events above the expectation from misidentifications and mismeasurements. We

compute 95% C.L. upper limits of the total cross section (σ) for the sampling points in the (μ, M_2) plane using the estimated efficiencies (ϵ) with their errors discussed above. The cross sections computed using a Bayesian approach [48] with a flat prior distribution for the signal cross section are listed in the last column of the Tables 6.2 and 6.3. Depending on the values of the supersymmetry parameters, the limits vary widely from a few hundreds picobarns(pb) for light charginos/neutralinos to ~ 0.18 pb for heavy charginos/neutralinos.

We also compute 95% C.L. upper limits of the detectable cross section (σ_D) for diphoton events with $E_T^{\gamma 1} > 20$ GeV, $E_T^{\gamma 2} > 12$ GeV, $|\eta^\gamma| < 1.2$ or $1.5 < |\eta^\gamma| < 2.0$, and $\not\!\!E_T$>25 GeV using the detecting efficiency ϵ_D for the parameter points of interest. The resulting limits are also listed in Tables 6.2 and 6.3. The limits vary from ~ 0.13 pb to ~ 0.20 pb, depending on the value of the supersymmetry parameters. Conservatively, we set a 95% CL detectable cross section limit for inclusive pair production of charginos and neutralinos $\sigma_D < 0.20$ pb for diphoton events with $E_T^{\gamma 1} > 20$ GeV, $E_T^{\gamma 2} > 12$ GeV, $|\eta^\gamma| < 1.2$ or $1.5 < |\eta^\gamma| < 2.0$, and $\not\!\!E_T$> 25 GeV. Care must be taken in comparing this limit with that reported in Ref. [49] due to the different kinematic cuts applied. Parton level studies show that the kinematic cuts used in this analysis are about 30% more efficient than those used in Ref. [49]. Moreover, the Monte Carlo events used to calculate the efficiency in this analysis generally have more jet activity than those used in Ref. [49]. Please also note that this limit is somewhat arbitrary given that only a limited number of parameter points are sampled.

6.5.2 Bounds in the Supersymmetry Parameter Space

To derive limits in the (μ, M_2) plane, the values of μ and M_2 are varied around the sampled points until the theoretical cross section exceed the upper limits. The bounds in the (μ, M_2) plane are shown in Fig. 6.10, along with the points sampled with GEANT simulations. As shown in Tables 6.2 and 6.3, the efficiency for supersymmetry is reasonably constant around the sampled points when the charginos and neutralinos are heavy, despite the great variations across the parameter space. Here a constant efficiency for supersymmetry is assumed around a sampled point. Furthermore, the smaller of the two efficiencies is used when two points are close together in the parameter space. The parameter region below the two solid lines is excluded by the analysis for $\tan\beta = 2$. The bounds depend on the $\tan\beta$ value slightly. In general, the bounds are stronger in the $\mu < 0$ half–plane and are weaker in the other half–plane for a larger $\tan\beta$. The bounds for a smaller $\tan\beta$ are almost identical to those of

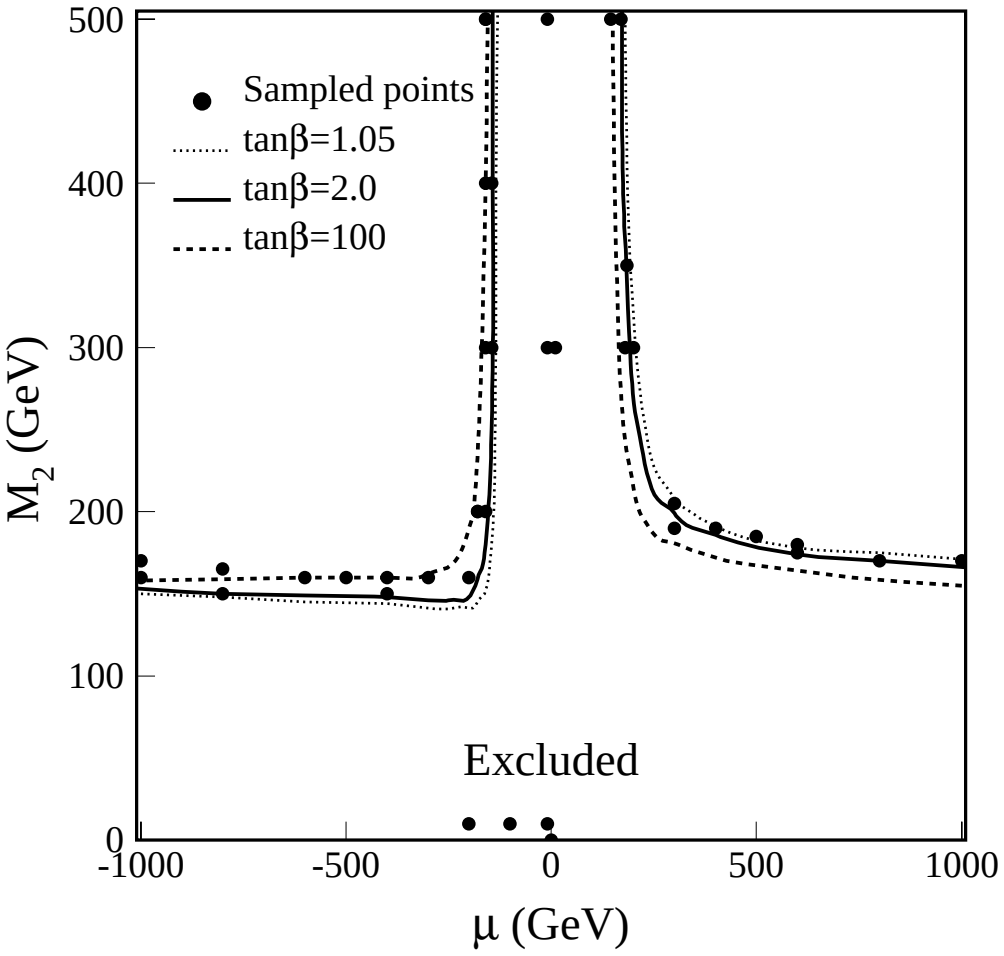

Figure 6.10: Sampled points in the (μ, M_2) plane with GEANT simulation. Also shown are bounds for $\tan\beta = 2$ (solid line), $\tan\beta = 1.05$ (dotted line) and $\tan\beta = 100$ (dashed line) derived from this analysis.

$\tan\beta = 2$. The limits for $\tan\beta = 1.05$ and $\tan\beta = 100$ are shown in Fig. 6.10 for comparison.

The bounds in the (μ, M_2) plane for $\tan\beta = 2$ derived from this analysis are compared in [16] with those estimated from the LEP data [5] in Fig. 6.11. The limits from this analysis are stronger than those of the LEP experiments and exclude the region of the parameter space speculated in [16] for the chargino interpretation of the CDF event. Also shown are the mass

---

[5] Most of the supersymmetry cross section at LEP is due to the $t-$channel exchanges of the slepton. Therefore, the LEP limits are strong functions of $m_{\tilde{e}}$. At the Tevatron, the charginos and neutralinos are produced primarily through the $s-$channel $W/Z/\gamma$ exchanges.

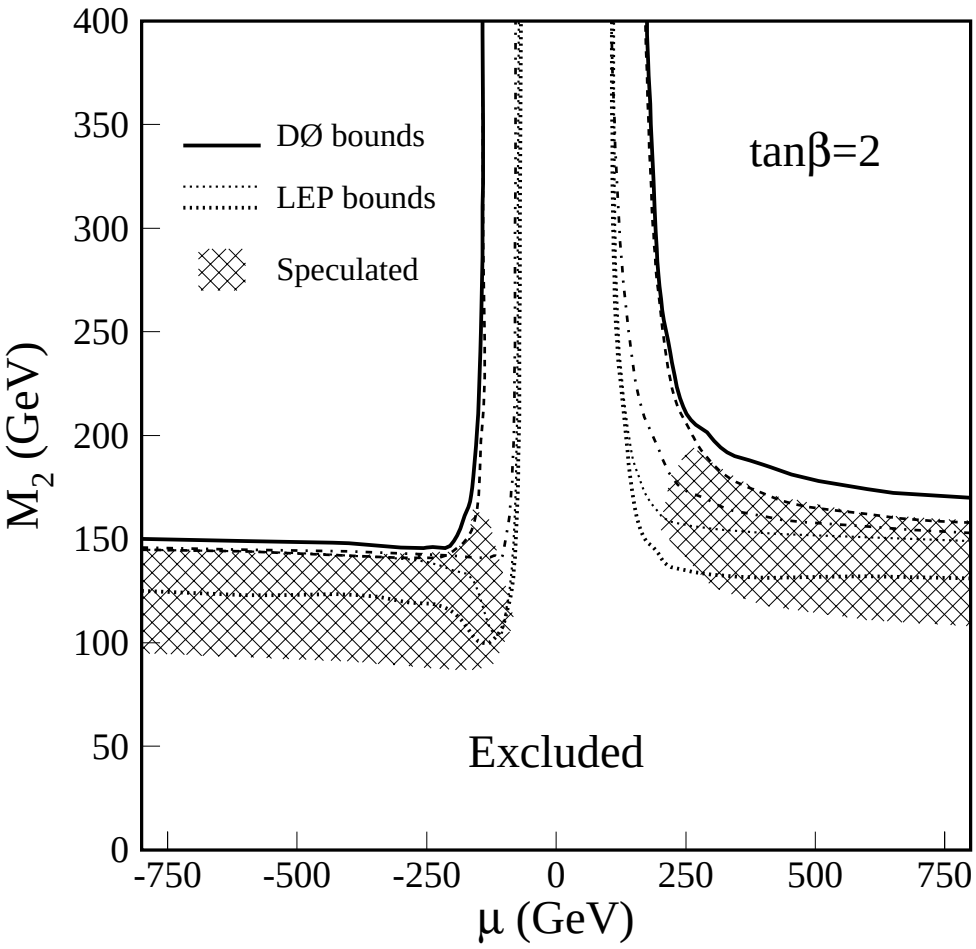

Figure 6.11: Bounds in the (μ, M_2) plane derived from this analysis for $\tan\beta = 2$. The region below the two solid lines is excluded at 95% CL. Also shown are the bounds estimated in Ref. [16] from the LEP data for $m_{\tilde{e}} = 150$ GeV/c^2 (thick dotted line) and for $m_{\tilde{e}} = 75$ GeV/c^2 (thin dotted line) and the contours of constant $m_{\tilde{\chi}_1^\pm} = 150$ GeV/c^2 (dashed line) and $m_{\tilde{\chi}_1^0} = 75$ GeV/c^2 (dot-dashed line). The hatched areas are speculated in [16] for the chargino interpretation of the CDF event in the model.

contours of $m_{\tilde{\chi}_1^\pm} = 150$ GeV/c^2 and $m_{\tilde{\chi}_1^0} = 75$ GeV/c^2. Low mass limits of 150 GeV/c^2 for the lightest chargino and 75 GeV/c^2 for the lightest neutralino are derived from the bounds. The 75 GeV/c^2 lower mass limit on the lightest neutralino also rules out a large part of the parameter space suggested for the scalar electron interpretation [15, 16] of the CDF event.

Since the changes in $m_{\tilde{\chi}_1^\pm}$ and $m_{\tilde{\chi}_1^0}$ are primarily responsible for the $\tan\beta$ dependence of the theoretical cross section, the mass limits derived for $\tan\beta = 2$ are also valid for other $\tan\beta$ values studied here ($1 < \tan\beta < 100$). For the same reason, the speculated region of the parameter space for the CDF event is excluded for $1 < \tan\beta < 100$.

6.5.3 Limits on $\tilde{\chi}_1^\pm\tilde{\chi}_1^\pm$ and $\tilde{\chi}_1^\pm\tilde{\chi}_2^0$ Pair Productions

The pair production of charginos and neutralinos is dominated by the production of $\tilde{\chi}_1^\pm\tilde{\chi}_1^\pm$ and $\tilde{\chi}_1^\pm\tilde{\chi}_2^0$ pairs. Therefore, the null result of the search also constrains the production cross sections of these processes, as is often done for the gravity-mediated models. We note that for a large part of the parameter space ($|\mu| \gg M_2$), the following approximate mass relationship

$$m_{\tilde{\chi}_1^\pm} \approx m_{\tilde{\chi}_2^0} \approx 2 \times m_{\tilde{\chi}_1^0}$$

holds. We therefore express the cross section limits as functions of $m_{\tilde{\chi}_1^\pm}$. These limits are compared with the theoretical cross sections in Fig. 6.12. The efficiencies and the theoretical cross sections are obtained by varying M_2 while fixing $\tan\beta$ to 2 and μ to -500 GeV. For a given $m_{\tilde{\chi}_1^\pm}$, the efficiency is insensitive to the choice of the parameter values while the theoretical cross section varies within about 10% with the choice of the parameters. The limits are below the theoretical cross section for a large $\tilde{\chi}_1^\pm$ mass range.

6.6 Conclusions

We have searched for inclusive high E_T diphoton events with large missing transverse energy using the data collected with the DØ detector during the 1992–1996 Tevatron run at $\sqrt{s}$=1.8 TeV. Such events are predicted in the supersymmetric model with low energy gauge-mediated supersymmetry breaking. No excess of events is found. The null result is interpreted in the minimal supersymmetric standard model with a light gravitino. A large region of the supersymmetry parameter space is excluded. The limits rule out the chargino interpretation of the CDF event and exclude a large part of the parameter space suggested for the scalar electron interpretation in the model.

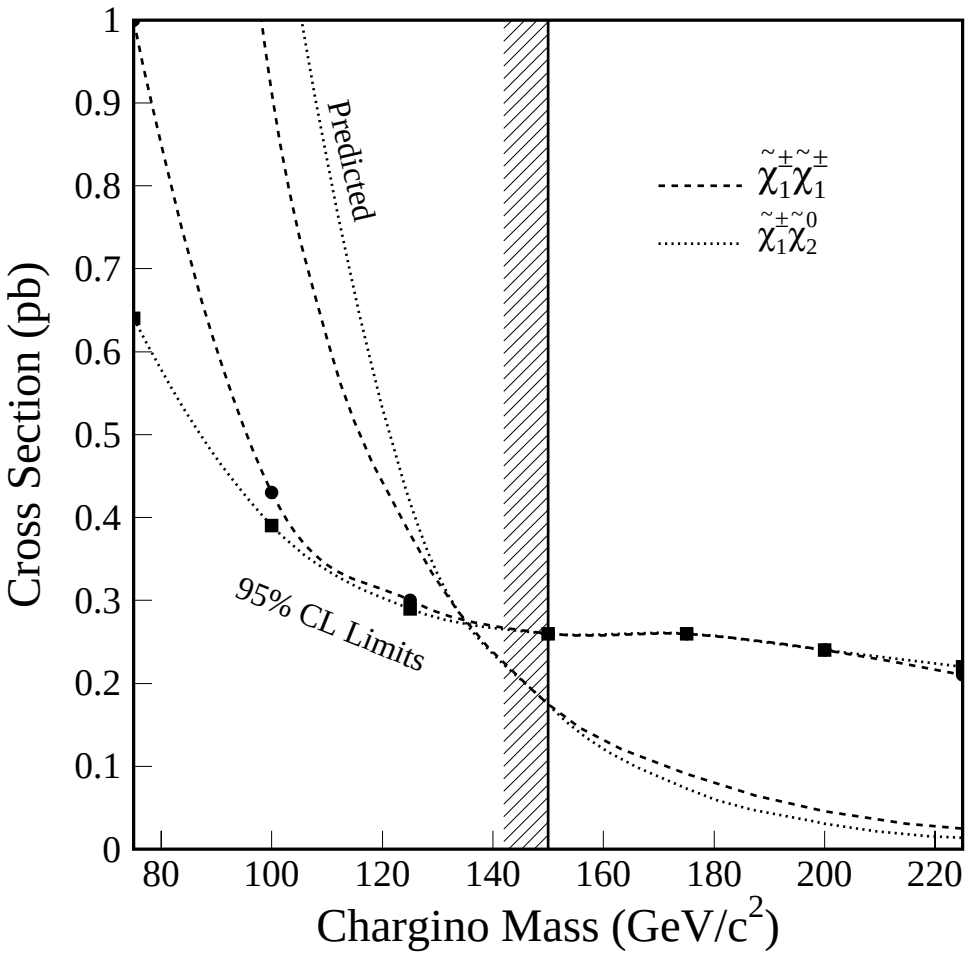

Figure 6.12: The 95% CL cross section limits and the theoretical cross sections for the $\tilde{\chi}_1^{\pm}\tilde{\chi}_1^{\pm}$ and $\tilde{\chi}_1^{\pm}\tilde{\chi}_2^{0}$ pair productions as a function of $m_{\tilde{\chi}_1^{\pm}}$. Also shown is the line representing the mass limit on the lightest chargino derived from this analysis.

BIBLIOGRAPHY

BIBLIOGRAPHY

[1] S.L.Glashow, J.Iliopoulos, and L.Maiani, Phys.Rev.**D2**, 1285 (1970).

[2] S.W. Herb *et al.*, Phys. Rev. Lett. **39**, 252 (1977).

[3] M.L. Perl *et al.*, Phys. Rev. Lett. **35**, 1489 (1975).

[4] G.L. Kane *Modern Elementary Particle Physics*, Addison-Wesley, 1993.

[5] DØ Collaboration, S.Abachi *et al.,* Physics.Rev.Lett. **72**, 2138 (1994).

[6] CDF Collabortion, F. Abe *et al.,* Phys. Rev. Lett. **73**, 225 (1994); Phys. Rev. **D50**, 2966 (1994).

[7] DØ Collaboration, S.Abachi *et al.,* Physics.Rev.Lett. **74**, 2632 (1995).

[8] CDF Collaboration, F. Abe *et al.,* Physics.Rev.Lett. **74**, 2626 (1995).

[9] E.Laenen,J.smith,W.van Neervan, Phys.Lett.**321B**, 254 (1994).

[10] E.Berger and H.Contopanagos, Phys.Lett. **361B**, 115 (1995).

[11] S.Catani, M.L.Mangano, P.Nason, and L.Trentadue, CERN-TH-96-21.

[12] E. Eichten, in *High Energy Physics 1985,* World Scientific, 709 (1986).

[13] X. Tata, in *The Standard Model and Beyond,* World Scientific, 304 (1991).

[14] D. Stump, M. Wiest, and C.-P. Yuan, Phys. Rev. **D54** (1996) 1936;
S. Dimopoulos, S. Thomas and J. Wells, Phys. Rev. **D54** (1996) 3283;
K. Babu, C. Kolda, and F. Wilczek, Phys. Rev. Lett. **77** (1996) 3070;
J. Lopez, D. Nanopoulos, and A. Zichichi, Phys. Rev. Lett. **77** (1996) 5168 and hep-ph/9610235;
H. Baer *et al.*, hep-ph/9610358;
J. Bagger *et al.*, hep-ph/9611229;
L. Randall, hep-ph/9612426.

[15] S. Dimopoulos *et al.*, Phys. Rev. Lett. **76** (1996) 3494;
S. Ambrosanio *et al.*, Phys. Rev. Lett. **76** (1996) 3498, Phys. Rev. **D54** (1996) 5395.

[16] J. Ellis, J. Lopez, and D. Nanopoulos, hep-ph/9610470.

[17] P. Fayet, Phys. Lett. **B70** (1977) 461; **B86** (1979) 272; **B175** (1986) 471;
D. Dicus, S. Nandi, and J. Woodside, Phys. Rev. **D41** (1990) 2347 and Phys. Rev. **D43** (1991) 2951.

[18] S. Park, "*Search for New Phenomena in CDF*", 10th Topical Workshop on Proton-Antiproton Collider Physics, edited by R. Raja and J. Yoh, AIP Press, 1995.

[19] DØ Collaboration, S. Abachi *et al.,* Nucl. Instrum. Methods **A338**, 185 (1994).

[20] D. Cutts*et al.,* IEEE Trans. Nucl. Sci. **NS-36**, 738 (1989)

[21] J. Yu, "*Determination of α_s and a Test of Perturbative QCD Using W+jets Processes in the DØ detector*", Ph.D. thesis, SUNY at Stony Brook, 1993(unpublished).

[22] U. Heintz *et al.,* "*A Likelihood Test for Electron ID*", DØ note 2386, (1994) unpublished.

[23] M. Kelly, "*Test of the Standard Model of Electroweak Interactions by Measuring the Anomalous $WW\gamma$ couplings at $\sqrt{s}$=1.8 TeV*", Ph.D. Thesis, Univ. of Notre Dame (1996) (unpublished);
DØ Collaboration, S. Abachi *et al.*, "*Limits on Anomalous $WW\gamma$ Couplings from $p\bar{p} \rightarrow W\gamma + X$ Events at $\sqrt{s}$=1.8 TeV*", hep-ex/9612002 and Fermilab-Pub-96/434-E.

[24] J. Womersley, "*Proceedings of the XXVI International Conference on High Energy Physics*", Dallas, Texas (1992).

[25] R. Brun and F. Carminati, CERN Program Library Long Writeup W5013, 1993 (Unpublished).

[26] R. Kehoe, "*Resolution Bias in Jet Response Measurement*" DØ Note 2052 (1994), unpublished.

[27] M. Paterno, "*A Study of the DØ Calorimeter E_T Resolution Using Low E_T Jet Triggers*", DØ Note 1782 (1993), unpublished.

[28] F.Paige and S. Protopopescu, "*ISAJET 6.49: A Monte Carlo Event Generator for pp and $p\bar{p}$ Interactions*", Fermilab Computing Division PM0059, (1992) (unpublished).

[29] R. Field and R. Feynman, Nucl. Phys. **B136**, 1 (1978).

[30] F. A. Berends, H. Kuijf, B. Tausk, and W. T. Giele, Nucl. Phys. **B357**, 32 (1991).

[31] S. Mrenna, "*SPYTHIA, A Supersymmetric Extension of PYTHIA 5.7*", hep-ph/9609360.

[32] H.U. Bengtsson and T. Sjöstrand, Comp. Phys. Comm. **46** (1987) 43;
T. Sjöstrand, Comp. Phys. Comm. **82** (1994) 74.

[33] W.G.D. Dharmaratana *et al.,* "*DØ Shower Library- Version 2.0*" DØ Note 1730 (1993), unpublished.

[34] S. Chopra and M. Narain, "*Determination of QCD backgrounds in e+jets events*", DØ Note 2105;

[35] C. Stewart, C. Cretsinger, E. Won, "*Search for the Top Quark in the All-jets Channel at DØ*", D0NOTE 2588A; N. Amos *et al.* "*The Randon Grid Search : A simple way to find optimal cuts*", D0note 2791, unpublished. The RGSEARCH package used was written by Chip Stewart and Harrison Prosper.

[36] T. Trippe "*DØ Results on Top quark Mass*" Hadron Collider Physics, Stony Brook (1997);
B. Abbott *et al.*, "*Direct Measurement of the Top Quark Mass at DØ*" Phys. Rev. D. (in preparation).

[37] J. Cochran "*eμ truths in run I*" DØNote in preparation.

[38] R. Kehoe, "*Search for the Top Quark in the Dielectron Final states at* $\sqrt{s}$ = 1.8 TeV *and Measurement of Response of DØ U/LAr Calorimeter to Jets*", Ph.D. thesis, Univ. of Notre Dame(1997) unpublished.

[39] R.E. Hall *et al.*, "*Studies of Kinematic Fitting of Dimuon Events*" DØ Note 2591 unpublished.

[40] J. Bantly *et al.*, "*Top Counting in the Dimuon Channel: DØAnalysis of Run 1*", DØNote 3088 (1997), unpublished.

[41] J.M. Butler *et al.*, "*Measurement of the Top quark production cross Section using lepton+jets events*" DØ Note 2978, unpublished.

[42] K. Genser, "*Search for the Top Quark in eν channel*", DØNote 3067 (1997), unpublished.

[43] H. Greenlee *et al.*, "*Theory of Correlated Errors in Top Quark Background and Cross Section Calculation*", DØ Note 2808, unpublished.

[44] H. L. Lai *et al.*, Phys. Rev. **D51** (1995) 4763.

[45] M. Carena *et al.*, Nucl. Phys. **B369** (1992) 33;
J. Bagger *et al.*, Phys. Rev. Lett. **55** (1985) 920.

[46] G. Landsberg, "*Search for Anomalous Couplings in the* $Z(\nu\nu)\gamma$ *Channel with Run Ia Data*", DØnote 3047, unpublished;
G. Landsberg, "HITSINFO *package*", to be released as a DØnote, unpublished.

[47] S. Chopra, U. Heintz and M. Narain, "*Comparison of Electron ID Efficiencies in Run 1A and 1B*", DØnote 2351, unpublished.

[48] Particle Data Group, R. M. Barnett *et al.*, Phys. Rev. **D54**, (1996) 165;
J. Hobbs, the limit program http://d0sgi0.fnal.gov/~hobbs/limit_calc.html;
I. Bertram *et al.*, "*A Recipe for the Construction of Confidence Limits*", DØnote 2775A, unpublished.

[49] DØ Collaboration, S. Abachi *et al.*, "*Search for Diphoton Events with Large Missing Transverse Energy in* $p\overline{p}$ *Collisions at* $\sqrt{s}$*=1.8 TeV*", hep-ex/9612011 and Fermilab-Pub-96/446-E.